UNIVERSITY OF CALIFORNIA
RIVERSIDE

The Effects of Dynamic Stress on Fault Interaction and Earthquake Triggering in the San Gorgonio Pass and San Jacinto, CA Regions

A Dissertation submitted in partial satisfaction
of the requirements for the degree of

Doctor of Philosophy

in

Geological Sciences

by

Jennifer Mary Tarnowski

March 2017

Dissertation Committee:
Dr. David Oglesby, Chairperson
Dr. Michele Cooke
Dr. Abhijit Ghosh

The Dissertation of Jennifer Mary Tarnowski is approved:

_____

_____

_____

Committee Chairperson

University of California, Riverside

Acknowledgements

There are several people without whom this dissertation would have never seen the light of day. First off, on the science side of things, I have to thank Michael Barall and Kenny Ryan for collaborating to create a version of FaultMod that can handle Cubit and Trelis output. Without this advancement, two chapters of this dissertation would have been impossible. None of the other mesh-generation options that were available when I started this degree were capable of handling the types of problems I intended to tackle. You two made all the future in-roads with modeling complicated geometries possible in the Oglesby lab. Special thanks also go to Abhi Ghosh. Despite several setbacks, I kept trying to make a non-modeling seismology project work out. Thankfully, after I just kept showing up to his lab meetings to learn about observational seismology, he eventually accepted me as an extra member of his group. Without him, the final chapter of this dissertation would not exist. Thanks also go to the members of the Ghosh lab for providing the occasional Matlab and Coral scripts and, more importantly, providing great discussions about our work and classes. Thank you Matt, Bo, and Allie. Last, but far from least on the science side of things, I have to thank Christodoulos Kyriakopoulos. Christos taught me how to work around bugs in Trelis, check my meshes for errors, and provided so many other tips and tricks for mesh generation. He played an invaluable role in the creation of the models for the second chapter of this dissertation.

On a more personal note, I want to thank David Oglesby, my advisor, for being patient with me. When I decided an academic career was not a good fit, he gave me the freedom to pursue different career options through various internships, professional

societies, and short courses during my time at UCR—even supporting my decision to be co-enrolled at CSU Long Beach for two quarters to learn industry-specific skills. For that, I am forever grateful. David, your support was the reason I stayed and honored my commitment to this degree even after difficulty after difficulty after difficulty arose. I also want to thank Michele Cooke for graciously stepping in as my third committee member and providing collaboration and support, despite being 3000 miles away. On another personal note, my thanks go out to Matt Mendoza, who would go for Starbucks and late night In-N-Out runs with me and even walk me back to my car when I stayed in the lab until well after Lot 13 emptied out.

Finally, on the most personal note of all, I thank my fiancé, Luke Gridley. Thank you for meeting me during the ups and downs of this degree and still deciding you wanted to marry me. Thank you for being by my side through the horrible summer in D.C., the shoulder injury, the debilitating fear following the car accident in Houston, the ankle injury, the oil crash that resulted in the loss of my job offer, and finally the burglary at UCR that undid so much of my work (and everything in between). You stood by my side, despite needing to work in Mississippi and Alabama and now that you are here in California with me, I look forward to the next chapter of our shared future together.

ABSTRACT OF THE DISSERTATION

The Effects of Dynamic Stress on Fault Interaction and Earthquake Triggering in the San Gorgonio Pass and San Jacinto, CA Regions

by

Jennifer Mary Tarnowski

Doctor of Philosophy, Geological Sciences
University of California, Riverside, March 2017
Dr. David Oglesby, Chairperson

We investigate how dynamic stresses can affect the occurrence of earthquakes in two regions in southern California. First we examine the San Gorgonio Pass (SGP) with 3D dynamic finite element models to investigate potential rupture paths of earthquakes propagating along faults in the western SGP. The SGP is extremely structurally complex because the San Andreas Fault splinters into many different fault strands in this area, and there are additional regional fault zones present. It has long been suspected that this structural knot, which consists of the intersection of various non-planar strike-slip and thrust fault segments, may inhibit earthquake rupture propagation between the San Bernardino strand of the San Andreas Fault System and the San Gorgonio Pass Fault Zone. With simplified numerical models of rupture propagation and slip, we find that nucleation on the San Bernardino strand does not produce through-going rupture to the San Gorgonio Pass Fault Zone, but nucleation on the San Gorgonio Pass Fault Zone may produce through-going rupture to the San Bernardino strand in some scenarios. Using

more realistically complex fault geometries in our models, we find the stress and subsequent rupture propagation patterns are highly influenced by the fault geometry and the initial stress field assumptions. Unlike in the models with simplified fault geometries, the results are not robust with respect to the input parameters. The complex models also have significantly different rupture propagation paths. Earthquakes that originate along the San Gorgonio Pass Fault Zone do not result in multi-fault rupture and there are generally fewer scenarios that include multi-fault rupture compared to the simple models. The combination of complex fault geometry and extremely heterogeneous initial stresses lead to results that imply the SGP could be a barrier for rupture propagation. In a separate study, we evaluate catalog earthquake data from the San Jacinto Fault Zone (SJFZ) for evidence of remote triggering of local earthquakes. We find that, while rare, local events are triggered along the SJFZ by large magnitude remote events and that a combination of statistical tests, peak magnitude analysis, and visual scans of seismograms are required to validate these examples of triggering.

Table of Contents

List of Figures

Introduction

Chapter 1

Chapter 2

Chapter 3

List of Tables

Chapter 1

Chapter 2

Chapter 3

Introduction

Stress in the Earth plays a critical role in the generation, rupture and slip behavior, and cessation of earthquakes. In general, stress conditions can control whether it is possible for an earthquake to occur at any given time. Faults can respond to long-term changes in stress, referred to as static stress, as well as short-term dynamic stress changes. While the distinctions regarding the type of stress change are somewhat arbitrary (i.e. there is no absolute measure of what length of time constitutes a long-term stress change), these distinctions are an essential part of earthquake triggering literature. Differentiations between static, quasi-static, and dynamic stress play a role in determining earthquake-triggering mechanisms. A static stress change is a more-or-less permanent change in the long-term stress following a physical process such as an earthquake. An earthquake can change the stress state in the surrounding rock, bringing some areas either closer to or further from failure (e.g. *King et al*., 1994, *Harris et al*., 1995). Quasi-static stresses are similar, but assume stress changes less gradual than static stress and more gradual than dynamic stress (*Stuart*, 1979). This intermediary stress change is associated with visco-elastic relaxation of the lower crust and transient deformation capable of triggering earthquakes (*Pollitz and Sacks*, 2002). Assuming static or quasi-static stresses, the stress change following an earthquake is often described by the change in the Coulomb Failure Function (CFF), evaluated as

$$\Delta CFF = \Delta\tau - \mu_s \Delta\sigma_n \tag{0.1}$$

where $\Delta\tau$ is the change in shear stress, μ_s is the static coefficient of friction, and $\Delta\sigma_n$ is the change in the normal stress, negative in compression in this sign convention, (e.g.

Oppenheimer et al., 1988; *Cocco and Rice*, 2002). A positive value for ΔCFF indicates the stress state in a particular location has increased towards Coulomb failure and potential fault failure and earthquake triggering.

Dynamic stress changes in particular are the focus of this dissertation. In contrast to static and quasi-static stresses, dynamic stresses are temporary stress changes that arise during the passage of seismic/acoustic waves. These types of stresses are transient, affecting the surrounding rock as seismic waves pass through, and typically dying out once waves have passed. However, depending on the initial stress state of the surrounding rock and any faults present in the rock volume, dynamic stresses can temporarily raise the stress state to what is referred to as a critically stressed state, in which failure can occur. One of the potential physical models explaining dynamic triggering at large distances is fluid activation. In this mechanism, dynamic stress changes affect permeability and fluid transport, subsequently causing a re-distribution of pore pressure that makes a rock volume more susceptible to failure (*Brodsky et al.* 2003; *Wang and Manga*, 2009; *Elkhoury et al*., 2011). The importance of dynamic stresses and their triggering capabilities arose in industry and intelligence applications, such as the former USSR's use of nuclear explosives to stimulate hydrocarbon reservoirs (e.g. *Nordyke*, 1975) and in studies designed to understand whether underground nuclear tests could trigger earthquakes (e.g. *Emiliani et al*., 1969). Eventually, the importance of dynamic stresses on earthquake triggering and fault interactions developed into robust areas of investigation (e.g. *Harris and Day*, 1993*; Gomberg et al.*, *1997*; *Oglesby et al.*, *2003a*; *Aagaard et al*., 2004; *Gomberg and Johnson*, 2005; *Felzer and Brodsky*, 2006;

Pollitz and Johnston, 2006). While there are many sources of temporal stress fluctuations in the crust and different modes of stress transfer, for this work, the focus on dynamic stresses is twofold. First, we study how dynamic stresses from an earthquake can affect the rupture propagation path, slip, and ground motion for that specific earthquake (e.g. *Oglesby et al.*, 2003a), and second, how dynamic stresses are capable of triggering earthquakes at remote distances (e.g. *Hill et al*., 1993).

Studies that use realistically complex geometries and stresses have shown that variations in either fault geometry or stress field inputs can facilitate or hinder rupture propagation. Dynamic modeling indicates that the distance between faults affects how quickly a rupture can propagate from one fault to another, and that distances greater than 5 km are not easily jumped (*Harris and Day*, 1993). Narrow branching angles lead to the stress shadowing effect, in which shear stress is relieved on one of the faults, making rupture less likely to propagate along both branches, while wider angles tend to facilitate rupture on both branches (*Kame et al*., 2003; *Duan and Oglesby*, 2007). Dynamic stress interactions between faults during rupture can either encourage or inhibit further rupture and are highly dependent on fault geometry and pre-stress conditions (*Oglesby et al*., 2003a; 2003b). Modeling intersecting faults with differing mechanisms (i.e. strike-slip and thrust) produces propagation paths that are a complex result of the pre-stress field, the dynamic stress field, and the initial earthquake nucleation location (*Oglesby*, 2005). Small faults located between larger faults can sometimes slow, halt, or encourage rupture propagation due to differences in dynamic stress interactions that are sensitive to the length and depth of the smaller fault (*Lozos et al.*, 2012). While many of these are

examples of hypothetical fault systems that could lead to multi-fault rupture, there are several examples of real complex earthquakes in which several faults fail, such as the 1957 Gobi-Altai (*Bayarsayhan et al.*, 1996), 1992 Landers, CA (*Sieh et al*., 1993), and 2002 Denali (*Eberhart-Phillips et al*., 2003) earthquakes.

This work investigates the role of dynamic stresses on two of the major right-lateral strike-slip fault systems in southern California. The first two chapters focus on dynamic rupture models of hypothetical earthquakes along a portion of the San Andreas Fault System (SAF) within the San Gorgonio Pass (SGP) region. The final chapter investigates the possibility of remote triggering of small local events along the San Jacinto Fault Zone by dynamic stresses from far-off earthquakes.

Because two chapters discuss how the geometric complexity of the SGP affects temporal stress changes for earthquake rupture propagation, it is necessary to discuss the general geologic background of the region (Figure 0.1). Geologic maps show the SAF as the dominant structure through the SGP. (*Vaughan*, 1922) mapped the Banning Fault as linked to the SAF in the central region of the SGP (*Hill*, 1928; *Allen*, 1957). During the late Miocene, the Banning fault likely formed a single structure that was part of the SAF, but eventually the SAF became divided into three segments (*Matti et al*., 1992). The Banning fault was abandoned during the Pliocene (*Matti et al*., 1992). Sediments cover the western segment of the Banning fault and its current position is inferred from gravity data (*Willingham*, 1971). The so-called structural knot in the SGP continued to evolve during the late Pliocene and Pleistocene. A left step in the SAF began to evolve during the Pleistocene and eventually the left-lateral motion of the Pinto Mountain Fault

deflected the geometry of the SAF to its modern structure (*Matti et al.*, 1992). Multiple right-lateral slipping fault strands developed through the SGP sometimes reactivating older structures within this increasingly complex area of active faulting. The Mission

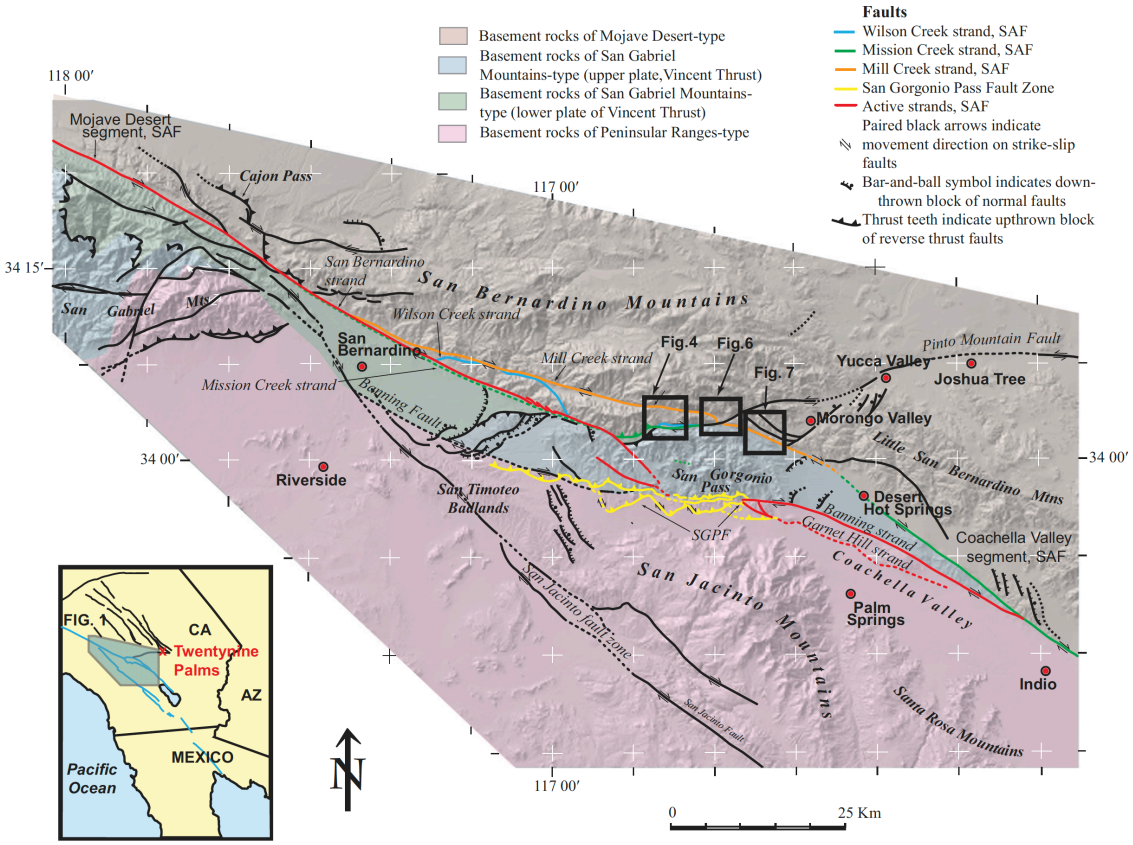

Figure 0.1. Geologic Map of Key Faults in the SGP. All annotations are original to the figure, from *Kendrick et al.* (2015). Original mapping from *Matti et al*. (1982) and *Matti and Morton* (1993).

Creek strand was one of the first to develop, but was abandoned during the Pleistocene (*Matti et al*., 1992). The Mill Creek strand developed next as the through-going strand, and while it is currently the most obvious through-going feature in the SGP, it is interpreted that the Pinto Mountain Fault displaced the Mill Creek strand, causing it to cease slipping between 106 to 95 ka (*Kendrick et al*., 2015). Toward the center of the

SGP, *Allen* (1957) mapped several faults that did not have a clear, continuous path through the area. Eventually it was proposed that the central portion of the Banning fault had been overprinted by a more geologically recent compressional tectonism that is not kinematically related to the Banning fault (*Matti et al*., 1985; *Matti et al*., 1992; *Matti and Morton*, 1993). This overprinted thrust fault system is known as the San Gorgonio Pass Fault Zone and may connect at its western end to the right-lateral Garnet Hill strand (*Yule and Sieh*, 2003). The Garnet Hill strand likely acts as a step-over with the remaining southeastern Banning Fault and Coachella Valley segment, which appears to be an offshoot of the main SAF trace that leads farther southeast toward the Salton Sea (*Matti et al.*,1992; *Yule and Sieh*, 2003). *Kendrick et al*. (2015) propose that the Pinto Mountain Fault, which has had a variable slip rate for the last 500 ka, likely caused the SAF to find a less mechanically optimal path via the San Gorgonio Pass Fault Zone and its neighboring faults. Dynamic rupture models in this work focus on this possible path through the SGP, consisting of the San Bernardino strand, San Gorgonio Pass Fault Zone, and Garnet Hill strand.

The faults in the region form a contractional stepover, which may slow or stop earthquake rupture as discussed in previous studies (e.g. *Carena et al*., 2004; *Langenheim et al*., 2005). The main active faults in the region have changed over relatively recent geologic time. Fault strands that have the strongest surface expression in the field at this time are typically older features that currently may not be the most active faults (e.g. the Mill Creek strand). Geologic mapping and paleoseismic studies indicate that thrust faults to the south may currently be the most active structures (*Yule and Sieh*, 2003; *Ramzan*,

2012, *Scharer et al*., 2013). Although recent paleoseismic trenching along the thrusts of the San Gorgonio Fault zone can provide estimates of earthquake recurrence intervals on the order of ~1400 years (*Scharer et al*., 2013), there is still considerable uncertainty about the dip angle of the thrust faults and the potential intersection with the strike-slip San Bernardino strand of the SAF. A fault intersection like the one in the western SGP has not been studied in extensive detail via dynamic rupture models. There is an extensive set of kinematic ground motion models testing rupture propagation scenarios through the SGP (e.g., *Olsen et al*., 2006; 2008), but these all assume a single, planar fault. Although simplifications are often necessary when modeling earthquakes, over-simplifications can miss important aspects of complex fault systems and provide inaccurate estimates of ground motion or propagation paths. We aim to build on the body of knowledge established in previous studies to investigate the effects of improved fault geometry and initial stress complexity through dynamic ruptures models.

References

Aagaard, B. T., G. Anderson, and K.W. Hudnut (2004), Dynamic rupture modeling of the transition from thrust to strike-slip motion in the 2002 Denali Fault earthquake, Alaska, *Bull. Seismol. Soc. Am.*, *94*, S190-S201.

Allen, C.R. (1957), San Andreas fault zone in San Gorgonio Pass, southern California, *Geol. Soc. of Am. Bull*., *68*, 319-350).

Bayarsayhan, C., A. Bayasgalan, B. Enhtuvshin, K. W. Hudnut, R. A. Kurushin, P. Molnar, and M. Ölziybat (1996), 1957 Gobi-Altay, Mongolia, earthquake as a prototype for southern California's most devastating earthquake, *Geology*, *24*(7), 579-582.

Brodsky, E. E. (2006), Long-range triggered earthquakes that continue after the wave train passes, *Geophys. Res. Lett*., *33*, L15313, doi:10.1029/ 2006GL026605.

Brodsky, E. E., E. Roeloffs, D. Woodcock, I. Gall, and M. Manga (2003), A mechanism for sustained groundwater pressure changes induced by distant earthquakes, *J. Geophys. Res*., *108*, doi:10.1029/2002JB002321.

Carena, S., J. Suppe, and H. Kao (2004), Lack of continuity of the San Andreas fault in Southern California: Three-dimensional fault models and earthquake scenarios, *Journal of Geophysical Research*, *109*, B04313, doi:04310.01029/02003JB002643.

Cocco, M. and J.R. Rice (2002), Pore pressure and poroelasticity effects in Coulomb stress analysis of earthquake interactions, *J. of Geophys. Res*., *107*, doi:10.1029/2002JB002319.

Duan, B., and D.D. Oglesby, 2007, Nonuniform prestress from prior earthquakes and the effect on dynamics of branched fault systems, *Journal of Geophysical Research*, *112*, B05308, doi:10.1029/2006JB004443.

Eberhart-Phillips, D., et al. (2003), The 2002 Denali fault earthquake, Alaska: A large magnitude, slip-partitioned event, *Science*, *300*(5622), 1113-1118.

Elkhoury, J.E., A. Niemeijer, E.E. Brodsky, and C. Marone (2011), Laboratory observations of permeability enhancement by fluid pressure oscillation of in situ fractured rock, *J. of Geophys. Res.*, *116*(B02311), doi:10.1029/2010JB007759.

Emiliani, C., C.G.A. Harrison, and M. Swanson (1969), Underground nuclear explosions, and the control of earthquakes, *Science*, *165*, 1255-1256.

Felzer, K. R. and E.E. Brodsky (2006), Evidence for dynamic aftershock triggering from earthquake densities, *Nature*, *441*, 735-738.

Gomberg, J., Blanpied, M. L. and Beeler, N. M. (1997), Transient triggering of near and distant earthquakes, *Bull. Seismol. Soc. America*, *87*, 294-309.

Gomberg, J. and P. Johnson (2005), Dynamic triggering of earthquakes, *Nature*, *437*, 830.

Harris, R. A., and S. M. Day (1993), Dynamics of Fault Interaction - Parallel Strike-Slip Faults, *J. of Geophys. Res.*, *98*(B3), 4461-4472.

Harris, R.A., R.W. Simpson, and P.A. Reasenberg (1995), Influence of static stress changes on earthquake locations in southern California, *Nature*, *375*, 221-224, doi:10.1038/375221a0.

Hill, D.P., et al. (1993), Seismicity remotely triggered by the magnitude 7.3 Landers, California, earthquake, *Science*, *260*, 1617–1623.

Hill, R.T. (1928), Southern California geology and Los Angeles earthquakes, *Los Angeles Southern California Academy of Sciences*, 232.

Kame, N., J. R. Rice, and R. Dmowska (2003), Effects of pre-stress state and rupture velocity on dynamic fault branching, *Journal of Geophysical Research*, *108*(B5), 2265, doi: 2210.1029/2002JB002189.

Kendrick, K.J., J.C. Matti, and S. Mahan (2015), Late Quaternary slip history of the Mill Creek strand of the San Andreas fault in San Gorgonio Pass, southern California: The role of a subsidiary left-lateral fault in strand switching, Geol. Soc. of Am. Bull, 127, 825-849, doi:10.1130/B31101.1.

King. G.C.P., R.S. Stein, and J. Lin (1994), Static stress changes and the triggering of earthquakes, *Bull. Seismol. Soc*. *America*, *84*, 935-953.

Langenheim, V. E., R. C. Jachens, J. C. Matti, E. Hauksson, D. M. Morton, and A. Christensen (2005), Geophysical evidence for wedging in the San Gorgonio Pass structural knot, southern San Andreas fault zone, Southern California, *Geological Society of America Bulletin*, *117*.

Lozos, J. C., D. D. Oglesby, J. N. Brune, and K. B. Olsen (2012), Small intermediate fault segments can either aid or hinder rupture propagation at stepovers, *Geophysical Research Letters*, *39(*18), DOI: 10.1029/2012GL053005.

Matti, J. C., and D. M. Morton (1993), Paleogegraphic evolution of the San Andreas fault in Southern California: A reconstruction based on a new cross-fault correlation, in *The San Andreas fault system: Displacement, palinspastic reconstruction, and geologic evolution*, edited by R. E. Powell, R. E. I. Weldon and J. C. Matti, pp. 107-159, Geological Society of America.

Matti, J.C., B.F. Cox, C.M., Obi, R.E. Powell, M.E. Hinkle, Griscom, Andrew, and E.L. McHugh, (1982), Mineral resource potential of the Whitewater Wilderness Study Area, Riverside and San Bernardino Counties, California, *U.S. Geological Survey Miscellaneous Field Studies Map MF-1478*, scale 1:62,500.

Matti, J.C., D.M. Morton, and B.F. Cox (1985), Distribution and geologic relations of fault systems in the vicinity of the central Transverse Ranges, southern California, *U.S. Geological Survey Open-File Report 85-365*, 27, scale 1:250,000.

Matti, J.C., D.M. Morton, and B.F., Cox (1992), The San Andreas fault system in the vicinity of the central Transverse Ranges Province, southern California, U.S. Geological Survey Open-File Report 92-354, 40, scale 1:250,000.

Nordke, M.D. (1975), A review of Soviet data on the peaceful uses of nuclear explosions, *Annals of Nuclear Energy*, *2*, 657-673.

Oglesby, D. D. (2005), The dynamics of strike-slip step-overs with linking dip-slip faults, *Bulletin of the Seismological Society of America*, *95*(5), 1604-1622.

Oglesby, D.D., S.M. Day, Y.-G. Li, and J.E. Vidale (2003a), The 1999 Hector Mine earthquake: the dynamics of a branched fault system, *Bulletin of the Seis. Soc. of Am.*, *93*(6), 2459-2476.

Oglesby, D.D., S.M. Day, and D.R.H. O'Connell (2003b), The dynamic and static interaction of two thrust faults: a case study with general implications, *Journal of Geophysical Research*, *108* (B10), 2489, doi:10.1029/2002JB002228.

Olsen, K. B., S. M. Day, J. B. Minster, Y. Cui, A. Chourasia, D. Okaya, P. Maechling, and T. Jordan (2008), TeraShake2: Spontaneous rupture simulations of M-w 7.7 earthquakes on the southern San Andreas fault, *Bulletin of the Seismological Society of America*, *98*(3), 1162-1185.

Olsen, K. B., S. M. Day, J. B. Minster, Y. Cui, A. Chourasia, M. Faerman, R. Moore, P. Maechling, and T. Jordan (2006), Strong shaking in Los Angeles expected from southern San Andreas, *Geophysical Research Letters*, *33*, L07305, doi:07310.01029/02005GL025472.

Oppenheimer, D.H., P.A. Reasenberg, and R.W. Simpson (1988), Fault plane solutions for the 1984 Morgan Hill, California, earthquake sequence: evidence for the state of stress on the Calavaras fault, *J. of Geophys. Res.*, *93*, 9007-9026.

Pollitz, F.F. and I.S. Sacks (2002), Stress triggering of the 1999 Hector Mine earthquake by transient deformation following the 1992 Landers earthquake, *Bull. Seismol. Soc. America*, 92(4), 1487-1496.

Pollitz, F.F. and M.J.S Johnston (2006), Direct test of static stress versus dynamic stress triggering of aftershocks, *Geophys. Res. Lett*., *33*, doi: 10:1029GL026764.

Ramzan, S. (2012), Paleoseismic investigation of the San Gorgonio Pass fault zone near Cabazon, California, M.S. Thesis: California State University, Northridge.

Scharer, K. M., D. Yule, L. R. Humbert, R. Witkowsky (2013), Implications for San Andreas Fault Ruptures Based on New Evidence from the Cabazon, CA Paleoseismic Site, San Gorgonio Pass Fault Zone, *American Geophysical Union, Fall Meeting 2013*, abstract #T43A-2622.

Sieh, K. E., L. Jones, et al. (1993), Near field investigation of the Landers earthquake sequence, April to July 1992, *Science*, *260*(5105), 171-176.

Stuart, W.D. (1979), Quasi-static earthquake mechanics, *Review of Geophysics*, *17*(6), 1115-1120, doi:10.1029/RG017i006p01115.

Vaughan, F.E. (1922), Geology of the San Bernardino Mountains north of San Gorgonio Pass, *California University Publications in Geological Sciences*, *13*, 319-411.

Wang C. Y., and M. Manga (2009), Hydrologic response to earthquakes and a general metric, *Geofluids*, *10*, 206-216.

Willingham, R.C. (1971), Basement fault geometries in the San Bernardino Valley and western San Gorgonio Pass area, southern California, *Geol. Soc. of Am. Abstracts with Programs*, *3*(2), 217.

Yule, D., and K. E. Sieh (2003), Complexities of the San Andreas fault near San Gorgonio Pass: Implications for large earthquakes, *J. of Geophys. Res.*, *108*(B11), doi:10.1029/2001JB000451.

Chapter 1

Testing Simplified Fault Geometries to Understand Fault Interactions in San Gorgonio Pass, CA via Dynamic Rupture Models

1.1. Abstract

We use 3D dynamic finite element method models to investigate potential rupture paths of earthquakes propagating along faults in the western San Gorgonio Pass (SGP) region of California. The SGP is a structurally complex region because the San Andreas Fault splinters into many sub-parallel active fault strands with additional active fault zones present in this location. It has long been suspected that this structural knot, which consists of the intersection of various non-planar strike-slip and thrust fault segments, may inhibit earthquake rupture propagation between the San Bernardino strand of the San Andreas Fault System and the San Gorgonio Pass Fault Zone. The above condition may limit the size of potential earthquakes in the region. We focus this study on a highly simplified approximation of the San Bernardino strand and the San Gorgonio Pass Fault Zone, where the fault connectivity is not well-constrained. We use the finite element method code FaultMod (*Barall*, 2009) to investigate how fault geometry, nucleation location, and initial stresses influence rupture propagation, which could be an indicator of the likelihood of through-going rupture in this region. Our results indicate that earthquakes that nucleate on the San Bernardino strand and propagate southeastward do not easily transfer rupture to thrust faults of the San Gorgonio Pass Fault Zone. However, with certain fault geometry assumptions, earthquakes that nucleate on the San Gorgonio Pass Fault Zone may transfer rupture to the San Bernardino strand. Thus, these results imply that through-going rupture may be more likely if an earthquake nucleates on the eastern side of the San Gorgonio Pass Fault Zone and the distance between the San Bernardino strand and the thrust faults of the San Gorgonio Pass Fault Zone is small.

1.2. Introduction

The San Gorgonio Pass (SGP) is a structurally complex region along the San Andreas Fault system (SAF) in southern California. Based on mapped surface traces through the SGP (Figure 1.1), the SAF does not have an obvious continuous surface expression through the area. Strike-slip and thrust faults appear discontinuous and many

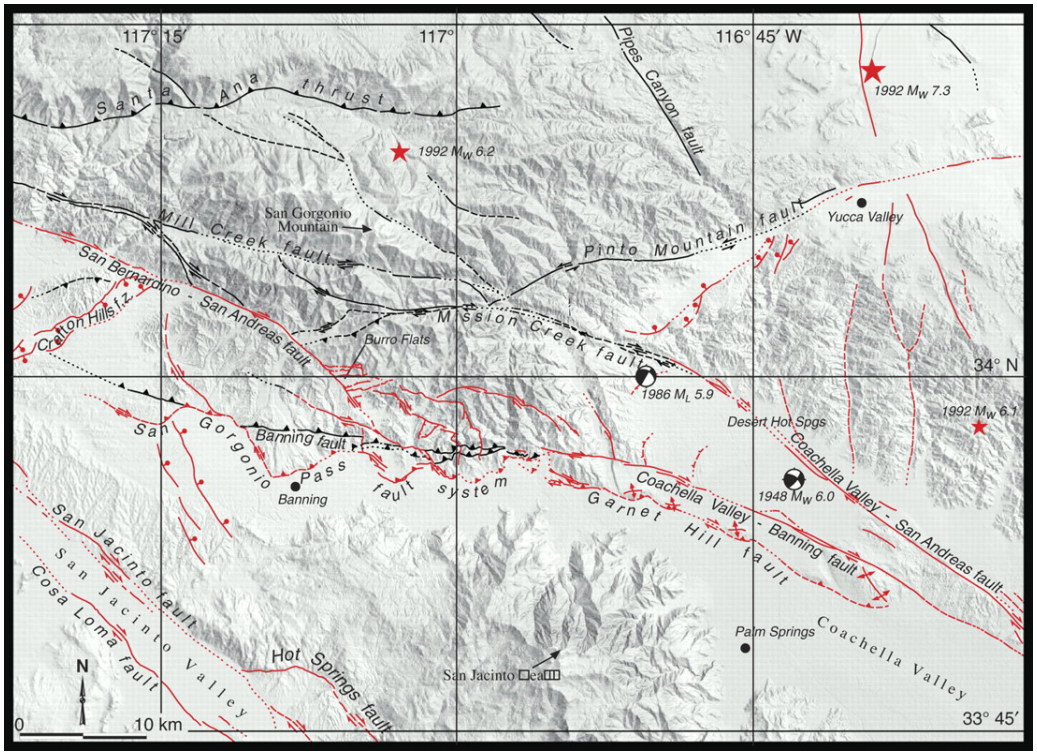

Figure 1.1. Location and Fault Map. Red lines show active fault traces; black are deemed inactive. All annotations are original to the figure (Yule and Sieh, 2003). Original mapping by Allen (1957), Matti et al. (1985), Matti et al. (1992), Matti and Morton (1993).

of the intersections amongst the various mapped traces are unclear (*Allen*, 1957; *Matti et al.*, 1985; *Matti and Morton*, 1993; *Yule and Sieh*, 2003). The SGP is a crucial "pinch-point" along the SAF because its structural complexity could lead to two extreme end-members of results. It could halt rupture propagation (*Sykes and Seeber*, 1985) or cause a complex earthquake in which several faults fail, as in the 1957 Gobi-Altai (*Bayarsayhan*

et al., 1996), 1992 Landers, CA (*Sieh et al*., 1993), and 2002 Denali (*Eberhart-Phillips et al*., 2003) earthquakes. The entirety of the southern SAF has not ruptured in modern seismically recordable history, leaving much speculation about the characteristics of potentially large earthquakes in the SGP region. If the entirety of the southern SAF, including the SGP, were to fail, large parts of southern California, including metropolitan areas, would experience strong shaking (*Olsen et al*., 2006). The sediments along the San Bernardino and San Gabriel Mountains act as a waveguide, funneling seismic radiation into the metropolitan areas built on basins that further amplify shaking. One of the fundamental questions in the literature regarding the SGP is whether a large through-going earthquake is possible in this region. If such a through-going rupture is possible, another important question is what circumstances (i.e. fault geometry, stress conditions, and nucleation locations) could increase the likelihood of such an event. To design a model that adequately addresses the circumstances that could lead to through-going earthquakes, it is necessary to first characterize the geologic complexities of the SGP and then decompose the complexities into a manageable starting point.

1.2.1. Geologic Complexities of the SGP

Strike-slip faults, thrust faults, and even normal faults comprise the active fault network of the SGP. The predominant faulting mechanisms are right-lateral strike-slip and thrust. In general, the faults in the region form a contractional stepover, which may slow or stop earthquake rupture (*Carena et al*., 2004; *Langenheim et al*., 2005). The main active faults in the region have changed over relatively recent geologic time. Fault

strands that have the strongest surface expression in the field at this time are typically older features that currently may not be the most active faults (e.g. the Mill Creek strand). Geologic mapping and paleoseismic studies indicate that thrust faults to the south may be the current most active structures (*Yule and Sieh*, 2003; *Ramzan*, 2012, *Scharer et al*., 2013). Although recent paleoseismic trenching along the thrusts of the San Gorgonio Fault zone can provide estimates of earthquake recurrence intervals on the order of ~1400 years (*Scharer et al*., 2013), there is still considerable uncertainty about the dip angle of the thrust faults and the potential intersection with the strike-slip San Bernardino strand of the SAF. The complexity of the SGP can be broken down into several areas that may each serve as a pinch-point for rupture propagation. One such area is the possible intersection between the San Gorgonio Pass Fault Zone and the San Bernardino strand of the SAF, henceforth referred to as the San Bernardino strand. At this possible intersection, the right-lateral San Bernardino strand terminates almost like a tear fault between two thrust faults in the San Gorgonio Pass Fault Zone, which are oriented nearly perpendicular to the San Bernardino strand (Figure 1.2). This study aims to understand the dynamic fault interactions in this particular area of the western SGP.

Paleoseismic data yield large uncertainties regarding the timing of earthquakes and cannot unequivocally determine dynamic fault interactions. Evidence of paleoseismic events can be difficult to correlate spatially and temporally. For example, features found in trenches both in the eastern and western SGP could either indicate that a large through-going earthquake occurred, or that smaller events occurred with days or even years passing between the events. The error associated with dating paleoseismic features

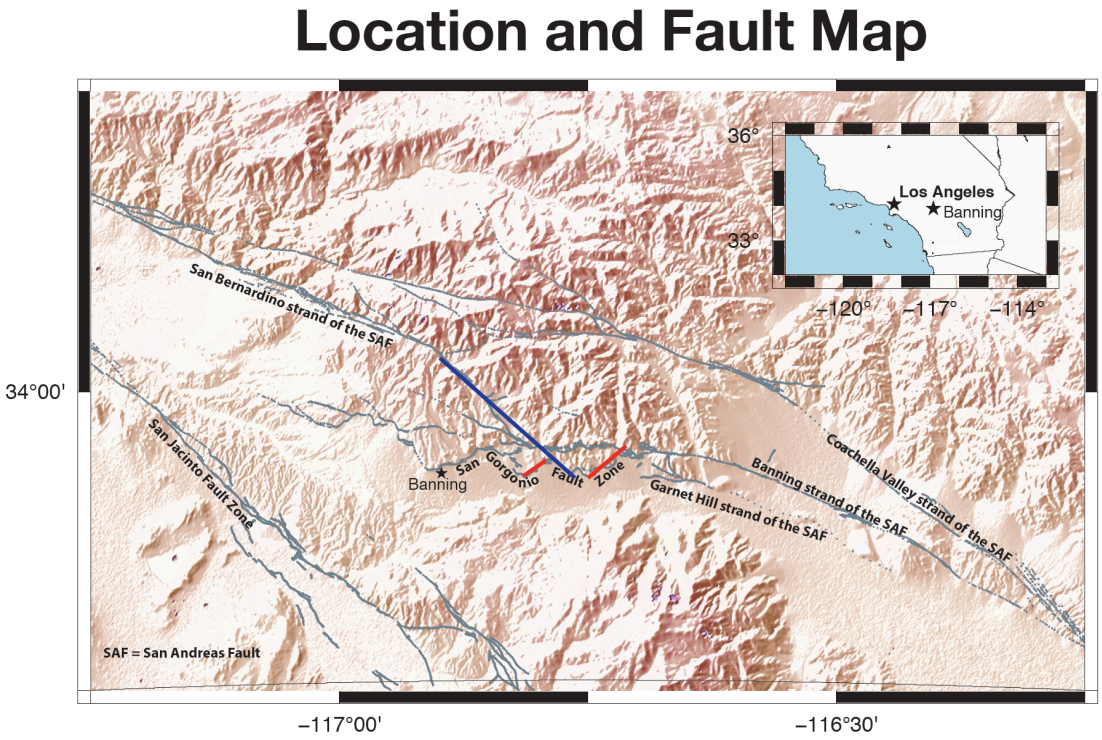

Figure 1.2. Location and Fault Map Showing Model Approximation. The blue and red lines show the approximation of the fault geometry made for the models. The blue line is the equivalent of the Strike-Slip Fault and the red lines are the Western and Eastern Thrusts in the models.

sometimes spans centuries, leaving the results open to several interpretations (e.g. *Scharer et al*., 2013). Numerical modeling is one way of investigating the likelihood of through-going rupture and can validate interpretations from the geologic record.

A fault intersection like the one in the western SGP has not been studied in extensive detail via dynamic rupture models. There is an extensive set of kinematic ground motion models testing rupture propagation scenarios through the SGP (e.g., *Olsen et al*., 2006; 2008), but these all assume a single, planar fault. Although simplifications are often necessary when modeling earthquakes, over-simplifications can miss important aspects of complex fault systems and provide inaccurate estimates of ground motion or

propagation paths. Studies that use more realistically complex geometries and stresses, but are not specific to the SGP region, have shown that variations in either fault geometry or stress field inputs can facilitate or hinder rupture propagation. Dynamic modeling indicates that the distance between faults affects how quickly a rupture can propagate from one fault to another, and that distances greater than 5 km are not easily jumped (*Harris and Day*, 1993). The branching angle between faults in a branched fault system can affect propagation paths. Narrow branching angles lead to stress shadows, in which stress is relieved on one of the faults, making rupture less likely to propagate along both branches; wider angles tend to facilitate rupture on both branches (*Kame et al*., 2003; *Duan and Oglesby*, 2007). Stress interactions between faults during rupture can either facilitate or terminate further rupture and are highly dependent on fault geometry and pre-stress conditions (*Oglesby et al*., 2003a; 2003b). Modeling intersecting faults with differing mechanisms (i.e. strike-slip and thrust) produces propagation paths that are a complex result of the pre-stress field, the dynamic stress field, and the initial earthquake nucleation location (*Oglesby*, 2005). Small faults located between larger faults can sometimes hinder or facilitate rupture propagation due to differences in dynamic stress interactions that are sensitive to the length and depth of the smaller fault (*Lozos et al.*, 2012). Models of strike-slip faults intersecting dipping thrust and normal faults show that slip on strike-slip faults could hinder rupture on nearby thrust faults, while the opposite is true for slip originating on thrust faults (*Oglesby*, 2005). However, the results of these previous models depend on the specific fault geometry and pre-stress fields used in those models, so they cannot adequately answer whether earthquakes can continue through a

specific intersection similar to the San Bernardino strand and San Gorgonio Fault zone, or what circumstances lead to through-going scenarios. Due to the uncertainty on the exact orientation of active fault structures in the area, dynamic rupture modeling is a suitable method to explore the possible variations of fault geometry in the SGP and the effect of those variations on earthquake propagation. Models in this study test six types of variation as follows: (1) the distance separating thrust faults from the strike-slip fault, (2) the size of the thrust faults, (3) the dip angles of the thrust faults, (4) the location of the potential fault intersection, (5) the nucleation location, and (6) the initial stress field. This study aims to maintain the simplest geometries possible for the San Bernardino strand and San Gorgonio Pass Fault Zone while testing multiple variations on that fault geometry.

1.3. Methods

There are various modeling methods used to investigate earthquake and fault behavior. The methods can generally be grouped into kinematic, quasi-static, and dynamic models. Kinematic faulting models assume fault displacement to calculate ground motion (e.g. *Michael*, 1990; *Wesnousky and Jones*, 1994), but fault motion must be specified beforehand. Quasi-static faulting models allow for the estimation of fault motion and stress transfer, but the assumption is that all elements of the model are in stress equilibrium, assuming no acceleration, so the sum of all forces is equal to zero. Such models are useful for determining the relative change in the regional stress field after an earthquake (e.g. *King et al*., 1994) because they solve for the difference in forces

between the beginning and end of the simulation. Because of their computational efficiency, fault motion and deformation can be modeled over long periods of time with quasi-static models (e.g. *Dair and Cooke*, 2009). However, quasi-static models do not incorporate seismic waves, so they cannot be used to determine ground motion, and do not include the complex interaction between dynamic stress waves and fault friction. Dynamic models fully consider the time-varying interaction between motion, forces, and material properties. Results are stepped forward in time, with the result from one time step affecting the result in the next time step. Dynamic modeling, due to its computational expense, cannot easily model long-term faulting behavior. However, it is an approach well-suited to investigate potential earthquake rupture propagation paths in the SGP over the time frame of a single earthquake because dynamic rupture models can explore the effects of fault geometry on slip distribution, propagation paths over time, ground motion, and earthquake size (*Aochi et al*., 2000; *Aagaard et al*., 2004; *Oglesby et al*., 2003a; 2003b; *Oglesby*, 2005; *Duan and Oglesby*, 2007; *Templeton*, 2009; *Lozos et al*., 2011; *Lozos et al*., 2012).

1.3.1. Basics of the Modeling Method

We use the 3D finite element method code FaultMod (*Barall*, 2009) to run all models in this study. FaultMod takes the following as basic inputs: 3D mesh, friction law, stresses, nucleation location (hypocenter), material properties, model duration, and time stepping. Using these inputs, FaultMod solves for displacement at the nodes of the elements, and for stresses at the element faces. In general, the calculations rely on

Newton's second law of motion and Hooke's law, which provides the relationship between strain and stress (*Taylor*, 2005; *Mac Donald*, 2007; *Zhang et al*., 2009). The outputs are absolute normal and shear stresses, slip, slip rate, and particle/ground motion. Total slip in particular is a useful output because it best emphasizes the rupture propagation paths for each model.

1.3.2. Mesh Designs and Relevant Parametric Assumptions

The San Bernardino strand of the SAF (hereafter referred to as the Strike-Slip Fault) and two thrust segments of the San Gorgonio Fault Zone (hereafter referred to as the Western Thrust or Eastern Thrust when referred to individually or as the thrusts when referred to together) were selected as the faults of interest due to their orientations. The fault traces for the geometries used in this study are simplified from the fault structures of the western SGP as shown in Figure 1.2. The Strike-Slip Fault is oriented at a 90-degree angle between the two thrusts. Based on mapping studies, it is uncertain how, or even if, these faults intersect (*Matti et al*., 1985; *Matti and Morton*, 1993; *Yule and Sieh*, 2003). The fault geometries used in this study are approximated with planar faults for simplicity. We discretize the faults and mesh the volume surrounding the faults in the csimsoft software toolkit Trelis, which is based on CUBIT software from Sandia National Laboratories. Fault surfaces are meshed with triangular elements, and the volumes are meshed with tetrahedra. Bias is implemented so that elements far from the faults are three times larger than elements around the faults to save on computational time and storage space. We generate two general categories of meshes for this study. The Test

Category #1 (T1) meshes have thrusts with a short along-strike length and a 1-2 km separation from the Strike-Slip Fault (Figure 1.3a). The Test Category #2 (T2) meshes are similar, but include thrusts with larger along-strike lengths compared to the T1 geometry and only a 100 m separation from the Strike-Slip Fault (Figure 1.3b). The T2 thrusts are extended to approximate the larger length of the San Gorgonio Pass Fault Zone and facilitate tests of earthquakes that may nucleate farther away from the potential intersection point of all faults involved in the models. There are also two variations with the length of the Strike-Slip Fault, which changes the potential intersection point with the thrusts (Figure 1.4) such that it terminates either near the Eastern or Western thrust segment. These variations are referred to as the gap and no gap scenarios. For all meshes, dip angles of 35, 45, and 55 degrees for both thrusts are tested. In total, there are 12 unique geometry combinations for all of the models tested in this study (Table 1.1). While still relatively simple, these variations of the fault geometry add more realistic complexity to models through the SGP when compared to models assuming a single planar fault through the region. These models also enhance our intuition for the factors that control the propagation of rupture across these faults.

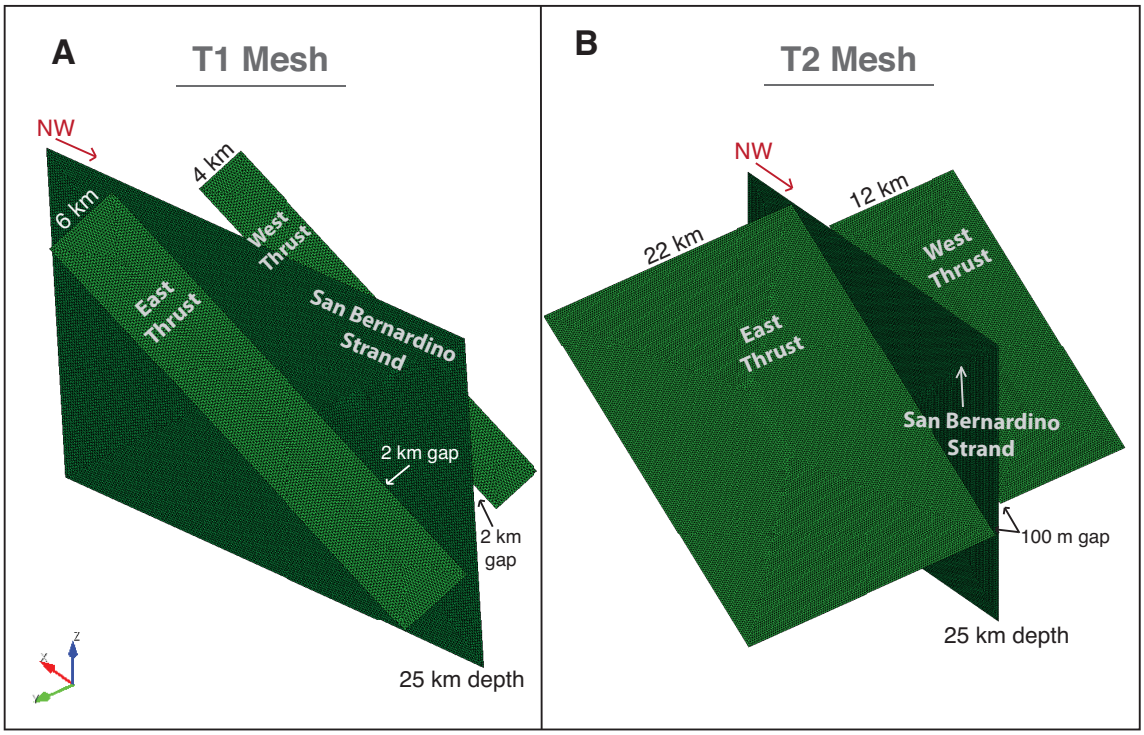

Figure 1.3. T1 and T2 Mesh Varieties. In general, the T2 mesh is the preferred mesh because the larger along-strike length of the thrusts allows directivity to play a larger role in the models, providing a closer match to the actual fault system. The T2 mesh also has a smaller gap between the thrusts and the Strike-Slip fault, labeled as the San Bernardino strand here. The along strike-length of the Strike-Slip fault for both meshes ranges from 20-24 km (see Figure 1.4) and both are meshed with 200 m-sized elements.

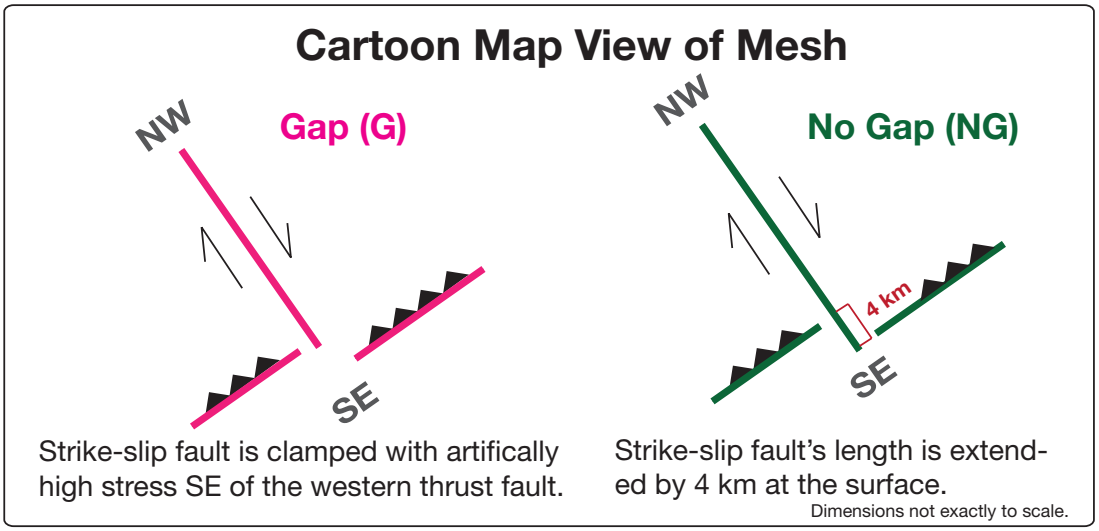

Figure 1.4. Map View of Gap and No Gap Scenarios. The map view of the gap scenario (pink) shows which how far the Strike-Slip fault extends. At depth, the Strike-Slip fault is clamped along the angle of the thrusts, even though the full mesh geometry will be visible in subsequent figures.

For these tests, the objective is to obtain potential earthquake rupture propagation paths. In addition to the fault geometry variations, we test various initial stress conditions as well, using the slip-weakening friction law (*Ida*, 1972; *Andrews*, 1976). The results of the models are divided into two main categories based on their initial stress inputs: Constant Tractions and Regional Stress. Both the Constant Tractions and Regional Stress models are further subdivided in the results section. In the Constant Tractions models, the Strike-Slip Fault is pre-stressed in a purely strike-slip manner and the thrusts are pre-stressed in a purely dip-slip manner. There is no assumption of oblique slip, but faults are allowed to slip in any direction based on the dynamic solution. We refer to these models as having constant tractions because the initial shear along-strike traction value is the same for every element along the Strike-Slip fault, as is the initial normal traction value. Likewise, the thrusts have the same initial shear along-dip traction values. A detailed breakdown of the stress values is in Table 1.2. With constant frictional parameters, we back-calculate the magnitude of the initial constant shear and normal tractions assuming a 3 MPa stress drop. Our physical and computational parameters for the Constant Tractions models are listed in Table 1.2.

With the Regional Stress models we use a constant tectonic stress field for the SGP region as the initial condition, with the shear and normal stress on each fault segment resolved from this observationally-based regional stress tensor onto each segment. This method adds another layer of complexity because oblique slip is possible in this scenario, and stress magnitudes are no longer equivalent on different segments. To obtain the initial regional stress values, we use the orientation of the stress field and

the relative magnitude of the three principal stress axes (A_ϕ) of the SGP area from *Hardebeck and Hauksson* (2001). We use the A_ϕ parameter as defined in Simpson (1997) to calculate ratios of initial stresses that fall within the range of $A_\phi = 1.5 – 2.3$, which is an appropriate range for the SGP (*Hardebeck and Hauksson*, 2001). The 1.5 – 2.3 range indicates a mixture of a strike-slip and thrust regime, with 2.3 having the higher compressive component because $A_\phi \approx 3$ indicates pure compression. We use 4 different sets of initial stress tensors that correspond to the following four A_ϕ values: 1.5, 1.74, 1.96, and 2.24. We then resolve the regional stress tensors onto the fault planes in FaultMod. Our physical and computational parameters for the Regional Stress models are listed in Table 1.3. We keep as many parameters as possible constant between the Constant Tractions and Regional Stress models, but the frictional parameters need to be somewhat different for the these two model suites in order to maintain S values that can facilitate rupture.

1.4. Results

The model results are divided into four groups with successively increasing complication: T1 mesh models, shallow T2 mesh models, an expanded set of T2 mesh models with various nucleation depths, and T2 mesh models that employ a variety of regional stress regimes. Overall, our results indicate that earthquakes nucleating on the Strike-Slip Fault do not easily transfer rupture to the thrust faults. However, the thrust faults may transfer rupture to the Strike-Slip Fault. Through-going rupture is more

common in the scenarios in which an earthquake nucleates on the Eastern Thrust and the distance between the Strike-Slip Fault and the thrusts is small.

1.4.1. T1 Set of Models

This category of models includes thrust dip angles of 35, 45, and 55 degrees; the gap and no gap fault intersections (Figure 1.4); and three different nucleation locations. The nucleation locations are on the Strike-Slip Fault, the Western Thrust, and the Eastern Thrust. All nucleation locations are at a depth of roughly 3 km. We find that the models with different thrust dip angles produce similar results, suggesting that the 20-degree variation in dip between different classes of our models does not significantly affect rupture propagation paths with this fault geometry. Instead, the nucleation locations and proximity of the Strike-Slip Fault to the thrusts have the most effect on rupture propagation paths. With models that have nucleation points on the Strike-Slip Fault, rupture does not propagate to either of the thrusts. Right-lateral slip on the Strike-Slip Fault causes an increase in normal stress on the Eastern Thrust and a decrease in normal stress on the Western Thrust. Although the change in normal stress should bring the Western Thrust closer to failure, the dynamic shear stress values remain relatively low compared to the normal stress. At the end of the simulation, shear stress values are actually lower on the Western Thrust than on the Eastern Thrust. This is likely due to the fault placement in the T1 mesh; the Western Thrust is 4 km away from the Strike-Slip Fault and the Eastern Thrust only 2 km away. Complete multi-fault rupture also does not occur in models that nucleate on the Western Thrust. Slip on the Western Thrust does

not significantly affect normal stress on the Strike-Slip Fault. However, the dynamic shear stresses on the Strike-Slip Fault are complex; patches of the fault closer to the surface (and closer to the Western Thrust) experience a decrease in shear stress, while parts of the fault farther away from the Western Thrust (to the northwest) experience an increase in shear stress. Overall, with rapid temporal changes in the shear stress, the shear stress magnitude on the Strike-Slip Fault does not exceed the normal stress magnitude for prolonged periods of time in models that nucleate on the Western Thrust. Conversely, rupture nucleation on the Eastern Thrust (i.e. the southeast) facilitates large shear stress increases on the Strike-Slip Fault, which leads to more complex rupture propagation paths (Figure 1.5). In each of the models that included nucleation on the Eastern Thrust, at least part of the Strike-Slip Fault also slipped. Figure 1.5 shows a model with a 35-degree dip angle for the thrusts and nucleation on the Eastern Thrust. The pale blue region at 1 second shows the nucleation location. At 3 seconds, rupture has jumped across the 1 km gap between the faults to the Strike-Slip Fault. At 9 seconds, the rupture dies on the Eastern thrust, but the Strike-Slip fault continues to rupture until the earthquake ends at 12 seconds. Due to the relatively small along-strike length of the Eastern Thrust, we test the effects of the nucleation radius on the results. Decreasing the nucleation radius to 3 km for the model in Figure 1.5 does not stop the rupture from jumping across to the Strike-Slip Fault. In comparison, using a 5 km nucleation radius on the Western Thrust, which is smaller along strike than the Eastern thrust, does not lead to multi-fault rupture, indicating that the nucleation radius does not significantly affect our results. The 2 km gap between the Western Thrust and the Strike-Slip Fault, plus the

aforementioned clamping effect between the two faults prevent the rupture from expanding beyond the Western Thrust. This suggests that the combined faulting mechanisms and fault geometry have significant effects on the results.

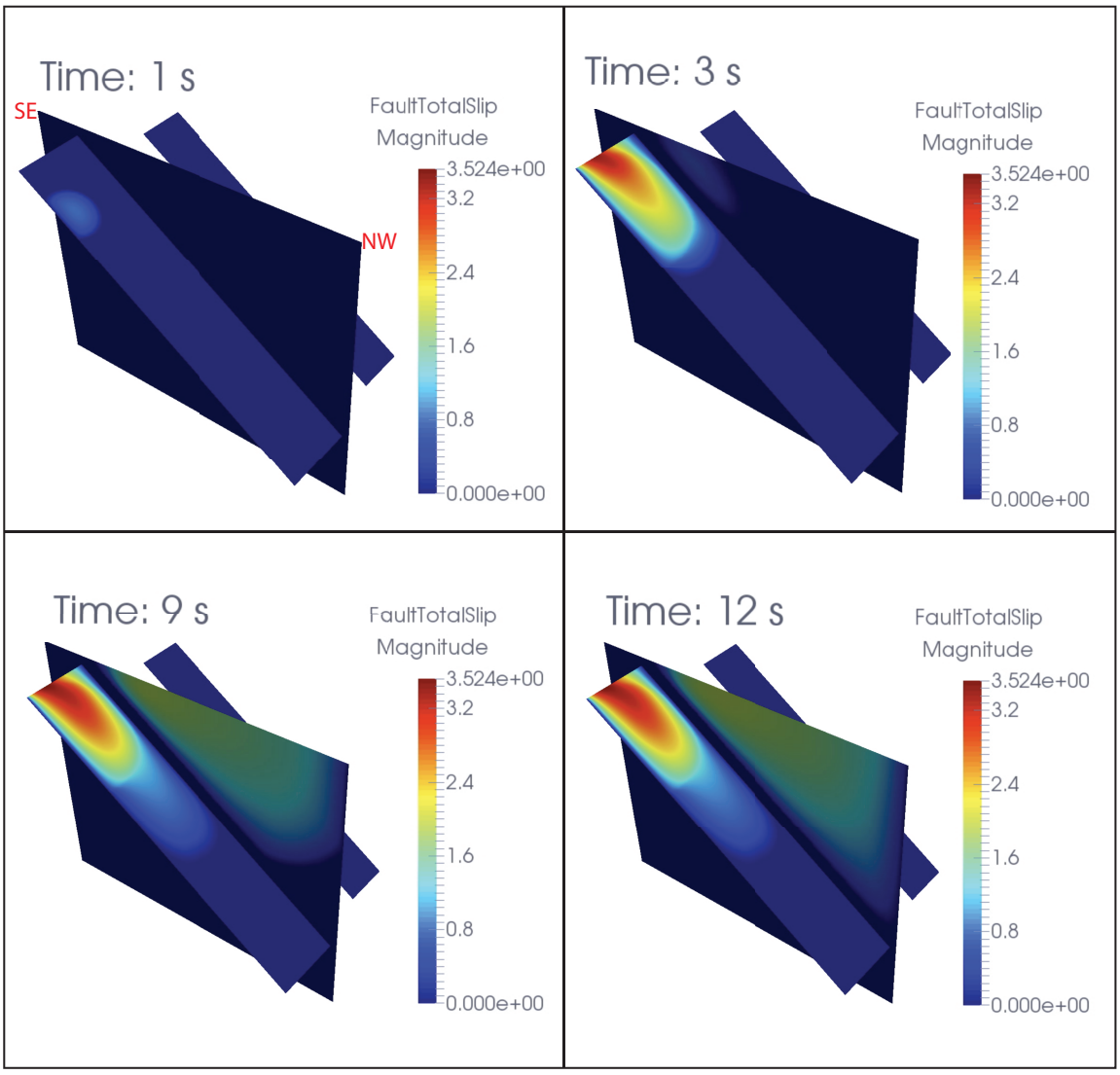

Figure 1.5. Total Slip Plots for T1 Example Model. Note the view is from the northeast direction, so the left corner shows the southeast direction. This model uses a T1 mesh, 35-degree dipping thrust faults, the no gap scenario, and nucleation on the Eastern Thrust. In this scenario, rupture jumps to the Strike-Slip Fault. Fault Total Slip Magnitude is given in meters. This scenario is approximated to be a M_w 6.7.

Figure 1.5 is also an example of a model where the Strike-Slip Fault is extended 4 km south for a total length of roughly 24 km, otherwise referred to as the no gap scenario. The no gap scenario decreases the distance between the Eastern Thrust and the Strike-Slip Fault, facilitating a build of up shear stress along the Strike-Slip Fault that leads to multi-fault rupture. With the T1 mesh configuration, we find that with nucleation on either of the thrusts, the no gap scenario tends to increase shear stresses on the Strike-Slip Fault, resulting in an increased likelihood of multi-fault rupture. In general, nucleating on the Eastern Thrust and having a no gap scenario for the fault geometry create stress conditions that are more favorable for multi-fault rupture. The results of all the models generated with a T1 mesh are summarized in section 1.4.3: Comparison Between T1 and T2 Models.

1.4.2. Basic Set of T2 Models

This and subsequent categories of models only employ the T2 mesh. Again, the varieties include thrust dip angles of 35, 45, and 55 degrees; the gap and no gap fault intersections; and three different nucleation locations. Unlike the results of the T1 set of models, we find that the difference in dip angles on the thrusts can impact rupture. As shown in Figures 1.6-1.8, increasing the dip angle facilitates multi-fault rupture for earthquakes that nucleate on the Eastern Thrust. Figure 1.6 shows the total slip plots for a T2 mesh model with 35-degree dip angles on the thrusts and a no gap intersection. Similar to the T1 model in Figure 1.5, at 3 seconds, the rupture propagates to the Strike-Slip Fault.

In this scenario, rupture terminates on the Eastern Thrust by 11 seconds and terminates on the Strike-Slip Fault by 15 seconds. If the dip angle on the thrusts is increased to 45 degrees, all three faults fail (Figure 1.7). The rupture propagates from the Strike-Slip Fault to the Western Thrust by 13 seconds, but is just barely visible at the viewing angle of Figure 1.7 at around 15 seconds. The earthquake takes nearly 25 seconds to end. Changing the thrust dip angle to 55 degrees appears to be the most favorable for multi-fault rupture with nucleation on the Eastern Thrust (Figure 1.8). In the 55-degree scenario, the rupture jumps to the Strike-Slip Fault by 9 seconds and the entire earthquake is over at 16 second. The dynamic shear stresses that cause the rupture to jump increase to failure significantly faster in the 55-degree scenario compared to the 45-degree scenario. Conversely, while increasing the dip angle promotes multi-fault rupture with nucleation on the Eastern Thrust, increasing the dip angle inhibits multi-fault rupture for earthquakes that nucleate on the Western Thrust with the no gap scenario. With nucleation on the Western Thrust, although unclamping is favored along most of the Strike-Slip Fault, there is a slight increase in normal stress along the Strike-Slip Fault to the south of the Western Thrust in the no gap scenario with larger dip angles. This may account for slip termination, considering that dynamic shear stresses are lower on the Western Thrust compared with the Eastern Thrust. Thus, although the dip angle variations lead to different results in the T2 set of models, the difference in the results is still strongly tied to the nucleation location.

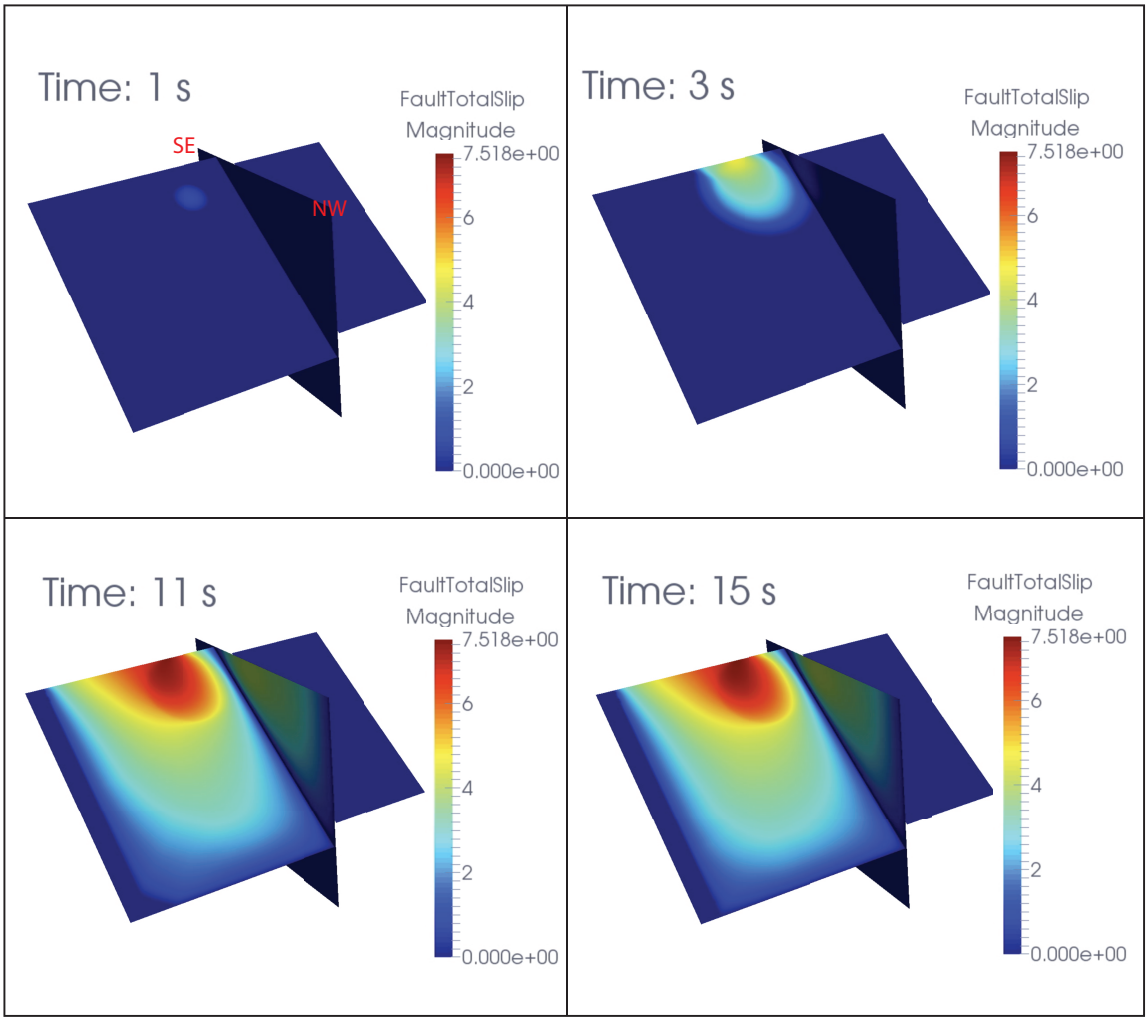

Figure 1.6. Total Slip Plots for T2 35 Degree Dip Model. This model assumes a T2 mesh, 35-degree dipping thrust faults, nucleation on the Eastern Thrust, and the no gap scenario. Fault total slip magnitude is given in meters. Total earthquake time is only three seconds longer than the comparable T1 mesh model.

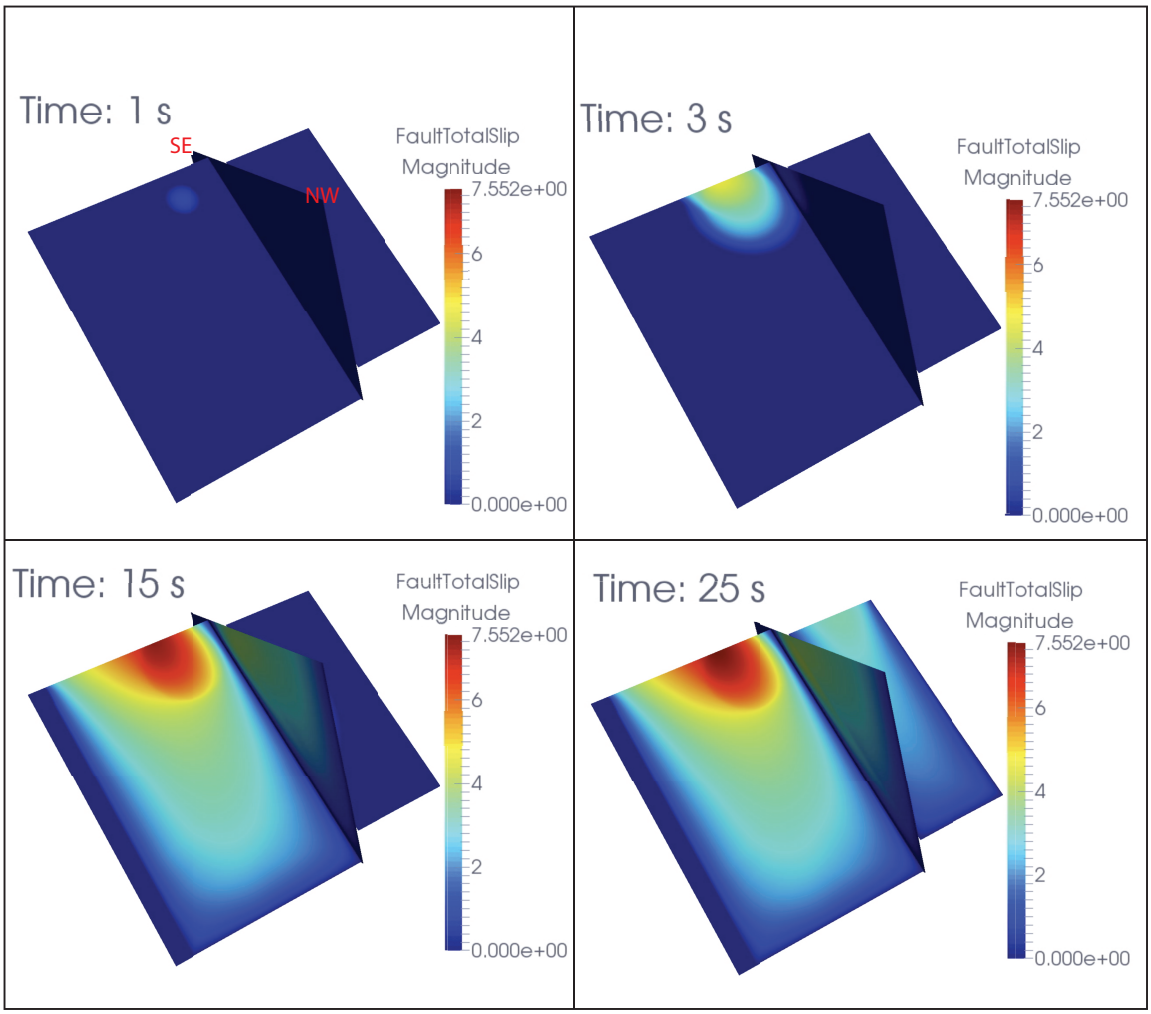

Figure 1.7. Total Slip Plots for T2 45 Degree Dip Model. This model assumes a T2 mesh, 45-degree dipping thrust faults, nucleation on the Eastern Thrust, and the no gap scenario. Fault total slip magnitude is given in meters. This scenario is approximated to be the equivalent of a M_w 7.3, corresponding to the maximum-slip scenario from the T2 suite of models employing constant tractions.

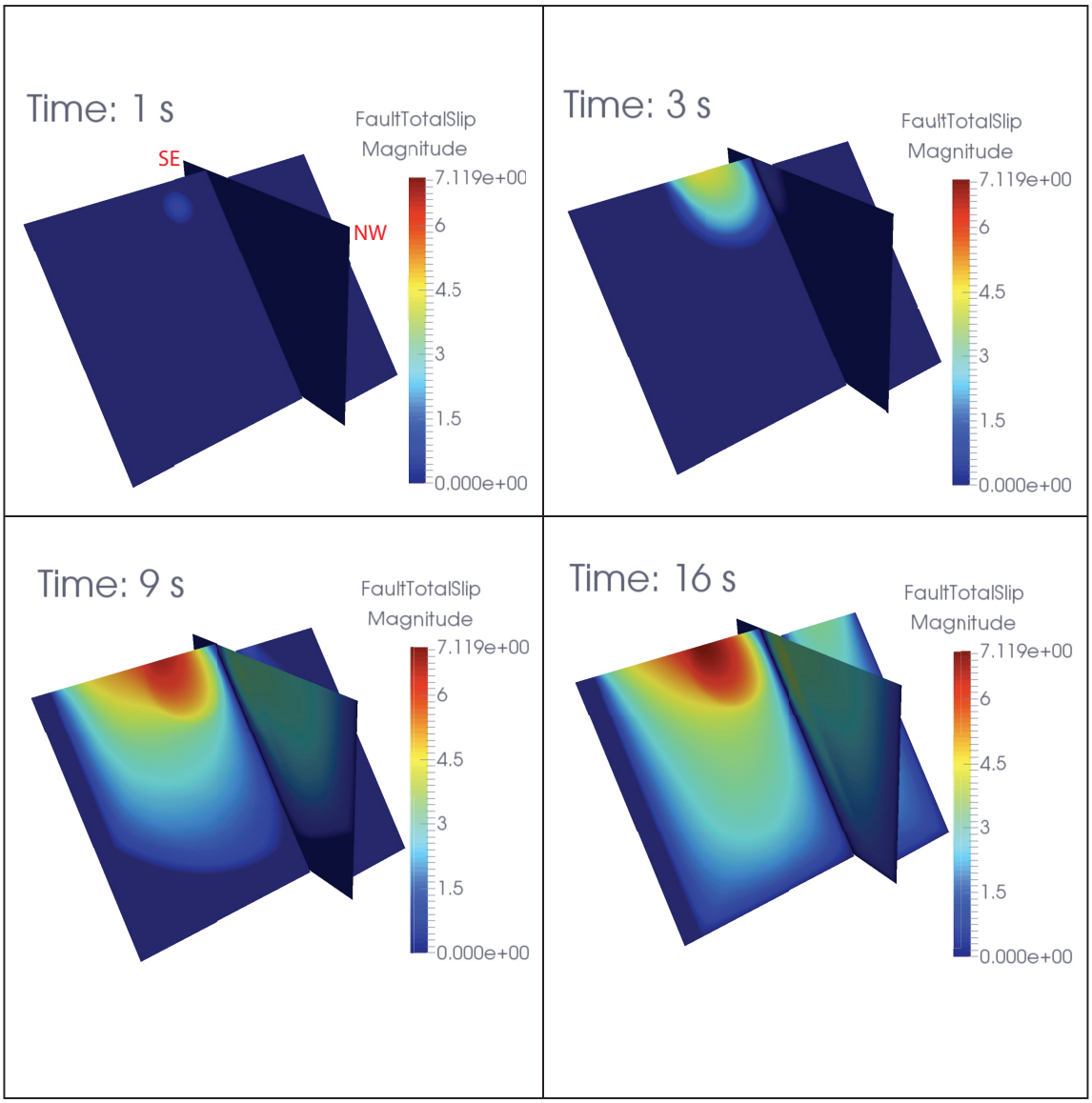

Figure 1.8. Total Slip Plots for T2 55 Degree Dip Model. This model assumes a T2 mesh, 55-degree dipping thrust faults, nucleation on the Eastern Thrust, and the no gap scenario. Fault total slip magnitude is given in meters. At 3 and 9 seconds, the slightly paler blue color shows where the rupture has jumped across to another fault.

The nucleation location and the gap or no gap scenarios cause the most variety in the results. Nucleating on the Strike-Slip Fault with the T2 mesh does not lead to multi-fault rupture, while nucleating on the Eastern Thrust readily causes either two or three faults to rupture. Nucleating on the Western Thrust occasionally leads to a small jump to the Eastern Thrust that bypasses the Strike-Slip Fault, but quickly dies out if the Strike-Slip Fault is longer along-strike (aka the gap scenario). If the no gap scenario is employed in the model with nucleation on the Western Thrust, then with 35-degree dipping thrusts, all three faults fails, but with 45 and 55-degree dipping thrusts, rupture tends to die out on the Strike-Slip Fault. Depending on the nucleation location, the no gap scenario (with a 4 km longer Strike-Slip Fault) leads to a higher likelihood of multi-fault rupture. Overall, there is a complex interaction between the dip angle, nucleation location, and fault intersection scenarios.

1.4.3. Summary and Comparison Between T1 and T2 Models

The most robust result from the models using the T1 and T2 meshes is that rupture nucleation on the Strike-Slip Fault does not lead to multi-fault rupture. Despite increasing the size of the thrusts and decreasing the distance between the thrusts and the Strike-Slip Fault from the kilometer scale down to 100 m on either side, the difference in the fault geometry of the two meshes does not affect the Strike-Slip Fault nucleation scenario (Figure 1.9). Figure 1.9a shows a sample model from the T1 set and Figures 1.9b-c show samples from the T2 set. For the T2 set, we show both the gap scenario

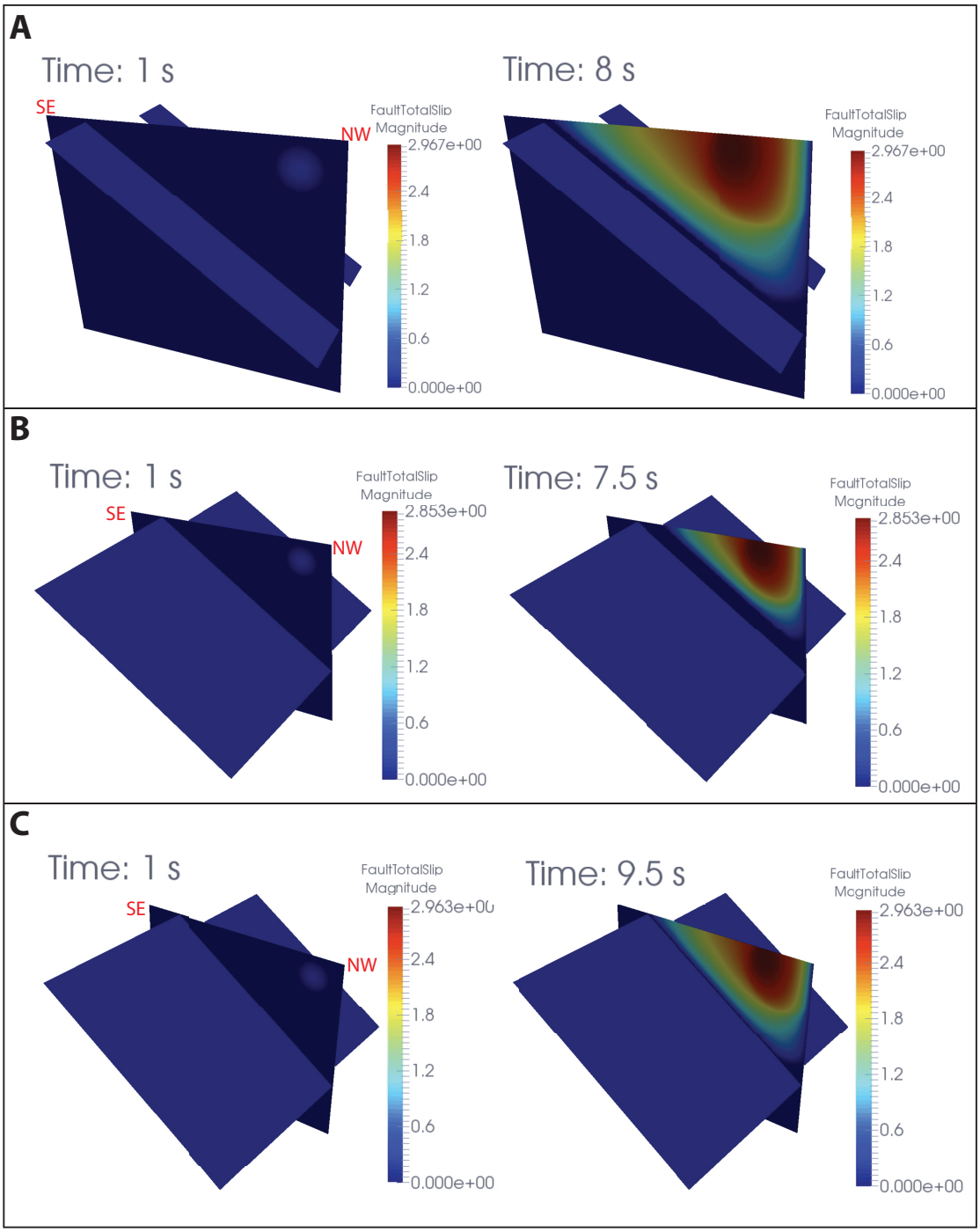

Figure 1.9. Total Slip Plots for Representative Strike-Slip Nucleation Models. These plots show the nucleation and final slip plot. (A) Model with the T1 mesh, 35-degree dipping thrusts, and the no gap scenario. (B) Model with the T2 mesh, 35-degree dipping thrusts, and the gap scenario. (C) Model with the T2 mesh, 35-degree dipping thrusts, and the no gap scenario. Each is representative of a larger suite of models with the same result that the rupture does not propagate from the Strike-Slip Fault to the thrusts.

(Figure 1.9b) and the no gap scenario (1.9c) because the distance between the thrusts and the Strike-Slip Fault is so small, it would be conceivable that rupture could jump in one of these models. However, the distance is insignificant because the stresses are not optimally oriented between the pure strike-slip motion of the Strike-Slip Fault and the pure dip-slip motion of the thrusts to facilitate multi-fault rupture. The easiest path for rupture is to continue along the Strike-Slip Fault. With the decreased distance between the thrusts and the Strike-Slip Fault, if nucleation occurs on either of the thrusts, multi fault rupture is more likely in the T2 models (Figure 1.10). Overall, nucleation on the Eastern Thrust with either of these meshes leads to the largest number of scenarios with multi-fault rupture.

1.4.4. Variable Depth Models

All previous models assume a 3 km nucleation depth, which is fairly shallow. Using the T2 mesh, which is likely to provide more stable results because of the larger along-strike length of the thrusts, we test the following nucleation depths: 8, 13, and 20 km. We could not test nucleation on the Strike-Slip Fault in some scenarios because FaultMod uses a 3-D spherical nucleation zone. Moving the nucleation point downward, close to the angle of the thrusts causes artificial bleed-over of nucleation onto the thrusts, creating artificial patches of slip on the thrusts that die out as soon as the nucleation phase ends. The scenarios that have this problem are listed as "Not Available" in Figure 1.11. At a depth of 20 km, the Western Thrust is too close to the edge of the mesh volume for reliable results (a wider mesh would be needed to test such deep nucleation points,

increasing the overall number of elements and computational time), so we only tested nucleation at that depth on the Eastern Thrust; the results matched exactly with the results for a 13 km depth (Figure 1.11).

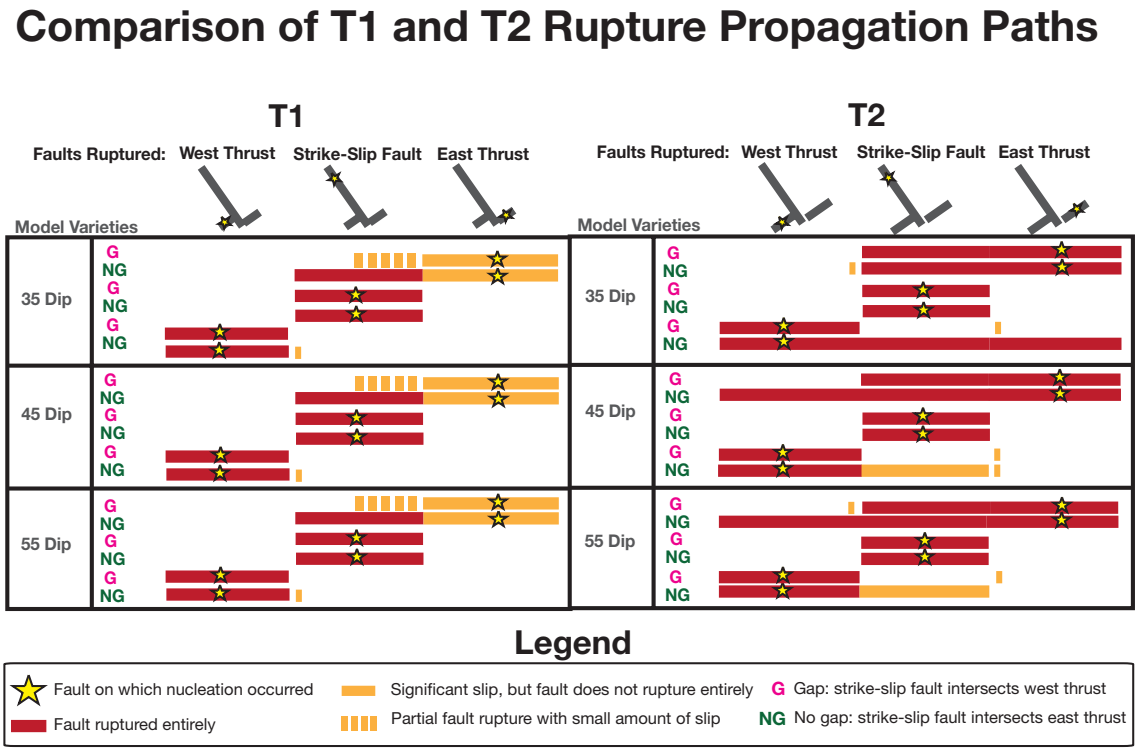

Figure 1.10. Summary Plot of T1 and T2 Results. In general, the trends of the models using the T2 mesh follow those of the T1 mesh. The main difference is that the T2 mesh promotes directivity due to its larger along-strike lengths for the thrust faults, allowing the dynamic stresses ahead of the rupture front to build up and facilitate multi-fault rupture. This legend is used for all subsequent summary plots.

T2 Rupture Propagation Paths with Different Nucleation Depths

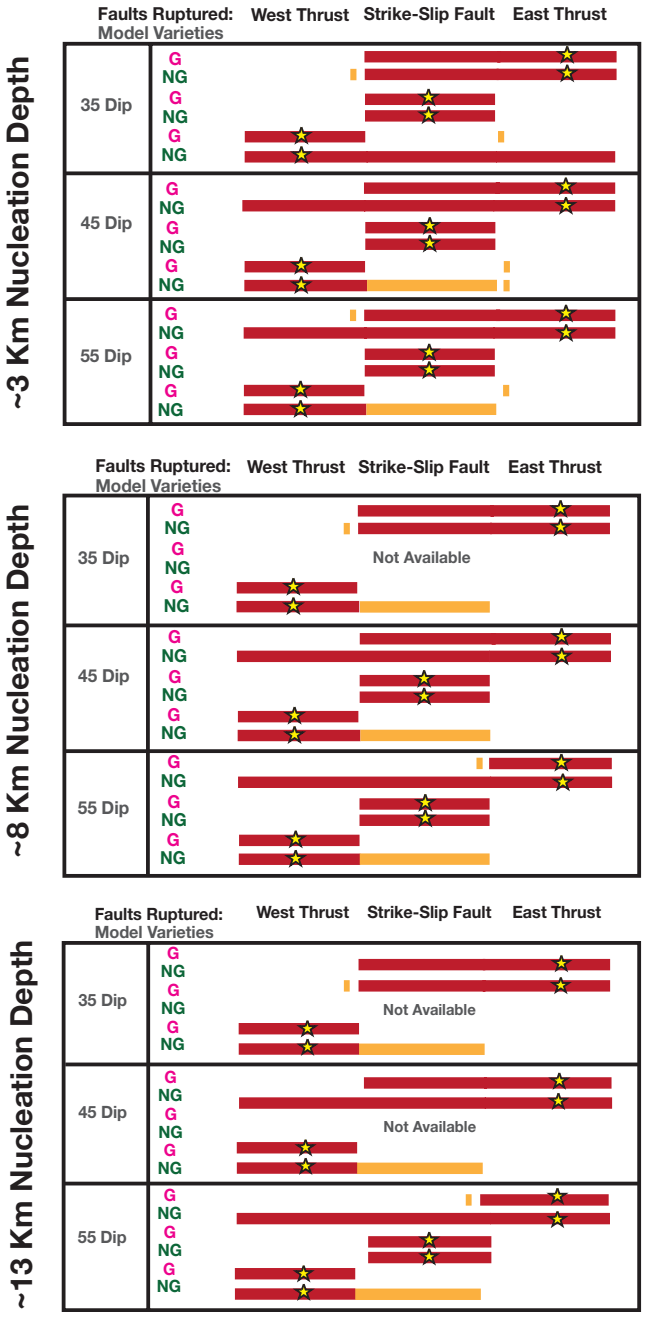

Figure 1.11. Summary Plot of T2 Variable Depth Results. Although there is some variability between the shallow models and the 8 km depth models, the 8 km and 13 km depth results match and the overall trends are still visible. Results marked "Not Available" are due to issues with a spherical nucleation zone. See text for details.

Nucleation deeper than 3 km produces results that are slightly different from the shallow nucleation because the dynamic stress interactions are somewhat modified by different rupture directivity. In addition, with some dip angles of the thrusts, we cannot exactly duplicate each deeper nucleation point. We do our best to approximate the same location by constraining it in the along-strike direction of the faults. We use the same number of elements along the strike of the thrust faults as were used in the first round of shallow models when placing the nucleation point at roughly the same depth (see Figure 1.12). However, this means the absolute along-dip location is different, which we believe causes the bulk of the variation in rupture propagation. This kind of subtle variability in

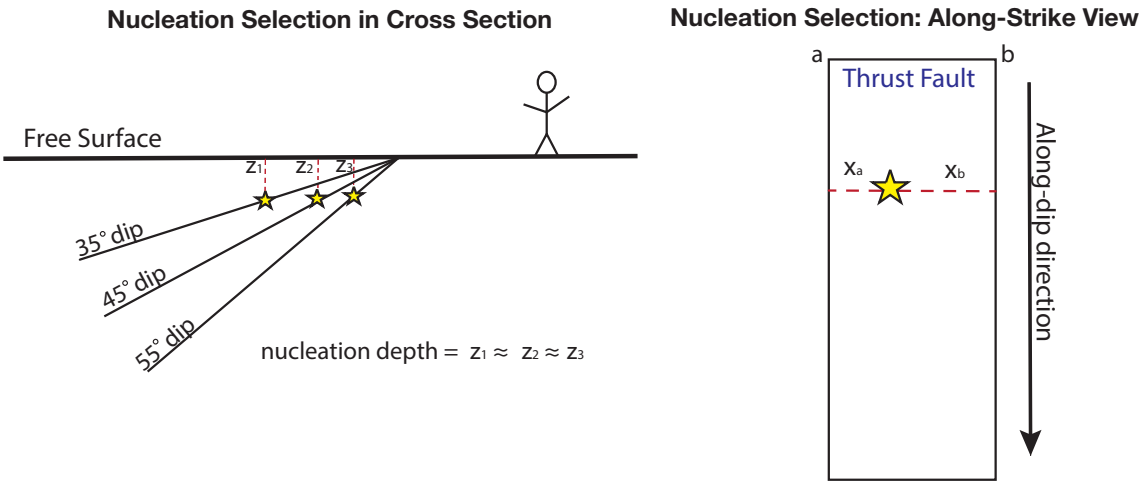

Figure 1.12. Nucleation Point Selection. To select nucleation points (denoted as stars) at various depths with dipping faults, it is only possible to constrain 2 out of 3 dimensions. We constrain the depth and along-strike positions. The depth (z) for groups of models is approximately the same for the 35º, 45º, and 55º dip angle configurations (hence the 3, 8, and 13 km nucleation depth groups of models). The along-strike position is constrained using the same number of elements from edge "a" of the thrust fault (x_a) and the same number of elements from edge "b" of the thrust fault (x_b) for each dip angle (x_a and x_b are not equal). This means that the along-dip position of the nucleation point is different for the models with different dip angles. We chose to used fixed depths on the thrusts because it would provide a more direct comparison with fixed depths on the Strike-Slip Fault.

the stresses with time, based on the nucleation location, is why it is important to test complex situations with dynamic models. Overall, the results of the 8 km depth models closely match the 3 km depth models discussed above, but there are a few differences. At deeper nucleation depths, none of the models with nucleation on the Western Thrust that cause all three faults to fail (Figure 1.11). For nucleation on the Eastern Thrust, the deeper depths do not lead to multi-fault rupture when the thrusts angles are 55 degrees and the gap scenario is employed. Based on the fact that the results for the Eastern Thrust nucleation models at 20 km matched exactly the 13 km results, we suspect that deeper earthquakes nucleating on the other faults would also be similar. In general, the over-arching patterns observed in the shallow models are still present with deeper nucleation depths.

1.4.5 Regional Stress Models

In addition to changing the spatial position of model parameters, we tested a small series of different initial stress conditions. For the four sets of models with different regional stress fields, we assumed the median values of the dip and depth assumptions from our previous models (8 km depth for nucleation and 45 degree dip angle on the thrusts) and the results are summarized in Figure 1.13. As with the constant-traction models, we obtain the robust result that nucleation on the Strike-Slip Fault did not allow rupture to jump in any of the regional stress variations. With the no gap scenario, nucleation on the Eastern Thrust fault leads to multi-fault rupture in all stress fields. For

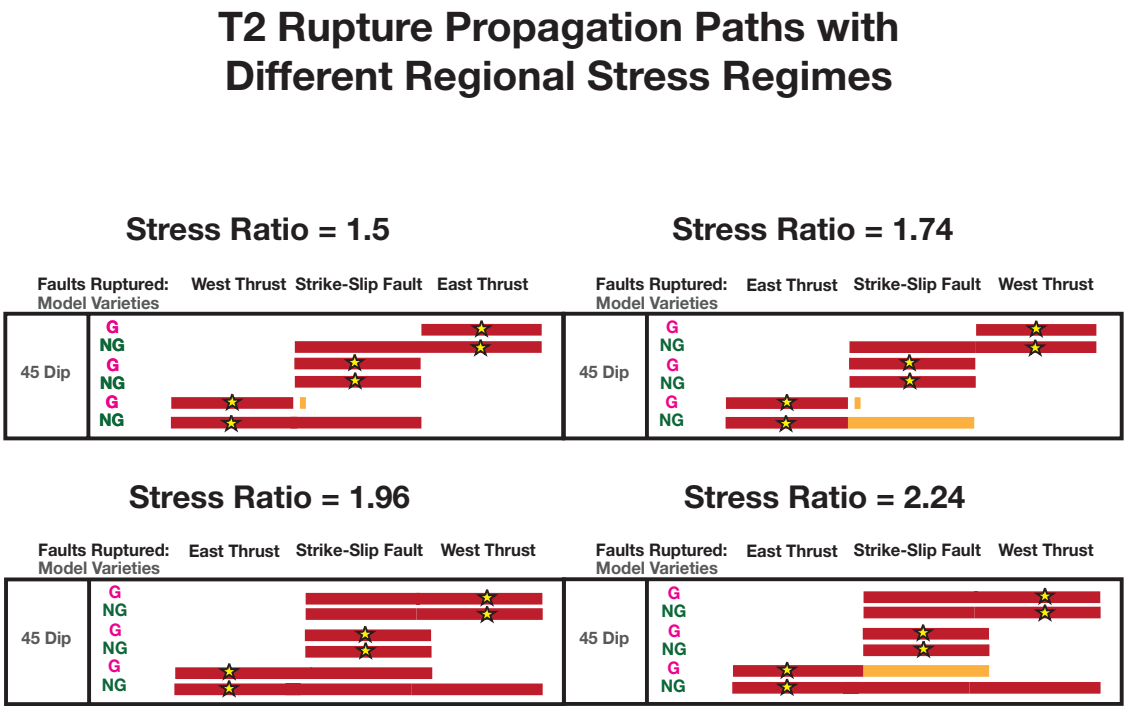

Figure 1.13. Summary Plot of T2 Regional Stress Results. The stress ratio spans the given ratio of the oblique regional stress field at ~10 km depth in *Hardebeck and Hauksson* (2001). The end members of 1.5 and 2.24 indicate a more strike-slip dominated regime versus a more compressive regime, respectively. The various regional stresses lead to more variability in the results. However, the result that nucleation on the Strike-Slip Fault does not lead to multi-fault rupture is in line with the results of all the previous models in this paper.

nucleation on either of the thrusts, multi-fault rupture becomes more favorable if the A_ϕ stress ratio is higher, corresponding to the case that the oblique stress field is dominated more by compression than strike-slip. Thus the conditions that enhance thrust faulting also enhance multi-segment rupture. The results of the intermediate stress fields with ratios of 1.74 and 1.96 most closely resemble the results from the shallow depth models in Figure 1.12.

1.5. Discussion

The results of this study have key similarities to previous studies with complex fault geometries that were not specific to the SGP. Similar to *Harris and Day* (1993), we see that the distance between faults can affect rupture jumps. In the T1 models, while the 4 km distance between the Western Thrust and the Strike-Slip Fault is smaller than the typical 5 km threshold for rupture jumps with step-overs (*Harris and Day*, 1993), the large distance contributes to smaller dynamic shear stress values and inhibits rupture jumps from the Western Thrust to the Strike-Slip Fault. In contrast, the smaller 2 km distance between the Eastern Thrust and Strike-Slip Fault facilitates rupture jumps from the Eastern Thrust to the Strike-Slip Fault, even though the Strike-Slip Fault does not fully rupture. In both the T1 and T2 models, we see that although a 4 km gap on the Strike-Slip Fault decreases the total slip in some models, rupture is still capable of jumping this distance in the models. This suggests that nucleation location and directivity may have a larger role on rupture propagation paths than solely the size of gaps between faults. We see that the results are sensitive to the nucleation location and that slip on the Strike-Slip Fault hinders rupture on the nearby thrusts, consistent with *Oglesby* (2005). However, the similarity with the *Oglesby* (2005) models may partly be due to a similarity in fault geometry. Although our models have an inverted T-shape in map view (with a strike-slip fault between two thrusts faults) and *Oglesby* (2005) has a zig-zag shape (with a dip-slip fault between two strike-slip faults), both studies have a 90º along-strike angle between the strike-slip and thrust faults. Wider angles between faults lessen the effects of stress shadowing, thereby making rupture more likely to propagate

along both a branch and a main fault (*Yamashita and Umeda*, 1994; *Oglesby and Duan*, 2007). Although a 90º angle between the thrusts and the Strike-Slip Fault would be considered wide and should therefore facilitate rupture along all the faults, similar to *Oglesby* (2005) we only see this to be true if earthquakes nucleate on the thrusts. However, if wide angles cause weaker dynamic stress interactions between branches (*Kame et al*., 2003), perhaps this angle is too large when nucleation is on the Strike-Slip Fault, allowing rupture to continue along the easiest (straightest) path, completely bypassing the thrusts. Dipping faults add another level of complexity to the analysis of branching fault systems because there are two sets of angles to consider. In our geometry, there is an along-strike angle between the Strike-Slip Fault and the thrusts, as well as a down-dip angle that could alter stress interactions between the thrusts and the Strike-Slip Fault. The down-dip angle of the thrusts did not appear to affect the T1 models, but slight variations between results of the 35, 45, and 55-degree dipping thrusts in the T2 models suggest that directivity may play a larger role than dip angle. The longer along-strike fault lengths likely provided a larger area over which shear stresses ahead of the rupture front could build up and cause propagation over multiple faults. As fault geometries become more complex, it is difficult to tell which aspects of the geometry have the most control over rupture propagation paths.

Although the models in this work use simplistic fault geometries, it may be possible to extrapolate these results to the SGP region. From the simplified models we see that a through-going rupture scenario in the SGP would be more probable if an earthquake began in the southeastern SGP, along one of the thrust faults, instead of in the

northwestern part of the region. Our models are finite in their spatial size, but this scenario could hypothetically include ruptures that nucleate farther to the east of the SGP, near Bombay Beach. In many of our models, this "rupture from the east" scenario results in rupture propagating out of the SGP along the Strike-Slip Fault (the simplified San Bernardino strand), matching TeraShake results that imply metropolitan areas in the Los Angeles and San Gabriel basins would be greatly affected (*Olsen et al*., 2006; 2008).

Our robust result that nucleation on the Strike-Slip Fault did not lead to multi-fault rupture is also similar to the results from the TeraShake models, which indicate that an earthquake nucleating in the north on the San Bernardino strand does not produce through-going rupture (*Olsen et al*., 2006; 2008), even though models of this study use a substantially different fault geometry than that used in the regional TeraShake model. In this sense, the SGP may be a barrier for rupture if an earthquake initiates northwest of the SGP on the San Bernardino strand. *Carena et al*. (2004) suggest that if the San Gorgonio Pass Fault Zone is close to failure, theoretically an earthquake nucleating on the San Bernardino strand could be able to rupture through the SGP. Although our models do not show this, perhaps our initial stress conditions are too rudimentary. The earth is not likely to have constant tractions, and the assumption of pure right-lateral strike-slip stress on the San Bernardino strand and pure thrust stress on the San Gorgonio Pass Fault Zone may be over-simplified. However, we obtain the same result with the regional stress fields. Perhaps this is also an over-simplification because the number of faults and proximity to other fault zones could have an effect on the stress interactions in this region (*Carena et al*., 2004). It may be necessary to study a broader range of fault geometries

that include more of the nearby mapped faults, in conjunction with more heterogeneous initial stress fields that account for stress release and loading from paleoseismic events.

1.6. Conclusions

Although our fault geometry is more complex than geometries used in previous numerical models of the SGP, it is still a simplification of the structures in the SGP. With this simplified geometry, earthquakes that nucleate on the right-lateral strike-slip San Bernardino strand of the SAF do not propagate to the San Gorgonio Pass Fault Zone in any of our models. Nucleation on a thrust in the San Gorgonio Pass Fault Zone east of the San Bernardino strand often leads to multi-fault rupture, including several through-going scenarios, and nucleation on a thrust in the San Gorgonio Pass Fault Zone west of the San Bernardino strand occasionally leads to multi-fault rupture, including some through-going scenarios. These results are similar to those of the TeraShake models (*Olsen et al.*, 2006; 2008) used to generate maximum magnitude estimates for hazard preparedness in southern California (*Jones et al*., 2008). Earthquakes nucleating within the SGP on the San Gorgonio Pass Fault Zone, thought to be one of the current active structures in the region (*Yule and Sieh*, 2003; *Ramzan*, 2012; *Scharer et al*., 2013), may be capable of a damaging earthquake that affects large parts of metropolitan and suburban southern California. However, the simplifications in these models may be over-simplifications. The geometry of the potential intersection between the San Bernardino strand and the San Gorgonio Pass Fault Zone has a significant effect on the rupture propagation paths, which is greater than the effect of variations on the dip angle of the

thrust faults. The effect of the potential intersection implies that models more faithfully matching the mapped surface traces and incorporating the complexity of additional fault interactions, including relative stress changes caused by paleoseismic and historic events, may differ from the results of this study.

1.7. References

Aagaard, B.T., G. Anderson, and K.W. Hudnut (2004), Dynamic rupture modeling of the transition from thrust to strike-slip motion in the 2002 Denali Fault, Alaska, earthquake, *Bulletin of the Seismological Society of America*, *94*(6B), S190-S201.

Allen, C. R. (1957), San Andreas fault zone in San Gorgonio Pass, Southern California, *Geological Society of America Bulletin*, *68*, 315-350.

Andrews, D. J. (1976), Rupture velocity of plane strain shear cracks, *Journal of Geophysical Research*, *81*(32), 5679-5687.

Aochi, H., E. Fukuyama, and M. Matsu'ura (2000), Selectivity of spontaneous rupture propagation on a branched fault, *Geophysical Research Letters*, *27*(22), 3635-3638.

Barall, M. (2009), A grid-doubling technique for calculating dynamic three-dimensional spontaneous rupture on an earthquake fault, *Geophysical Journal International*, *178*, 845-859.

Bayarsayhan, C., A. Bayasgalan, B. Enhtuvshin, K. W. Hudnut, R. A. Kurushin, P. Molnar, and M. Ölziybat (1996), 1957 Gobi-Altay, Mongolia, earthquake as a prototype for southern California's most devastating earthquake, *Geology*, *24*(7), 579-582.

Carena, S., J. Suppe, and H. Kao (2004), Lack of continuity of the San Andreas fault in Southern California: Three-dimensional fault models and earthquake scenarios, *Journal of Geophysical Research*, *109*, B04313, doi:04310.01029/02003JB002643.

Dair, L., and M. L. Cooke (2009), San Andreas fault geometry through the san Gorgonio Pass, California, *Geology*, *37*(2), 119-122.

Day, S. M. (1982), Three-dimensional simulation of spontaneous rupture: The effect of nonuniform prestress, *Bulletin of the Seismological Society of America*, *72*(6), 1881-1902.

Duan, B., and D.D. Oglesby, 2007, Nonuniform prestress from prior earthquakes and the effect on dynamics of branched fault systems, *Journal of Geophysical Research*, *112*, B05308, doi:10.1029/2006JB004443.

Eberhart-Phillips, D., et al. (2003), The 2002 Denali fault earthquake, Alaska: A large magnitude, slip-partitioned event, *Science*, *300*(5622), 1113-1118.

Fuis, G. S., D. S. Scheirer, V. E. Langenheim, and M. Kohler (2012), A new perspective on the geometry of the San Andreas Fault in Southern California and its relationship to lithospheric structure, *Bulletin of the Seismological Society of America*, *102*(1), 236-251.

Hardebeck, J.L., Hauksson, E., (2001), Stress Orientations Obtained from Earthquake Focal Mechanisms: What Are Appropriate Uncertainty Estimates, *Bulletin of the Seismological Society of America*, 91, 2, pp. 250-262.

Harris, R. A., and S. M. Day (1993), Dynamics of Fault Interaction - Parallel Strike-Slip Faults, *Journal of Geophysical Research*, *98*(B3), 4461-4472.

Ida, Y. (1972), Cohesive force across the tip of a longitudinal-shear crack and Griffith's specific surface energy, *Journal of Geophysical Research*, *77*(20), 3796-3805.

Jones, L. M., et al. (2008), The ShakeOut Scenario, *U.S. Geol. Surv. Open File Rep.*, *2008-1150*.

Kame, N., J. R. Rice, and R. Dmowska (2003), Effects of pre-stress state and rupture velocity on dynamic fault branching, *Journal of Geophysical Research*, *108*(B5), 2265, doi: 2210.1029/2002JB002189.

Kendrick, K. J., J. C. Matti, S. A. Mahan, G. P. Landis, and D. P. Miggins (2011), Depositional constraints on slip along the San Andreas fault within the eastern San Gorgonio Pass region, Southern California, *2011 SCEC Annual Meeting Program*, A-135.

King, G. C. P., R. S. Stein, and J. Lin (1994), Static stress changes and the triggering of earthquakes, *Bulletin of the Seismological Society of America*, *84*(3), 935-953.

Langenheim, V. E., R. C. Jachens, J. C. Matti, E. Hauksson, D. M. Morton, and A. Christensen (2005), Geophysical evidence for wedging in the San Gorgonio Pass structural knot, southern San Andreas fault zone, Southern California, *Geological Society of America Bulletin*, *117*.

Lozos, J. C., D. D. Oglesby, B. Duan, and S. G. Wesnousky (2011), The effects of double fault bends on rupture propagation: a geometrical parameter study, *Bulletin of the Seismological Society of America*, *101*(1), 385-398.

Lozos, J. C., D. D. Oglesby, J. N. Brune, and K. B. Olsen (2012), Small intermediate fault segments can either aid or hinder rupture propagation at stepovers, *Geophysical Research Letters*, *39(*18), DOI: 10.1029/2012GL053005.

Mac Donald, B. J. (2007), *Practical Stress Analysis with Finite Elements*, Glasnevin Publishing: Dublin, Ireland.

Matti, J. C., and D. M. Morton (1993), Paleogegraphic evolution of the San Andreas fault in Southern California: A reconstruction based on a new cross-fault correlation, in *The San Andreas fault system: Displacement, palinspastic reconstruction, and geologic evolution*, edited by R. E. Powell, R. E. I. Weldon and J. C. Matti, pp. 107-159, Geological Society of America.

Matti, J. C., D. M. Morton, and B. F. Cox (1985), Distribution and geologic relations of fault systems in the vicinity of the central Transverse Ranges, southern California, scale 1:250,000, *U.S. Geol. Surv. Open File Rep.*, *85-365*.

Matti, J.C., D.M. Morton, and B.F., Cox (1992), The San Andreas fault system in the vicinity of the central Transverse Ranges Province, southern California, U.S. Geological Survey Open-File Report 92-354, 40, scale 1:250,000.

Michael, A. J., (1990), Energy constraints on kinematic models of oblique faulting: Loma Prieta versus Parkfield-Coalinga, *Geophysical Research Letters*, *17*(9), 1453-1456.

Nicholson, C., E. Hauksson, and A. Plesch (2012), Active fault geometry and crustal deformation along the San Andreas Fault system through San Gorgonio Pass, California: The view in 3D from seismicity, Abstract T22C-03, in *Presented at 2012 Fall Meeting, AGU, San Francisco, CA, 3-7 Dec.*, edited.

Oglesby, D. D. (2005), The dynamics of strike-slip step-overs with linking dip-slip faults, *Bulletin of the Seismological Society of America*, *95*(5), 1604-1622.

Oglesby, D.D., S.M. Day, Y.-G. Li, and J.E. Vidale (2003a), The 1999 Hector Mine earthquake: the dynamics of a branched fault system, *Bulletin of the Seismological Society of America*, *93*(6), 2459-2476.

Oglesby, D.D., S.M. Day, and D.R.H. O'Connell (2003b), The dynamic and static interaction of two thrust faults: a case study with general implications, *Journal of Geophysical Research*, *108* (B10), 2489, doi:10.1029/2002JB002228.

Olsen, K. B., S. M. Day, J. B. Minster, Y. Cui, A. Chourasia, D. Okaya, P. Maechling, and T. Jordan (2008), TeraShake2: Spontaneous rupture simulations of M-w 7.7 earthquakes on the southern San Andreas fault, *Bulletin of the Seismological Society of America*, *98*(3), 1162-1185.

Olsen, K. B., S. M. Day, J. B. Minster, Y. Cui, A. Chourasia, M. Faerman, R. Moore, P. Maechling, and T. Jordan (2006), Strong shaking in Los Angeles expected from southern San Andreas, *Geophysical Research Letters*, *33*, L07305, doi:07310.01029/02005GL025472.

Oglesby, D. D. and P. M. Mai (2012), Fault geometry, rupture dynamics and ground motion from potential earthquakes on the North Anatolian Fault under the Sea of Marmara, *Geophysical Journal International, 188*(3), 1071-1087.

Plesch, A., et al. (2007), Community Fault Model (CFM) for Southern California, *Bulletin of the Seismological Society of America*, *97*(6), 1793-1802.

Ramzan, S. (2012), Paleoseismic investigation of the San Gorgonio Pass fault zone near Cabazon, California, M.S. Thesis: California State University, Northridge.

Scharer, K. M., D. Yule, L. R. Humbert, R. Witkowsky (2013), Implications for San Andreas Fault Ruptures Based on New Evidence from the Cabazon, CA Paleoseismic Site, San Gorgonio Pass Fault Zone, *American Geophysical Union, Fall Meeting 2013*, abstract #T43A-2622.

Sieh, K. E., L. Jones, et al. (1993), Near field investigation of the Landers earthquake sequence, April to July 1992, *Science*, *260*(5105), 171-176.

Sieh, K. E., and P. L. Williams (1990), Behavior of the southernmost San Andreas Fault during the past 300 years, *Journal of Geophysical Research, Solid Earth, 95*(B5), 6629-6645.

Stern, A. R. (2016), Fault interaction within restraining bend fault systems, M.S. Thesis: University of Massachusetts, Amherst.

Sykes, L. R., and L. Seeber (1985), Great earthquakes and great asperities, San Andreas fault, Cajon Pass, Southern California, *Geological Society of America Bulletin*, *13*, 835-838.

Taylor, J. R. (2005), *Classical Mechanics*, University Science Books: USA.

Templeton, E. L., H. S. Bhat, R. Dmowska, and J. R. Rice (2009), Dynamic rupture through a branched fault configuration at Yucca Mountain and resulting ground motions, *Bulletin of the Seismological Society of America, 100*(4), 1485-1497.

Wesnousky, S. G. and C. H. Jones (1994), Oblique slip, slip partitioning, spatial and temporal changes in the regional stress field, and the relative strength of active faults in the Basin and Range, western United States, *Geology*, *22*, 1031-1034.

Yule, D. (2009), The enigmatic San Gorgonio Pass, *Geology*, *37*(2), 191-192.

Yule, D., and K. E. Sieh (2003), Complexities of the San Andreas fault near San Gorgonio Pass: Implications for large earthquakes, *Journal of Geophysical Research*, *108*(B11), doi:10.1029/2001JB000451.

Zhang, H., Y. Z. Zhou, Z. L. Wu, Z. Z. Yan, S. Chen, H. M. Jing, X. W. Xu, Y. L. Shi (2009), Finite element analysis of seismic wave propagation in Fuzhou Basin, *Chinese Journal of Geophysics*, *52*(3), 604-614.

1.8. Tables

Table 1.1. Unique Mesh Varieties

Mesh Type	Dip Angle of Thrusts	Intersection Type
T1	35	Gap
T1	35	No Gap
T1	45	Gap
T1	45	No Gap
T1	55	Gap
T1	55	No Gap
T2	35	Gap
T2	35	No Gap
T2	45	Gap
T2	45	No Gap
T2	55	Gap
T2	55	No Gap

Table 1.2. Constant Traction Models: Physical and Computational Parameters

P-wave Velocity	S-wave Velocity	Density
5477 m/s	3162 m/s	2700 kg/m^3
Static Friction	**Dynamic Friction**	**Slip Weakening Distance**
0.84	0.42	0.4 m
Initial Shear Stress	**Initial Normal Stress**	**Nucleation Stress**
10 MPa	16.65 MPa	15.4 MPa
Small Element Size	**Large Element Size**	**Nucleation Radius**
200 m	600 m	5 km

Table 1.3. Regional Stress Models: Physical and Computational Parameters

P-wave Velocity	**S-wave Velocity**	**Density**
5477 m/s	3162 m/s	2700 kg/m^3
Static Friction	**Dynamic Friction Slip**	**Weakening Distance**
0.6	0.1	0.4 m
Small/Large Element Size	**Nucleation Radius**	**Nucleation Stress**
200/600 m	5 km	10% > Initial Stress

Stress Tensor Variation	σ_{00}	σ_{01}	σ_{02}	σ_{10}	σ_{11}	σ_{12}	σ_{20}	σ_{21}	σ_{22} **(MPa)**
$A_\phi = 1.5$	53	0	0	0	31	-11	0	-11	31
$A_\phi = 1.74$	53	0	0	0	29.5	-9.5	0	-9.5	29.5
$A_\phi = 1.96$	70	0	0	0	35	-12	0	-12	35
$A_\phi = 2.24$	69	0	0	0	32.5	-10.5	0	-10.5	32.5

Chapter 2

The effects of pre-stress assumptions on dynamic rupture with complex fault geometry in the San Gorgonio Pass, CA region

2.1. Abstract

We use 3D dynamic finite element models to investigate potential rupture paths of earthquakes propagating along faults in the western San Gorgonio Pass (SGP) region. The SGP is a structurally complex region along the San Andreas fault system (SAF) in southern California. We focus on the San Bernardino strand of the SAF, the San Gorgonio Pass Fault Zone, and a portion of the Garnet Hill strand of the SAF. The San Bernardino and Garnet Hill strands are predominately right-lateral strike-slip faults. Thrust faults dominate the San Gorgonio Pass Fault Zone, with small right-lateral tear faults between the thrust faults. We use the finite element method code FaultMod (*Barall*, 2009) to observe differences in rupture propagation along a meshed fault geometry that reflects most of the surface trace complexity, and is consistent with long-term loading and observed surface deformation. We test three different types of pre-stress assumptions: 1) constant tractions, 2) regional stress regimes, and 3) long-term (evolved) stress from quasi-static crustal deformation modeling. Models with constant tractions assume pure right-lateral strike-slip motion on the San Bernardino and Garnet Hill strands and oblique thrust/right-lateral strike-slip motion on the San Gorgonio Pass Fault Zone. We find that the complexity of the fault geometry inhibits rupture propagation for several nucleation location and stress field assumptions, which may have implications for the reduced likelihood of through-going earthquakes scenarios along the SAF in southern California.

2.2. Introduction

The San Gorgonio Pass (SGP) is located between the San Bernardino and San Jacinto mountains in southern California. In this region, the San Andreas Fault system (SAF) does not appear to have obviously continuous faults based on mapped surface traces (Figure 2.1). Faults appear discontinuous, and many of the relationships among the various mapped traces are unclear (*Allen*, 1957; *Matti et al*., 1985; *Matti and Morton*, 1993; *Yule and Sieh*, 2003). This is an important region in southern California seismology because of the uncertainty about its ability to produce large, through-going earthquakes. The entirety of the southern SAF, especially through the SGP, has not

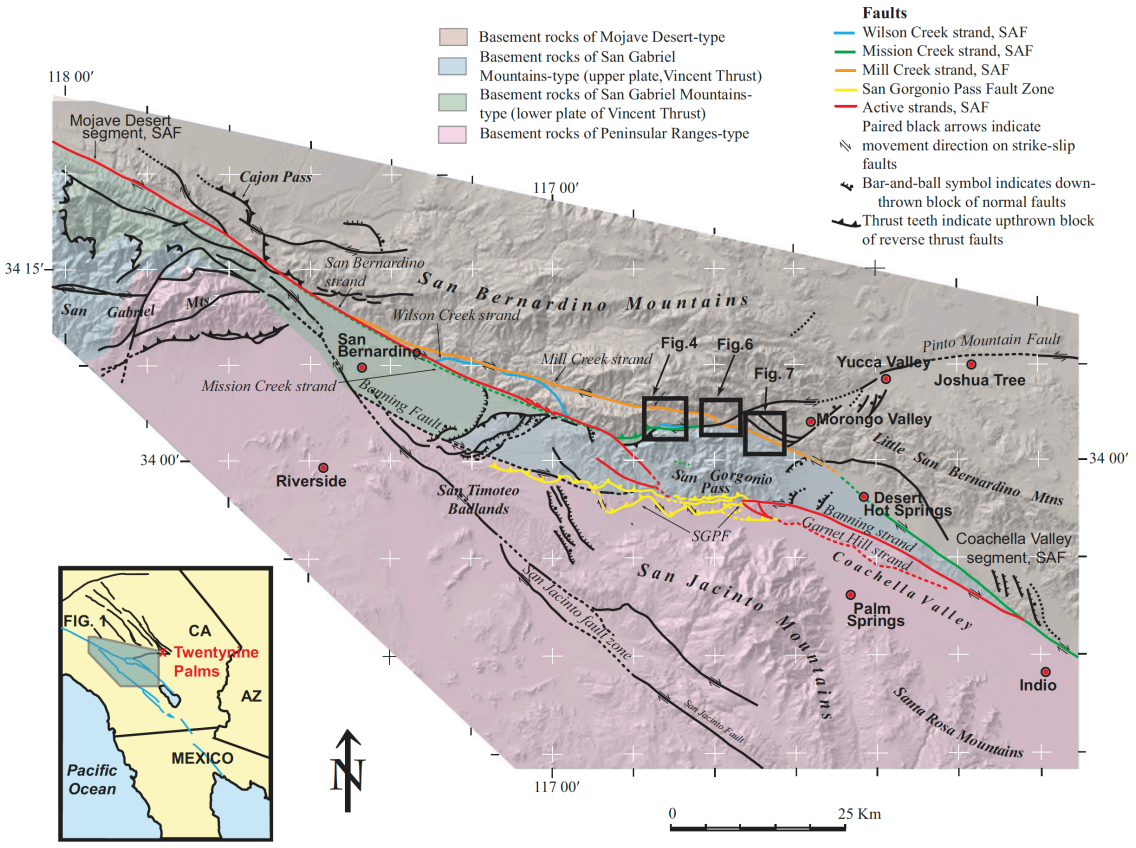

Figure 2.1. Location and Fault Map. All annotations are original to the figure, from *Kendrick et al*. (2015). Original mapping from *Matti et al*., (1982) and *Matti and Morton*, (1993).

ruptured in modern, seismically recordable history, but if it were to fail in a single, through-going rupture, large parts of southern California could experience strong shaking (*Olsen et al*., 2006; 2008).

2.1.1. Brief Geologic Considerations

The SGP has a complex history of right-lateral strike-slip faulting, fault strand-switching, and convergence. The Mill Creek strand of the SAF is the most prominent through-going feature in the region, but it is deemed currently inactive (*Matti et al*., 1992; *Kendrick et al*., 2015). Many researchers have hypothesized that following the shut-off of the Mill Creek strand, the complexity of fault interactions in the SGP increased as less mechanically optimal paths to transfer slip developed (*Matti et al*., 1992; *Yule and Sieh* (2003); *Yule* (2009); *Kendrick et al*. (2015). However, the Mill Creek strand is often still incorporated into regional fault geometries such as the Southern California Earthquake Center (SCEC) Community Fault Model (*Plesch et al*., 2007). Modelers tend to favor simple structures in studies of hypothetical earthquake scenarios, and consequently several studies use simplified geometries that actually represent older, inactive structures in the SGP (*Meade and Hager*, 2005; *Smith and Sandwell*, 2006; *Olsen et al*., 2006; *Olsen et al*., 2008). *Dair and Cooke* (2009) tested various fault geometries through the SGP with static deformation models to see which geometries matched well with slip rate and uplift studies. Using the Mill Creek strand did not produce a good match with the slip rate and uplift data (*Cooke and Dair*, 2011). Geologic mapping and paleoseismic studies indicate that thrust faults south of the San Bernardino Mountains (Figure 2.1) are

likely some of the currently active structures (*Allen*, 1957; *Matti et al*., 1985; *Yule and Sieh*, 2003; *Kendrick et al.,* 2011; *Ramzan*, 2012, *Scharer et al*., 2013). Three-dimensional crustal deformation models that incorporate some finer-scale geometric complexities of active faults in the SGP (*Cooke and Dair*, 2011; *Herbert and Cooke*, 2012) match slip rates and uplift patterns fairly well. Consequently, we incorporate the San Bernardino strand of the SAF, the San Gorgonio Pass Fault Zone and a portion of the Garnet Hill strand of the SAF into our semi-regional fault geometry. Because the full fault names are bulky, we drop "of the SAF" for the San Bernardino strand and Garnet Hill strand in the remainder of this paper.

2.2.2. Advancement of Complexity in Rupture Models

Rupture models are rapidly incorporating increasing levels of complexity. Early, models that captured the physics of the earthquake problem were geologically unrealistic. Before realistic fault geometries, stress regimes, and heterogeneities in 3D earth materials could be adequately addressed, dynamic models first had to be able to represent stress heterogeneity (*Day*, 1982), frictional properties (*Dieterich*, 1978; 1979; *Ruina*, 1983; *Ohnaka and Kuwahara*, 1990; *Ohnaka*, 1996), wave interactions (*Madariaga et al*., 1998), and healing or rupture termination (*Day*, 1982; *Heaton*, 1990; *Madariaga et al*., 1998). Many models used a two-dimensional fault geometry, a 2D pre-stress field, or a combination of both (e.g. *Bhat et al*., 2004; *Fliss et al*., 2005). Early studies that included analysis in three-dimensions typically used a planar, horizontal fault in a fully elastic, homogeneous medium in order to test the physics and work within the limitations of their

models (e.g. *Madariaga et al*., 1998). Models using planar faults are simpler to work with mathematically, but for geologists wishing to use such models to test hypotheses about fault interactions or simulate potential earthquake rupture paths, models with complex faults that more accurately represent existing fault systems are necessary.

More complex models include fault branches and test the effects of assigning more complex stress fields versus homogeneous stress. The initial stress conditions that are input into dynamic models are referred to as the pre-stress model or pre-stress field. Although *Aochi et al*. (2000) introduced 3D fault geometries into branched fault modeling, the pre-stress field was essentially a 2D model extruded into 3D. This kind of pre-stress is non-oblique, and probably unrealistic for large-scale active fault systems that experience changes in stress after each earthquake on various fault strands. In an oblique stress field, shear stress will be resolved differently on faults with different orientations, leading to certain rupture propagation paths being more favorable than others. *Oglesby et al*. (2003a) showed that despite using an originally homogeneous stress field, the model of the 1999 Hector Mine earthquake on a branched fault system produced a final heterogeneous stress field.

Although simplifications are often necessary when modeling earthquakes, over-simplifications can miss important aspects of complex fault systems and provide inaccurate estimates of ground motion or propagation paths. Studies that use more realistically complex geometries and stresses have shown the following effects. The distance between faults affects how quickly a rupture can propagate from one fault to another, and distances greater than 5 km are not easily jumped (*Harris and Day*, 1993).

The branching angle between faults in a branched fault system can promote propagation onto patches of adjoining faults that become critically stressed, while creating stress shadows along different patches (*Kame et al*., 2003; *Duan and Oglesby*, 2007). Stress interactions between faults during rupture can either facilitate or terminate further rupture and are highly dependent on fault geometry and pre-stress conditions (*Oglesby et al*., 2003a; 2003b). Likewise, modeling intersecting faults with differing mechanisms (i.e. strike-slip and thrust) produces propagation paths that are a complex result of the pre-stress field, the dynamic stress field, and the initial earthquake nucleation location (*Oglesby*, 2005; *Chapter 1 of this dissertation*). Small faults located between larger faults can sometimes hinder or facilitate rupture propagation due to differences in dynamic stress interactions that are sensitive to the length, depth, and orientation of the smaller fault (*Lozos et al.*, 2012). The addition of topography to models with complex fault geometries results in zones with either an increase or decrease in total displacement along the fault when compared to a comparable model without topography (*Kyriakopoulos* et al., 2015). Using evolved stresses from the earthquake simulator RSQSim as the inputs for dynamic rupture models, *Gilchrist* (2015) finds that the ground motions calculated are significantly lower than those calculated in models with more typical homogeneous initial stress states. Given the complex interactions between stresses and fault geometry, it is valuable to apply a variety of stress assumptions to a more realistically complex fault geometry through the SGP to better characterize the plausible rupture scenarios in this region.

2.3. Methods

We use the 3D dynamic rupture finite element method code FaultMod (*Barall*, 2009). FaultMod takes the following as basic inputs: 3D mesh (i.e., discretized fault and material structure), friction law, stresses, nucleation location (hypocenter), material properties, model duration, and time stepping. Using these inputs, FaultMod solves for displacement at the nodes of the elements, stresses in the elements, and tractions at the fault element faces. In general, the calculations rely on Newton's second law of motion and Hooke's law, which provides the relationship between strain and stress (*Taylor*, 2005; *Mac Donald*, 2007; *Zhang et al*., 2009). The outputs are absolute normal and shear stresses, slip, slip rate, and acceleration. The code has been validated through the Southern California Earthquake Center Code Validation Project (*Harris et al*., 2009).

Dynamic rupture models fully consider the time-varying interaction between motion, forces, and material properties. Dynamic modeling is the approach best-suited to answer the questions of whether it is possible for rupture to propagate through the SGP because results are integrated over time, with the result from one time step affecting the result in the next time step. This allows us to explore the effects of fault geometry and various stress fields on slip distribution and propagation paths over time (*Aochi et al*., 2000; *Aagaard et al*., 2004; *Oglesby et al*., 2003a; 2003b; *Oglesby*, 2005; *Duan and Oglesby*, 2007; *Templeton*, 2009; *Lozos et al*., 2011; *Lozos et al*., 2012).

2.3.1. Mesh Generation

Working with collaborators at the University of Massachusetts, Amherst, we obtain the fault geometry used in *Herbert and Cooke* (2012), *Herbert et al*. (2014), and *Fattaruso et al.* (2014) to successfully match geologic slip rates and patterns of GPS velocities and uplift. This fault geometry is based on the Southern California Earthquake Center Community Fault model version 4 (*Plesch*, 2007) with small refinements introduced by Herbert and *Cooke* (2012), *Herbert et al*. (2014), and *Fattaruso et al*. (2014). We convert and slightly smooth the mesh from Herbert and Cooke (2012) and create the model geometry in the csimsoft software toolkit Trelis, which is based on the CUBIT software from Sandia National Laboratories. We mesh the fault surfaces with 300 m triangular elements and the volumes with tetrahedra. Bias is implemented so that elements far from the faults are three times larger than elements around the faults in order to keep the total number of elements small enough to be compatible with FaultMod's current capabilities. The mesh fault geometry is shown in Figure 2.2. While the mesh

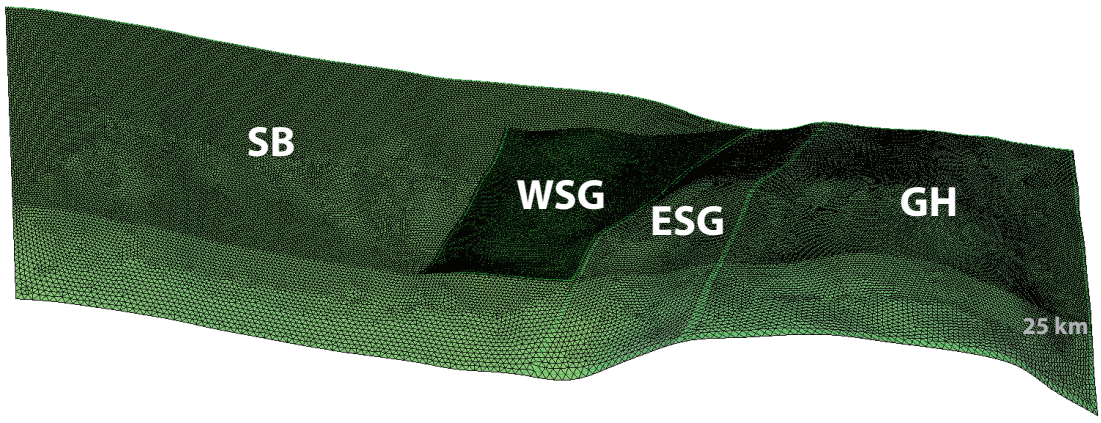

Figure 2.2. Mesh Specifications. The faults are oriented northwest to southeast. The surface trace length of the SB, ESG, and GH combined is 123.3 km and the length of the WSG is 17.1 km. The rupturable depth of the mesh is set to 25 km, as marked on the mesh.

extends down to 35 km, we only allow the upper 20 km to be rupturable. We handle the junction line of the San Bernardino strand and the portions of the San Gorgonio Pass Fault Zone by removing a single line of nodes along that intersection. For simplicity, when referring to the models, we break the fault geometry down into four sections: the San Bernardino strand (SB), the western portion of the San Gorgonio Pass Fault Zone (WSG), the eastern portion of the San Gorgonio Pass Fault Zone (ESG), and the Garnet Hill strand (GH). Breaking the fault geometry into these sections has no geologic significance; it is simply for referential ease when describing setup or results of the models.

2.3.2. Parametric and Stress Field Assumptions

The two main variations we are investigating in these models are the effects of the different stress field assumptions and different nucleation locations. For all models we use the slip weakening friction law (*Ida*, 1972) to isolate the effects of the stress assumptions without adding frictional complexity. The results of the models are divided into three main categories based on their initial stress inputs: Constant Tractions, Regional Stress, and Evolved Stress. In the Constant Tractions models, the SB and GH are loaded in a purely strike-slip manner and the WSG and ESG fault portions, which are located between the SB and GH strands are oblique, partitioned equally between right-lateral strike-slip and thrust behavior. There is precedence for abrupt changes in the orientation of the pre-stress field (*Duan*, 2010) and we employ the simplest assumptions with the Constant Tractions models for comparison with the more complex pre-stress

assumptions. The tractions are considered constant because the initial shear along-strike traction value is the same for every element along the SB and GH, as is the initial normal traction value. Likewise, the WSG and ESG have the same initial shear along-strike and along-dip traction values. With constant frictional parameters, we back-calculate the magnitude of the initial constant shear and normal tractions assuming a 3 MPa stress drop. Physical and computational parameters for the Constant Tractions models are listed in more detail in Table 2.1.

We use the orientation of the tectonic stress regime and the relative magnitude of the three principal stress axes (A_ϕ) of the SGP from *Hardebeck and Hauksson* (2001) as the inputs for the Regional Stress models. We use the A_ϕ parameter as defined in *Simpson* (1997) to calculate ratios of initial stress end members for the range of $A_\phi = 1.5 – 2.3$, as determined for depths of 10 km within the SGP (*Hardebeck and Hauksson*, 2001). The lower end member of 1.5 represents a stronger strike-slip component because $A_\phi \approx 1$ indicates pure strike-slip. The upper member is 2.24, which has a higher compressive component because $A_\phi \approx 3$ indicates pure compression. We resolve two regional stress tensors for the end members onto the fault planes in FaultMod. Physical and computational parameters for the Regional Stress models are listed in Table 2.2. The difference in the frictional parameters between the Constant Tractions and Regional

Stress models is due to the need to maintain strength ratios (or S values) that can facilitate rupture with the specified Constant Tractions. *Das and Aki* (1977) define the dimensionless quantity S as,

$$S = \frac{\tau_u - \tau_0}{\tau_0 - \tau_f} \quad (2.1)$$

where τ_u is the yield stress, τ_0 is the initial shear stress, and τ_f is the final stress. High S values indicate that a fault is far from failure and low values indicate a fault is favorable for rupture.

The models with Evolved Stresses use the stress outputs of quasi-static crustal deformation modeling from *Stern and Cooke* (2014) and *Stern* (2016), based on the method used in *Herbert and Cooke* (2012). In quasi-static crustal deformation modeling, long-term stressing rates are evaluated from plate boundary velocities applied to the model in a two-step approach (e.g. *Marshall et al*., 2009). The first step finds the distribution of long-term steady-state fault slip compatible with applied plate velocities. The second model applies the steady-state fault slip below the locking depth to simulate interseismic loading. Likely shear traction distributions on the various faults are determined from the interseismic stressing rates using recurrence intervals and the time since the last earthquakes, as established in the literature. This method creates a set of pre-stress conditions that should be a more realistic estimation of the pre-stress conditions along the faults in the SGP region than either constant tractions or a regional stress field (Figure 2.3). *Stern* (2016) demonstrates that the shear traction results implementing recurrence intervals, fault interactions, and time since the last event differ from regional stresses resolved onto the same fault geometry. *Stern and Cooke* (2014) show that

absolute shear traction should be increased in the fault bends of the SGP, relative to the strands of the SAF outside the SGP. In addition to the stress interactions of active faults within the SGP, *Stern* (2016) includes the effect of the 1992 Landers earthquake, which reduces shear traction along the Garnet Hill strand and increases shear traction along the San Gorgonio Pass Fault Zone. Due to the size difference between the elements used by our collaborators and our much smaller 300 m element sizes for the dynamic rupture models, we interpolate our stress values twice using a nearest neighbor approximation. The first interpolation is to eliminate NaN values in the shear tractions provided by *Stern* (2016), and the second round interpolates the values to our mesh designed in Trelis.

While we use the shear stress output from *Stern* (2016) and *Stern and Cooke* (2014), we do not use the normal stress output because it is established as a stressing rate. Obtaining the normal traction values from stressing rate would require assuming an arbitrary time increment and there are concerns about artificially high normal tractions due to how the deformation models are loaded (*Cooke*, *pers. comm*., 2016). Instead, we assume a constant S value, or fault strength, along the entire fault geometry. The initial shear stress in Equation 2.1 is calculated from the values provided by *Stern* (2016). From the following relationships substituted into Equation 2.1, we can back-calculate σ_n, the normal stress:

$$\tau_u = \mu_s \sigma_n \tag{2.2}$$

$$\tau_f = \mu_d \sigma_n. \tag{2.3}$$

The values for the static μ_s and dynamic μ_d frictional parameters can be found in Table 2.3. The result is a distribution of normal stress that varies across the fault geometry.

Although S is held constant to obtain the initial normal traction distribution, the dynamic stress interactions during the rupture simulation enable fault strength to vary over the rupture duration.

2.4. Results

In general, we find that the complex fault geometry makes the models more sensitive to the input parameters than the more simplified models in Chapter 1. Similar to *Gilchrist* (2015), our models have difficulty producing large ruptures, and in some cases are unable to rupture beyond the initial nucleation patch. The models show significant differences between constant tractions and regional stress loading, most likely due to compatibility issues with the orientation of the pre-stress field with the complex fault geometry. The Evolved Stresses models are strongly controlled by the initial stress conditions, exhibited in the extreme variability in results from different nucleation locations.

2.4.1. Constant Tractions Models

We further subdivide the Constant Tractions models into two groups: one that employs a linear gradient of normal stress down to 3 km, to simulate the decrease in absolute stress with lower lithostatic load near the surface, and one without a gradient in the normal stress. We find no significant difference in the results between these two groups. We test four nucleation locations with these models, and each produce

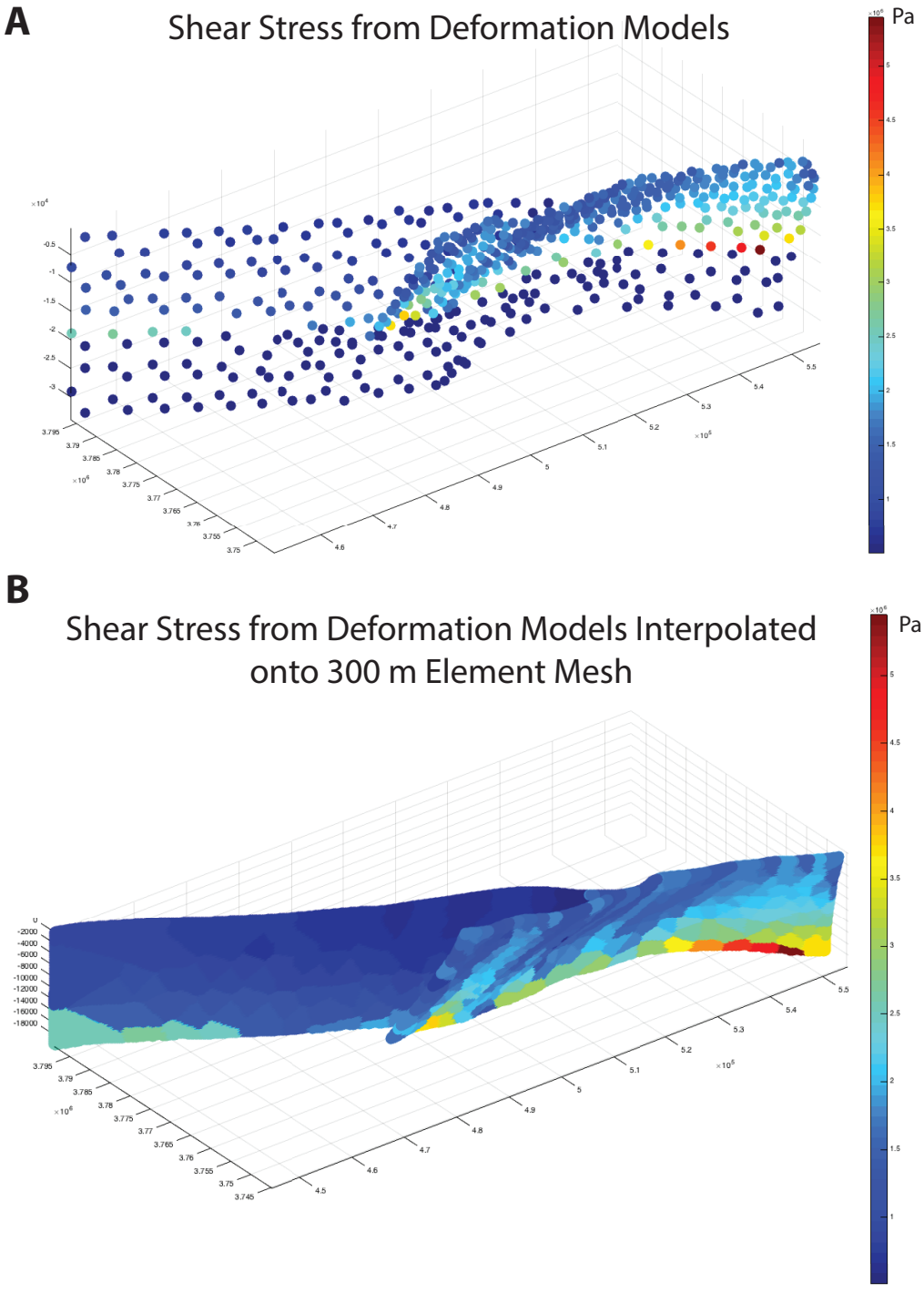

Figure 2.3. Plot of Initial Shear Tractions. (A) Net shear tractions from the deformation models, down to 35 km. This plot shows the coarseness of the initial shear traction distribution. (B) Interpolated shear traction down to the rupturable depth of 20 km. Darker blue colors indicate lower stress and red colors indicate relatively higher stress.

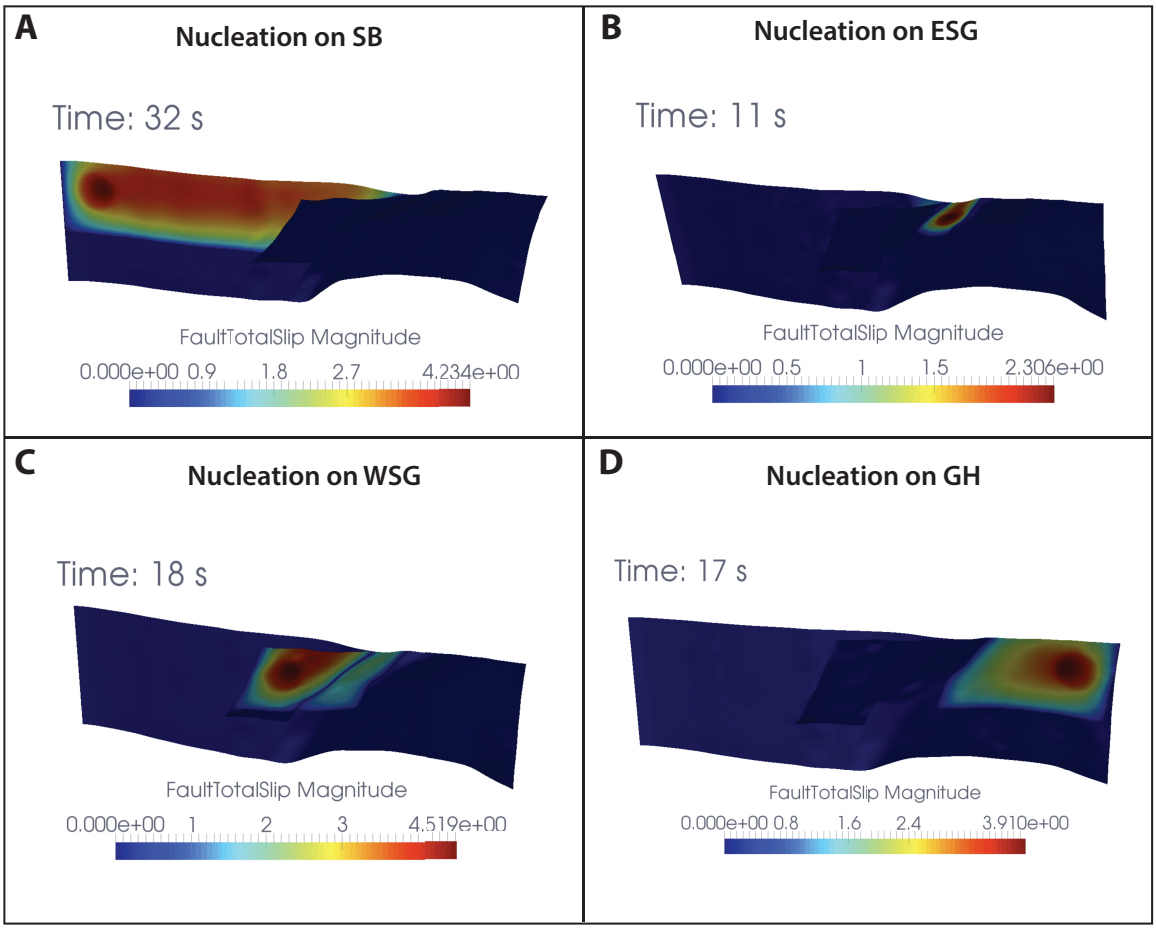

Figure 2.4. Summary Plot of Constant Tractions Models. These show the total slip plots at the end of the simulation for four different nucleation locations. (A) Nucleation on SB. (B) Nucleation on ESG. (C) Nucleation on WSG. (D) Nucleation on GH. Total slip magnitude is given in meters. These models do not result in any through-going rupture scenarios.

significantly different rupture patterns (Figure 2.5). Nucleation on the SB results in an earthquake that only ruptures the SB strand (Figure 2.5a). With nucleation on the ESG, rupture dies out quickly, after rupturing small amounts of the SB and GH (Figure 2.5b), which are more clearly visible when the color scale is over-saturated because the value is roughly 0.6 m of slip. The entirety of the ESG does not slip. Nucleation on the WSG leads to rupture propagation across to the ESG (Figure 2.5c), which is unsurprising

because although these two portions are separated by a line of nodes removed along the intersection with the SB, these two portions have the same initial stress field orientation. With nucleation on the GH, rupture terminates on that fault and does not propagate through to the oblique ESG portion.

2.4.2. Regional Stress Models

We test two end members of the relative magnitude of the three principal stress axes, $A_\phi = 1.5$ and $A_\phi = 2.24$, with the same nucleation locations employed in the Constant Tractions models. Unlike in the Constant Tractions models, we do not delete from the fault system the line of nodes separating the ESG and the GH for these and the Evolved Stresses models. We keep the nodes in these models because there is not an abrupt change in the stress field at this location, unlike in the Constant Tractions models. For the both the Regional and Evolved Stresses, we only test three nucleation locations—on the SB, WSG, and GH, because the ESG and GH are connected as part of the same fault mesh in these models.

The $A_\phi = 1.5$ resolved regional stress field is more favorable for rupture than the Constant Tractions stress field. In the $A_\phi = 1.5$ set of models, nucleation on the GH leads to a through-going rupture scenario (Figure 2.6). By 12 seconds, the rupture has crossed over to both the WSG and the SB (Figure 2.6b). At 25.5 seconds there is a semi-circular patch of the SB that experiences stress shadowing due to rupture on the WSG (Figure 2.6c). Slip on the WSG dynamically decreases the shear stress on the nearly parallel SB, creating this stress shadow. The rupture continues until nearly the entire SB slips,

leaving only a fraction of the previous area within the stress shadow un-ruptured (Figure 2.6d). The magnitude of the total slip is smallest along the SB within the stress shadow created by the WSG. All of the results for the Regional Stress models are summarized in Figure 2.7. The entire fault system ruptures when earthquakes are initiated on either the GH or the SB. With nucleation on the WSG, rupture dies out after the nucleation phase, indicating that this particular stress field does not facilitate rupture on the WSG. Results from the $A_\phi = 2.24$ stress field closely resemble those of the $A_\phi = 1.5$ stress field (Figure 2.7). The most notable difference between the $A_\phi = 1.5$ and $A_\phi = 2.24$ models is that in the latter, the stress shadowing effect between the SB and WSG portions of the fault system is slightly more pronounced, with a smaller total slip magnitude along the SB in response to slip on the WSG. This difference makes intuitive sense because in a more compressive stress regime, slip along the predominately strike-slip SB is less favorable and the oblique dynamic stresses along the WSG help to further decrease shear stress on portions of the SB.

2.4.3. Evolved Stresses Models

This set of models did not have straightforward results (Figure 2.8). Ruptures set to nucleate on the SB and WSG faults did not propagate outside of the initial nucleation zone, and the rupture that nucleated on the GH only propagated through part of the ESG. We attempted lowering the S value from 1.0 to 0.5, thereby lowering the variable normal traction, but the results did not qualitatively change. Given the relatively small shear stress magnitudes and variable distribution of the stresses, we used the critical patch

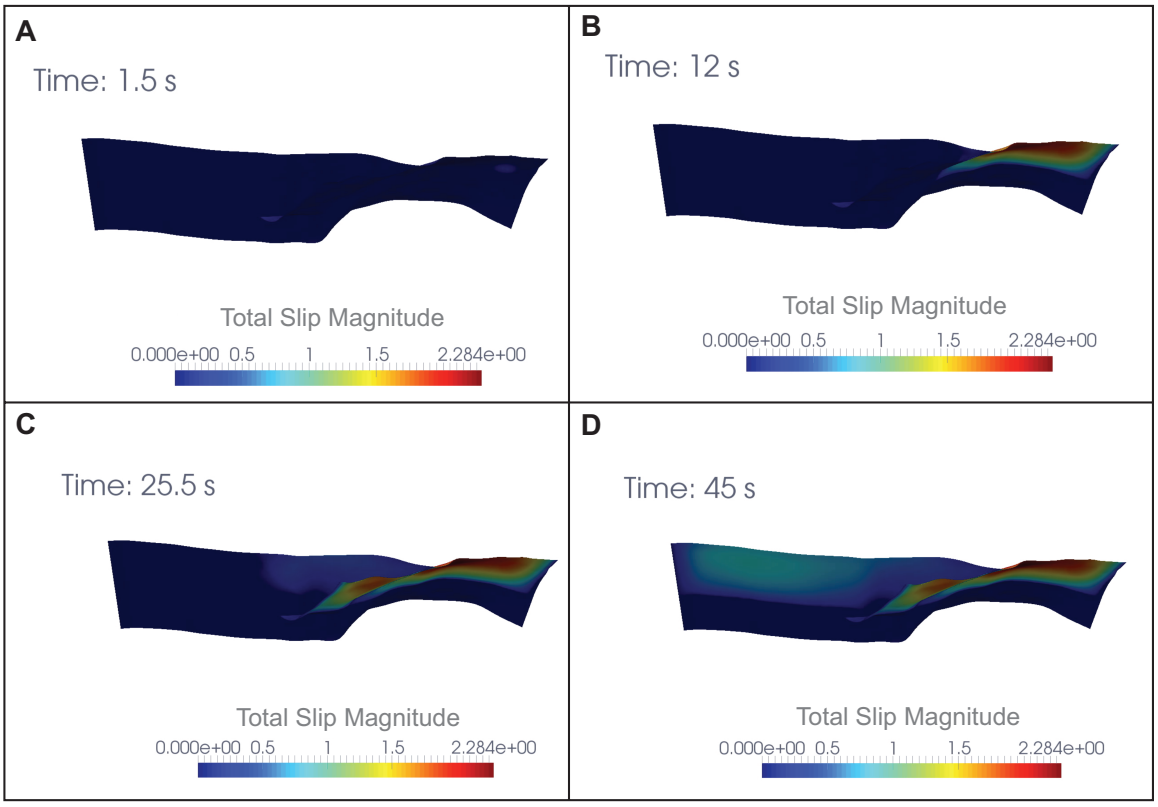

Figure 2.5. Example of Through-Going Rupture. These plots show the total slip at specific times during the simulation that employs a regional stress field with $A_\phi = 1.5$ and nucleation on the GH. Total slip magnitude is given in meters. Stress shadowing caused by slip on the WSG limits slip on the SB.

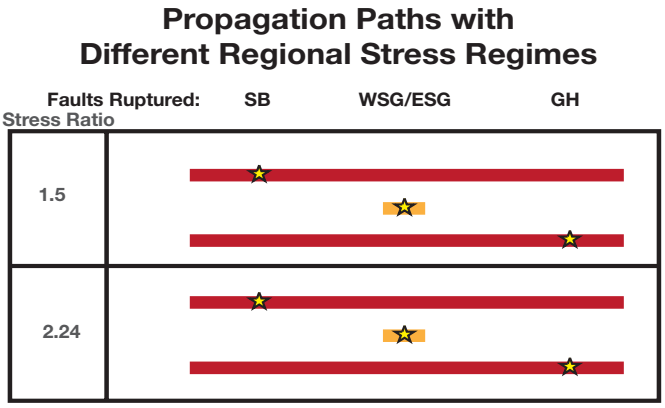

Figure 2.6. Summary of Regional Stress Model Results. Red bars indicate that a particular fault ruptured fully; orange bars indicate that only part of the fault slipped. Stars denote the fault on which rupture nucleated. For both stress ratios of $A_\phi = 1.5$ and $A_\phi = 2.24$, models that nucleated on the WSG failed to propagate out of the initial nucleation zone, while those that nucleated on the SB and GH resulted in multi fault rupture.

radius equation from *Day* (1982) to estimate that a physically unreasonably large nucleation radius on the order 30 km would be needed to allow rupture to proceed spontaneously beyond the nucleation zone on the SB. Alternatively, we estimate, that reducing the slip weakening distance, d_0, by a factor of seven, would promote spontaneous rupture. Using both S = 0.5 to generate the variable normal traction values and the smaller d_0 = 0.086 m, nucleating on the SB led to a multi-fault rupture of the entire system, while nucleating on the GH yielded results similar to the models that used S = 1.0 or S = 0.5 and a d_0 value of 0.6 (Figure 2.8). Thus we find that increasing or decreasing the (relatively unconstrained) slip weakening distance while using a highly heterogeneous stress field can have a very strong influence on the results.

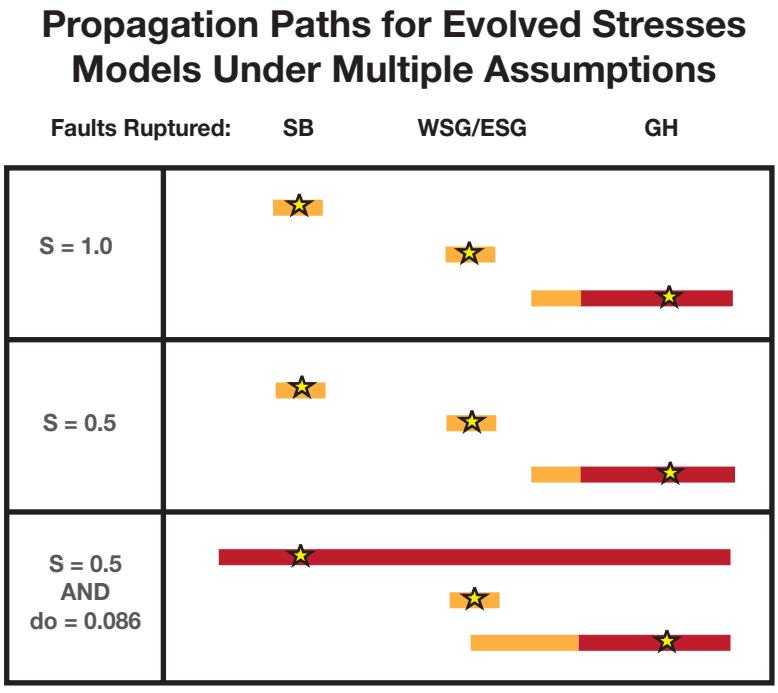

Figure 2.7. Summary of Evolved Stress Model Results. Red bars indicate that a particular fault ruptured fully; orange bars indicate that only part of the fault slipped. Stars denote the fault on which rupture nucleated. S values refer to the strength ratio used to generate the normal stresses (see Methods) and d_0 refers to the slip-weakening distance (m).

2.5. Discussion

In the case of the Constant Tractions models, the most likely cause for rupture terminating abruptly is the orientation of the initial stress field. The abrupt rotation of the stress field from pure right-lateral strike-slip to oblique right-lateral and thrust likely causes rupture to stop at these segment boundaries because the pre-stress orientation is unfavorable with the complex fault geometry (*Duan*, 2010). In this case, the pre-stress orientation swamps the effect of the dynamic stresses, which would otherwise facilitate earthquake rupture propagation. However, if there is an actual abrupt change in the orientation of the stress field within the SGP, this supports suggestions that the SGP is a barrier for rupture and that through-going earthquakes are rare (*Carena et al*., 2004; *Langenheim et al*., 2005). The effect of the shear stress orientation is so dominant that including, or not including, a linear gradient with the normal stresses appears to have almost no effect on the results.

The $A_\phi = 1.5$ Regional Stress models suggest that directivity may play a key role in the ability of through-going rupture scenarios in the SGP. Nucleating along the Garnet Hill and San Bernardino strands causes multi-fault rupture. However, nucleating from within the SGP does not lead to a multi-fault rupture scenario. This suggests that it is the dynamic stress changes from the initial stages of the earthquake, causing a build up of shear stress ahead of a rupture front coming from either the northwest or southeast, that allows the San Gorgonio Pass Fault Zone to rupture. This directivity effect has been noted before in models of the North Anatolian Fault (*Oglesby and Mai*, 2012). The through-going scenario that starts in the southeastern part of the SGP falls in line with the

hypothesis that a hypothetically large event rupturing through the SGP could start in Bombay Beach down by the Salton Sea (*Olsen et al*., 2006).

The results of the Evolved Stresses models with both the original d_0 and the scaled d_0 values suggest that some of the faults simply are not primed for failure. The pre-stress assumptions for these models take into consideration the time since a last event on these faults. For each of the different S value and d_0 assumptions, models that nucleate on the Garnet Hill strand rupture the Garnet Hill strand entirely and propagate partially along the San Gorgonio Pass Fault Zone. This suggests that the Garnet Hill strand is primed for failure, based on the loading caused by previous events. Conversely, none of the Evolved Stresses models that nucleate on the San Gorgonio Pass Fault Zone spontaneously rupture beyond the initial nucleation patch size. This suggests the San Gorgonio Pass Fault Zone is not primed for failure. Nucleation on the San Bernardino strand also caused rupture to die out in the initial nucleation patch with $d_0 = 0.6$. However, when we tuned the d_0 value to allow rupture on the San Bernardino strand, rupture propagated across to the base of our artificially named WSG portion of the San Gorgonio Pass Fault Zone. It continued to propagate up-dip and southeastward, allowing shear stress to build up on the ESG portion as both the San Bernardino strand and the WSG portion slipped. Eventually the entirety of the San Gorgonio Pass Fault Zone and the Garnet Hill strand ruptured as well in an example of through-going rupture. Paleoseismicity indicates that it has been roughly 400 years since the San Bernardino strand failed in a large earthquake (*McGill et al*., 2002), which is relatively recent and may explain why it is not primed for failure with our evolved stress assumptions. Further

investigation may be needed to see whether it is possible to fine-tune d_0 in a way that could produce a through-going rupture scenario with nucleation on the San Gorgonio Pass Fault Zone.

The results from the Evolved Stresses models also suggest that slip-weakening friction with a constant d_0 parameter may not be a compatible assumption with very heterogeneous initial stresses and geometry. There is large uncertainty about the d_0 parameter and its physical interpretation that makes it difficult to assess a reasonable numerical value for the parameter (*Day*, 1982). Given the sensitivities of this parameter with the evolved stress results, it may be necessary to explore the compatibility of time-weakening friction (*Andrews*, 1985) with highly variable initial stresses.

2.6. Conclusions

The results are not robust with respect to the input parameters, which implies that the pre-stress assumptions have a strong influence on the results of models with complex geometries. Models that nucleate on the San Bernardino strand and Garnet Hill strands are most sensitive to the pre-stress conditions. Nucleation on the San Bernardino strand results in single-fault rupture in the Constant Tractions models, through-going rupture in both sets of Regional Stress models, and through-going rupture in the Evolved Stresses models, only after parameters were fine-tuned to allow failure on the San Bernardino strand. Models that nucleate on the Garnet Hill strand result in single-fault rupture in the Constant Tractions models, through-going rupture in both sets of Regional Stress models, and multi-fault (but not through-going) rupture in all of the Evolved Stresses models.

Models that nucleate on the San Gorgonio Pass Fault Zone have the most robust result, which demonstrates that it is difficult for rupture to propagate outward towards either the San Bernardino strand or the Garnet Hill strand of the SAF.

Considering this summary of the results, we conclude that while not impossible, through-going rupture in the SGP is likely limited to specific stress conditions and dependent on nucleation location. It is likely not a common occurrence because differences in the pre-stress conditions can completely shut off rupture that occurred under a different set of assumptions. Results from the Evolved Stresses models support the conclusions of *Carena et al*. (2004) that the SGP region can act as a barrier for through-going rupture, while the Regional Stress models show it can occasionally facilitate through-going rupture from earthquakes initiating from either the northwest or southeast (e.g. *Carena et al*., 2004); *Olsen et al*., 2006). The difficulty with rupture along the San Gorgonio Pass Fault Zone may be an indication that this particular interpretation of SGP fault geometry strongly influences rupture at the possible intersection of the San Bernardino strand and the San Gorgonio Pass Fault Zone, regardless of the pre-stress conditions. We would need to conduct further investigations with alternate fault geometries to understand how strongly this fault geometry interpretation influences the results. Further investigation on pre-stress assumptions in dynamic rupture models is also necessary because it is clear that it has a significant effect on rupture propagation paths and it must be well understood in order to provide the seismological community with valuable results in geologically complex areas.

2.7. References

Aagaard, B.T., G. Anderson, and K.W. Hudnut (2004), Dynamic rupture modeling of the transition from thrust to strike-slip motion in the 2002 Denali Fault, Alaska, earthquake, *Bulletin of the Seismological Society of America*, *94*(6B), S190-S201.

Allen, C. R. (1957), San Andreas fault zone in San Gorgonio Pass, Southern California, *Geological Society of America Bulletin*, *68*, 315-350.

Andrews, D. J. (1976), Rupture velocity of plane strain shear cracks, *Journal of Geophysical Research*, *81*(32), 5679-5687.

Andrews, D.J., (1985), Dynamic plane-strain shear rupture with a slip-weakening friction law calculated by a boundary integral method, *Bull. Seismol. Soc. Am.*, 75(1), 1-21.

Aochi, H., E. Fukuyama, and M. Matsu'ura (2000), Selectivity of spontaneous rupture propagation on a branched fault, *Geophysical Research Letters*, *27*(22), 3635-3638.

Barall, M. (2009), A grid-doubling technique for calculating dynamic three-dimensional spontaneous rupture on an earthquake fault, *Geophysical Journal International*, *178*, 845-859.

Bhat, H.S., R. Dmowska, J.R. Rice, and N. Kame (2004), Dynamic slip transfer from the Denali to Totschunda Faults, Alaska: Testing theory for fault branching, *Bulletin of the Seismological Society of America*, *94*, S202-S213.

Carena, S., J. Suppe, and H. Kao (2004), Lack of continuity of the San Andreas fault in Southern California: Three-dimensional fault models and earthquake scenarios, *Journal of Geophysical Research*, *109*, B04313, doi:04310.01029/02003JB002643.

Cooke, M. L., and L. C. Dair (2011), Simulating the recent evolution of the southern big bend of the San Andreas fault, Southern California, *Journal of Geophysical Research*, *116*, B04405, doi:04410.01029/02010JB007835.

Dair, L., and M. L. Cooke (2009), San Andreas fault geometry through the san Gorgonio Pass, California, *Geology*, *37*(2), 119-122.

Das, S., and K. Aki (1977), Fault plane with barriers: A versatile earthquake model, *Journal of Geophysical Research*, *82*(36), 5658-5670.

Day, S. M. (1982), Three-dimensional simulation of spontaneous rupture: The effect of nonuniform prestress, *Bulletin of the Seismological Society of America*, *72*(6), 1881-1902.

Dieterich, J. (1978), Time-dependent friction and the mechanics of stick-slip, *Pure and Applied Geophysics*, *116*(4-5), 790-806.

Dieterich, J. (1976), Modeling of rock friction. 1. Experimental results and constitutive equations, *Journal of Geophysical Research*, *84*, 2161-2168.

Duan, B. (2010), Role of initial stress rotations in rupture dynamics and ground motion: A case study with implications for the Wenchuan earthquake, *J. Geophys. Res*., *115*, B05301, doi:10.1029/2009JB006750.

Duan, B., and D.D. Oglesby, 2007, Nonuniform prestress from prior earthquakes and the effect on dynamics of branched fault systems, *J. of Geophys. Res.*, *112*, B05308, doi:10.1029/2006JB004443.

Fattaruso, L., M.L. Cooke, and R.J. Dorsey (2014), Sensitivity of uplift patterns to dip of the San Andreas fault in the Coachella Valley, California, *Geosphere*, *10*(6), 235–1246; doi:10.1130/GES01050.1.

Fliss, S., H.S. Bhat, R. Dmowska, and J.R. Rice (2005), Fault branching and rupture directivity, *Journal of Geophysical Research*, *110* (B6), B06312, doi:10.1029/2004JB003368.

Gilchrist, J.J. (2015), Applications of Multi-Cycle Earthquake Simulations to Earthquake Hazard. UC Riverside: Geological Sciences. Retrieved from: http://escholarship.org/uc/item/6zv6912f.

Hardebeck, J.L., Hauksson, E., (2001), Stress Orientations Obtained from Earthquake Focal Mechanisms: What Are Appropriate Uncertainty Estimates, *Bulletin of the Seismological Society of America*, 91, 2, pp. 250-262.

Harris, R. A., and S. M. Day (1993), Dynamics of Fault Interaction - Parallel Strike-Slip Faults, *Journal of Geophysical Research*, *98*(B3), 4461-4472.

Heaton T. H. (1990), Evidence for and implications of self-healing pulses of slip in earthquake rupture, *Physics of the Earth and Planetary Interiors*, *64*, 1-20.

Herbert, J.W., and M.L. Cooke (2012), Sensitivity of the southern San Andreas fault system to tectonic bound- ary conditions and fault configurations, *Bull. of the Seis. Soc. of Am.*, *102*, 2046– 2062, doi: 10 .1785 /0120110316.

Herbert, J.W. et al. (2014), How much can off-fault deformation contribute to the slip rate discrepancy within the eastern California shear zone?, *Geology*, *42*, 71 – 74.

Ida, Y. (1972), Cohesive force across the tip of a longitudinal-shear crack and Griffith's specific surface energy, *J. of Geophys. Res.*, *77*(20), 3796-3805.

Kame, N., J. R. Rice, and R. Dmowska (2003), Effects of pre-stress state and rupture velocity on dynamic fault branching, *Journal of Geophysical Research*, *108*(B5), 2265, doi: 2210.1029/2002JB002189.

Kendrick, K. J., J. C. Matti, S. A. Mahan, G. P. Landis, and D. P. Miggins (2011), Depositional constraints on slip along the San Andreas fault within the eastern San Gorgonio Pass region, Southern California, *2011 SCEC Annual Meeting Program*, A-135.

Kendrick, K.J., J.C. Matti, and S. Mahan (2015), Late Quaternary slip history of the Mill Creek strand of the San Andreas fault in San Gorgonio Pass, southern California: The role of a subsidiary left-lateral fault in strand switching, Geol. Soc. of Am. Bull, 127, 825-849, doi:10.1130/B31101.1.

Kyriakopoulos, C., G. Funning, D.D. Oglesby, J.M. Fletcher, and K.J. Ryan (2015), The M7.2 2010 El-Mayor-Cucapah Earthquake: How much of the Complexity Can We Explain With Our Models?, *American Geophysical Union, Fall Meeting 2015*, abstract #T51H-02.

Langenheim, V. E., R. C. Jachens, J. C. Matti, E. Hauksson, D. M. Morton, and A. Christensen (2005), Geophysical evidence for wedging in the San Gorgonio Pass structural knot, southern San Andreas fault zone, Southern California, *Geological Society of America Bulletin*, *117*.

Lozos, J. C., D. D. Oglesby, B. Duan, and S. G. Wesnousky (2011), The effects of double fault bends on rupture propagation: a geometrical parameter study, *Bulletin of the Seismological Society of America*, *101*(1), 385-398.

Lozos, J. C., D. D. Oglesby, J. N. Brune, and K. B. Olsen (2012), Small intermediate fault segments can either aid or hinder rupture propagation at stepovers, *Geophysical Research Letters*, *39(*18), DOI: 10.1029/2012GL053005.

Mac Donald, B. J. (2007), *Practical Stress Analysis with Finite Elements*, Glasnevin Publishing: Dublin, Ireland.

Madariaga R., K. Olsen, and R. Archuleta, Modeling Dynamic Rupture in a 3D earthquake fault model, *Bulletin of the Seismological Society of America*, *88*(5), 1182-1197.

Marshall, S.T., Cooke, M.L., Owen, S.E., (2009), Interseismic deformation associated with three-dimensional faults in the greater Los Angeles region, California, *J. Geophys. Res.*, 114, B12.

Matti, J. C., and D. M. Morton (1993), Paleogegraphic evolution of the San Andreas fault in Southern California: A reconstruction based on a new cross-fault correlation, in *The San Andreas fault system: Displacement, palinspastic reconstruction, and geologic evolution*, edited by R. E. Powell, R. E. I. Weldon and J. C. Matti, pp. 107-159, Geological Society of America.

Matti, J.C., B.F. Cox, C.M., Obi, R.E. Powell, M.E. Hinkle, Griscom, Andrew, and E.L. McHugh, (1982), Mineral resource potential of the Whitewater Wilderness Study Area, Riverside and San Bernardino Counties, California, *U.S. Geological Survey Miscellaneous Field Studies Map MF-1478*, scale 1:62,500.

Matti, J. C., D. M. Morton, and B. F. Cox (1985), Distribution and geologic relations of fault systems in the vicinity of the central Transverse Ranges, southern California, scale 1:250,000, *U.S. Geol. Surv. Open File Rep.*, *85-365*.

Matti, J.C., D.M. Morton, and B.F., Cox (1992), The San Andreas fault system in the vicinity of the central Transverse Ranges Province, southern California, U.S. Geological Survey Open-File Report 92-354, 40, scale 1:250,000.

Meade, B. J., and B. H. Hager (2005), Block models of crustal motion in Southern California constrained by GPS measurements, *Journal of Geophysical Research*, *110*.

McGill S., Dergham S., Barton K., Berney-Ficklin T., Grant D., Hartling C., Hobart K., Minnich R., Rodriguez M., Runnerstrom E., Russell J., Schmoker K., Stumfall M., Townsend J., Williams J., (2002), Paleoseismology of the San Andreas fault at Plunge Creek, near San Bernardino, southern California. *Bull. Seismol. Soc. Am*. 92, 2803–2840.

Oglesby, D. D. (2005), The dynamics of strike-slip step-overs with linking dip-slip faults, *Bulletin of the Seismological Society of America*, *95*(5), 1604-1622.

Oglesby, D.D., S.M. Day, Y.-G. Li, and J.E. Vidale (2003a), The 1999 Hector Mine earthquake: the dynamics of a branched fault system, *Bulletin of the Seismological Society of America*, *93*(6), 2459-2476.

Oglesby, D.D., S.M. Day, and D.R.H. O'Connell (2003b), The dynamic and static interaction of two thrust faults: a case study with general implications, *Journal of Geophysical Research*, *108* (B10), 2489, doi:10.1029/2002JB002228.

Ohnaka, M. (1996), Nonuniformity of the constitutive law parameters for shear rupture and quasistatic nucleation to dynamic rupture: A physical model of earthquake generation processes, *Proceedings of the National Academy of Sciences of the United States of America*, *93*(9), 3795-3802.

Ohnaka, M. and Y. Kuwahara (1990), Characteristic features of local breakdown near crack-tip in the transition zone from nucleation to dynamic rupture during stick-slip shear failure, *Tectonophysics*, *175*, 197-220.

Olsen, K. B., S. M. Day, J. B. Minster, Y. Cui, A. Chourasia, D. Okaya, P. Maechling, and T. Jordan (2008), TeraShake2: Spontaneous rupture simulations of M-w 7.7 earthquakes on the southern San Andreas fault, *Bulletin of the Seismological Society of America*, *98*(3), 1162-1185.

Olsen, K. B., S. M. Day, J. B. Minster, Y. Cui, A. Chourasia, M. Faerman, R. Moore, P. Maechling, and T. Jordan (2006), Strong shaking in Los Angeles expected from southern San Andreas, *Geophysical Research Letters*, *33*, L07305, doi:07310.01029/02005GL025472.

Plesch, A., et al. (2007), Community Fault Model (CFM) for Southern California, *Bulletin of the Seismological Society of America*, *97*(6), 1793-1802.

Ramzan, S. (2012), Paleoseismic investigation of the San Gorgonio Pass fault zone near Cabazon, California, California State University, Northridge.

Ruina, A., (1983), Slip Instability and State Variable Friction Laws, *J. Geophys. Res.*, 88, B1210359-10370.

Scharer, K. M., D. Yule, L. R. Humbert, R. Witkowsky (2013), Implications for San Andreas Fault Ruptures Based on New Evidence from the Cabazon, CA Paleoseismic Site, San Gorgonio Pass Fault Zone, *American Geophysical Union, Fall Meeting 2013*, abstract #T43A-2622.

Simpson, R.W. (1997), Quantifying Anderson's fault types, *J. Geophys. Res.*, 102, B817909-17919.

Smith, B. R., and D. T. Sandwell (2006), A model of the earthquake cycle along the San Andreas fault system for the past 1000 years, *Journal of Geophysical Research*, *111*.

Stern, A. and M. L. Cooke (2014), An approach for calculating absolute stress from stressing rate, *Southern California Earthquake Center, Annual Meeting 2014*, poster.

Taylor, J. R. (2005), *Classical Mechanics*, University Science Books: USA.

Templeton, E. L., H. S. Bhat, R. Dmowska, and J. R. Rice (2009), Dynamic rupture through a branched fault configuration at Yucca Mountain and resulting ground motions, *Bulletin of the Seismological Society of America, 100*(4), 1485-1497.

Yamashita, T., Umeda, Y., (1994), Earthquake rupture complexity due to dynamic nucleation and interaction of subsidiary faults, *Pure Appl. Geophys.*, 143, 89-116.

Yule, D. (2009), The enigmatic San Gorgonio Pass, *Geology*, *37*(2), 191-192.

Yule, D., and K. E. Sieh (2003), Complexities of the San Andreas fault near San Gorgonio Pass: Implications for large earthquakes, *Journal of Geophysical Research*, *108*(B11), doi:10.1029/2001JB000451.

Zhang, H., Y. Z. Zhou, Z. L. Wu, Z. Z. Yan, S. Chen, H. M. Jing, X. W. Xu, Y. L. Shi (2009), Finite element analysis of seismic wave propagation in Fuzhou Basin, *Chinese Journal of Geophysics*, *52*(3), 604-614.

2.8. Tables

Table 2.1. Constant Traction Models: Physical and Computational Parameters

P-wave Velocity	**S-wave Velocity**	**Density**
5477 m/s	3162 m/s	2700 kg/m^3
Static Friction	**Dynamic Friction**	**Slip Weakening Distance**
0.84	0.42	0.6 m
Initial Shear Stress	**Initial Normal Stress**	**Nucleation Stress**
10 MPa	16.65 MPa	10.9 MPa
Small Element Size	**Large Element Size**	**Nucleation Radius**
300 m	900 m	5 km

Table 2.2. Regional Stress Models: Physical and Computational Parameters

P-wave Velocity	**S-wave Velocity**	**Density**
5477 m/s	3162 m/s	2700 kg/m^3
Static Friction	**Dynamic Friction Slip**	**Weakening Distance**
0.6	0.1	0.6 or 0.086 m
Small/Large Element Size	**Nucleation Radius**	**Nucleation Stress**
300/900 m	5 km	10% > Initial Stress

Stress Tensor Variation	σ_{00}	σ_{01}	σ_{02}	σ_{10}	σ_{11}	σ_{12}	σ_{20}	σ_{21}	σ_{22} **(MPa)**
$A_\phi = 1.5$	53	0	0	0	41.3	-3.76	0	-3.76	20.7
$A_\phi = 2.24$	69	0	0	0	42.4	-3.59	0	-3.59	22.6

Table 2.3. Evolved Stress Models: Physical and Computational Parameters

P-wave Velocity	**S-wave Velocity**	**Density**
5477 m/s	3162 m/s	2700 kg/m^3
Static Friction	**Dynamic Friction**	**Slip Weakening Distance**
0.6	0.1	0.6 or 0.086 m
Initial Shear Stress	**Initial Normal Stress**	**Nucleation Stress**
Variable (~1-6 MPa)	Variable (~1-14 MPa)	10% > Initial Stress
Small Element Size	**Large Element Size**	**Nucleation Radius**
300 m	900 m	5 km

Chapter 3

Remotely Triggered Earthquakes Along the San Jacinto Fault Zone, CA

3.1. Abstract

Remote earthquake triggering across the globe is a well-documented phenomenon (*Hill et al*., 1993). However, there is still much to understand about the controlling physical processes and methods to adequately gauge earthquake triggering for a specific region. We examine the likelihood of remote triggering along the San Jacinto Fault Zone in southern California with the β-value statistic, changes in maximum magnitude, and visual scans of the seismic data. Out of 549 remote events in a ten-year period, we find that 14 remote events triggered the San Jacinto Fault Zone. We find that the β-value statistic alone is not a strong enough indicator of triggering in the San Jacinto region, but combining it with peak magnitude analysis can provide statistically significant results. Despite using multiple methods to detect triggered events, the SJFZ still appears to be infrequently triggered.

3.2. Introduction

Earthquakes can trigger other earthquakes on a variety of spatial and temporal scales (e.g. *Hill et al*., 1993). Local aftershock sequences following a main shock are the most familiar examples of triggering and are representative of rapid triggering in a relatively small area. Large magnitude events can also trigger small earthquakes hundreds to thousands of kilometers away from the initial main shock (*Hill et al*., 1993; *Hill and Prejean*, 2007). *Velasco et al.* (2008) indicate that several $M_w \geq 7.0$ earthquakes between 1990 and 2008 triggered smaller earthquakes in multiple remote locations across the globe and numerous studies show significant increases in seismicity ranging from

minutes to days after a large event (e.g. *Hill et al*., 1993; *Prejean et al*., 2004; *Brodsky*, 2006; *Meng and Peng*, 2014). Triggered earthquakes are important because their occurrence can provide information about the relative state of stress in a particular region. Absolute stresses along fault zones are difficult to obtain. However, earthquakes occur when faults are optimally oriented and critically stressed to a point where even a small increase in shear stress causes failure. Thus, triggered events can indicate the occurrence of a critically stressed state of faults in a particular region.

We systematically look for evidence of remote triggering of small local earthquakes along the San Jacinto Fault Zone (SJFZ) in southern California. Accommodating predominately right-lateral strike-slip motion, the SJFZ is the most seismically active fault zone along the Pacific and North American plate boundary (*Sharp*, 1967). Although the SJFZ is a very active zone, few studies have found instances of regional or remote triggering in this area. Qualitatively, the M_w 6.7 1994 Northridge, CA earthquake appeared to trigger local events in the Anza region of the SJFZ, but statistical tests revealed that the seismicity following the main shock did not deviate from the overall trend in the long term (*Kane et al*., 2007). More recently, there was a statistically significant increase in seismicity along the SJFZ for two to three days following the 2010 M_w 7.2 El Mayor-Cucapah earthquake and roughly 70 days of an elevated seismicity rate when compared with the pre-main shock rate (*Meng and Peng*, 2014). Dynamic stress changes are likely responsible for the initial increase in seismicity, while changes in static stress explain the longer term elevated seismicity rate in this case (*Meng and Peng*, 2014). In an attempt to find a dynamic triggering threshold

with data from the ANZA seismic network along the SJFZ, *Kane et al*. (2007) determined that out of 60 $m_b \geq 7.0$ remote events spanning 1993 to 2004, the 2001 M_w 7.3 Mariana Islands earthquake was the only remote main shock likely to have triggered events in the SJFZ. However, their attempts to find a triggering threshold with spectral amplitudes, frequencies, and maximum ground velocities led to mixed results even with local and regional events. It appears that, while possible, it is difficult and rare to detect remote triggering along the SJFZ with statistical tests that evaluate changes in the number of local events. Similarly, amplitude, frequency, and ground velocities may not be adequate indicators of the triggering capabilities of a remote event in this area.

3.3. Data and Methods

We investigate the possibility of remote triggering along the SJFZ in a 10-year timespan with two levels of tests. The first category consists of statistical tests that determine whether the number of local events following a remote event is significantly larger than prior to the remote event. The second category quantitatively examines peak magnitude of local events occurring before and after a remote event. In addition, we supplement these tests with visual scans of seismic data from stations located along the SJFZ to determine whether local events occur during the onset or passage of various phases from the remote events. This is helpful because tiny local events, especially during the passage of teleseismic waves, often remain undetected by the network. We use data from the Advanced National Seismic System (ANSS) Composite Catalog for the quantitative tests. From the ANSS catalog, we compile a remote event catalog that

consists of 549 $M_w \geq 6.5$ worldwide events from January 1, 2005 to September 30, 2015. For the purposes of this paper, we do not treat regional events differently from teleseismic events, referring to both groups as remote events. We do so because there were no $M_w \geq 6.5$ earthquakes in southern California during the selected timeframe and the apparent lack of a threshold for triggering along the SJFZ (*Kane et al*., 2007) gives us little reason to distinguish main shocks in Baja California and the Gulf of California from main shocks that occurred farther away. We compile the local events catalog from the ANSS using the region outlined in the polygon in Figure 3.1. The Anza gap and a

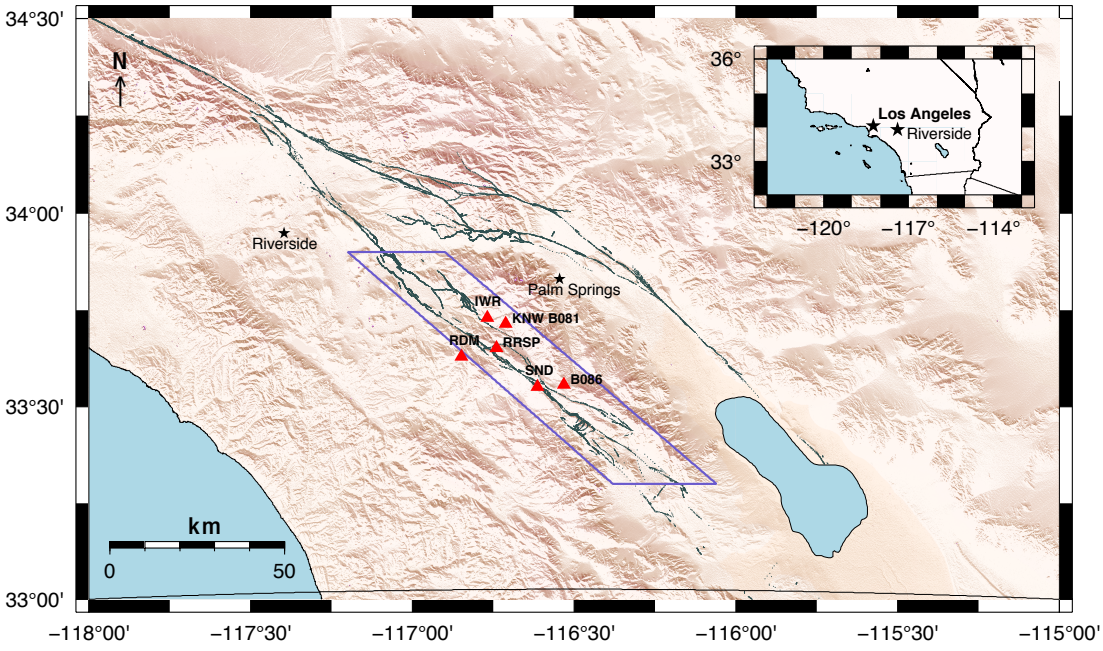

Figure 3.1. Location Map. The purple polygon outlines the study area, which is the same as the region used to gather local events from the ANSS catalog. The red triangles show the stations selected from the ANZA and PBO networks. The seismograms used in the visual scans come from these stations. Station KNW of the ANZA network is co-located with the borehole station B081 from the PBO network.

region between Cajon Pass and Riverside are known gaps in seismic activity along the SJFZ (*Thatcher*, 1975). Following the El Mayor Cucapah event, the majority of detected

events were located in the central and southern portions of the SJFZ (*Meng and Peng*, 2014). For these reasons, we focus on events that occurred within a narrow polygon around the central and southern portions of the fault (Figure 3.1). Consistency checks for magnitude calculations with the local events catalog reveal that ≥ 98.7% of the events in that catalog are M_L; the remaining events are M_h (1.29%) and M_w (0.01%). The majority of the local events are < M_L 2.0 (97.7%) and only 6 events are $M_L \geq 4.0$. We test various time windows for calculations to ensure that the higher magnitude local events do not affect the statistics with their own aftershock sequences. Histograms for all time windows are visually inspected for local events that have aftershock sequences. These events are flagged, and if they fall within the time window of a statistical calculation for a remote event, the results for that event are marked as inconclusive. We discuss more details about the time window selection process below. In general, high magnitude local events very rarely occurred within the time windows of remote events.

3.3.1 Statistical Tests

The primary statistical test we apply is the beta (β) value test (*Matthews and Reasenberg*, 1988; *Kilb et al*., 2002; *Meng and Peng*, 2014). The β-value is a measure of how the seismicity over a specific time period deviates from the background rate of seismicity. Equation 3.1 describes the β-value as

$$\beta = \frac{n_a - E(n_a)}{\mathrm{Var}(n_a)}, \tag{3.1}$$

where n_a is the number of events after a remote event, $E(n_a)$ is the expected number of events equivalent to the background rate, and $\mathrm{Var}(n_a)$ is the variance of n_a. β-values

higher or lower than ±2 indicate statistically significant deviations from the expected seismicity. We only consider the one-tailed statistical test of β-values ≥ 2 because we are interested in an increase in seismic activity as opposed to quiescence following a remote event. The β-value test assumes that it is possible to determine a background rate of seismicity accurately describing the mean number of earthquakes per day in the region. Due to the inherent variability in the processes that cause the number of earthquakes occurring each day to fluctuate, we choose to calculate multiple β-values for each event with background rates from a variety of time intervals. To obtain $E(n_a)$, we take the mean of the seismicity over 30, 25, 20, 15, 10, 5, 4, 3, and 2-day time intervals preceding each remote event to ensure a robust result. We take a 1-day time interval for the value of n_a and a 30-day interval for $E(n_a)$ in the final results. The local events catalog spans December 1, 2004 to October 31, 2015 to facilitate the background rate calculation.

To test the statistical significance of our results, we generate a catalog of 2000 random times spanning the same time period as the local events catalog. The Random Times Catalog allows us to test whether the occurrence of β-values ≥ 2 and increases in maximum magnitude following remote events are by random chance due to the regular fluctuation of the background rate. The random times are generated with a uniform distribution and then filtered to remove 48 hours before and after $M_w \geq 6.5$ remote events and $M_w \geq 2.2$ local events. It eliminates randomly generated times that occur within a potential triggering window and are therefore, not representative of the background rate fluctuation. This results in a catalog of 945 random times.

The ANSS catalog completeness level may have an affect on our results. During this study, we noticed two updates to the catalog that did change the number of total events in the selected polygonal region during the 10-year time span used in this investigation. We also see small local events (S-P time less than 2 seconds) in the borehole stations that are not listed in the ANSS catalog. The completeness of the catalog could significantly affect the β-value calculation, but it is not likely that it affects the magnitude analysis. Larger magnitude events are less likely to be absent from the ANSS catalog.

3.4. Results

For each of the 549 remote events, when we use a background rate calculated over 30 days and seismicity for 1 day following the event, we find that 25 of the remote events have a β-value ≥ 2. These 25 events are considered triggering candidates (Table 3.1). Of these candidates, 22 events are included in a stacked histogram (Figure 3.2). Outliers such as the El Mayor Cucapah earthquake, a known example of triggering along the SJFZ (*Meng and Peng*, 2014), are not included. The M_w 7.5 Bay of Bengal event is another outlier because of the sheer number of local events; it also falls within the time period of long-term elevated seismicity identified by *Meng and Peng* (2014). The final outlier is a March 10, 2013 M_w 6.5 Papua New Guinea event. In the 24-hour period following that event, there was a local Mw 4.7 with an aftershock sequence. We could not determine from the statistics alone whether the Papua New Guinea event triggered the large local event and even after visually scanning the seismograms, we could not

confidently correlate the two events, hence the outlier status. Even without considering the outliers, Figure 3.2 shows that there is a statistically significantly larger number of earthquakes in the 48 hours after the remote events compared to the background rate.

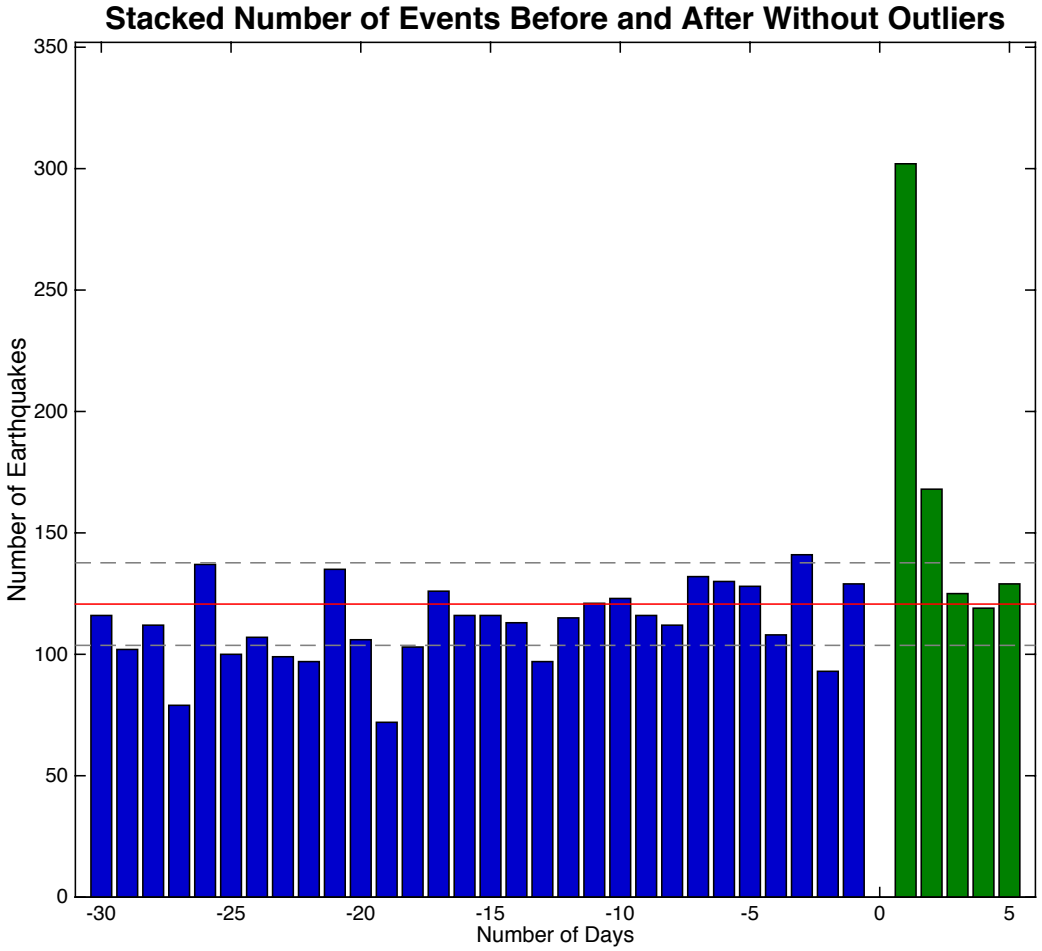

Figure 3.2. Stacked Histogram. Blue bars are days preceding remote events and green bars are days following remote events. Although there is a gap at zero, it just marks the remote events. Earthquakes are binned in 1-day intervals, so -1 is the 24-hour period preceding remote events, +1 is the 24-hour period following remote events, and so on. The solid red line is the mean and the dashed gray line is the standard deviation from the background rate.

However, when we compare the percentage of remote events with a β-value ≥ 2 to the percentage of times from the Random Times Catalog that also have a β-value ≥ 2, the

results are not statistically significant (Figure 3.3a). Regardless of the number of days used to calculate the background rate for the β-value calculation, the percentage of remote events that have a high β-value fits within the uncertainty of random chance. In other words, picking either a random time or a remote event from our catalogs will have roughly the same likelihood of having a β-value ≥ 2.

Although we find that using the β-value statistic alone is not a strong indicator of triggering along the SJFZ, it is valuable when combined with magnitude analysis. For all times in both the real and random times catalogs, the likelihood of having the maximum magnitude event during a 1-day period following a selected time is equivalent to the 50/50 probability of a coin flip if the local events are not affected by external stress (in this case, dynamic stress from remote earthquakes). Out of the 25 triggering candidates, 80% have a higher peak (maximum) magnitude local event in the 24 hours following the remote event compared to 24 hours preceding the remote event. Using larger time windows to evaluate the maximum magnitude (e.g. 72 hours before and after), over 70% of the events have a higher maximum magnitude following the remote event, before stabilizing at about 60% with time windows greater than 5 days. Considering only the β-values calculated with a background rate averaged over 30 days, we compare the total number of remote events with both a β-value ≥ 2 and a peak magnitude following the selected time to the same results for the total number of times in the Random Times Catalog (Figure 3.3b). With the combined β-value and peak magnitude metrics, the real remote events have a statistically higher percentage of events that pass both the β-value and peak magnitude test compared to the Random Times Catalog. Even with larger time

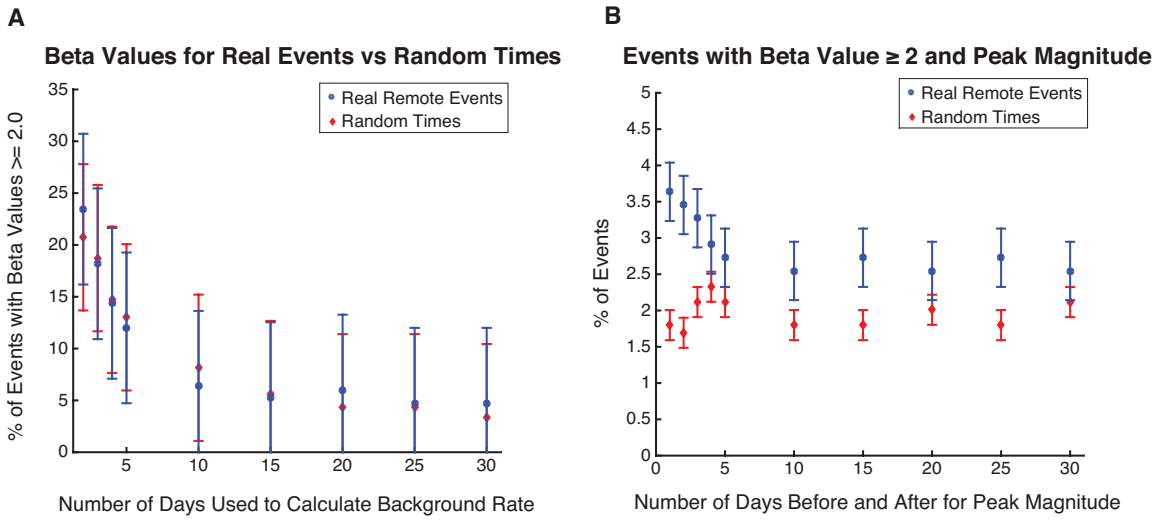

Figure 3.3. Comparison of β-value and Magnitude Statistics. (A) Percentage of events from the catalog of real remote events (blue) and the Random Times Catalog (red) that have a β-value ≥ 2. Results obtained with different time windows for the background rate estimation are plotted in the x-direction. (B) Percentage of events for both catalogs that have both a β-value ≥ 2 and a higher magnitude local earthquake that occurs after an event. Note that the x-axis marks the time window around an event for the peak magnitude determination. Percentages are out of 549 and 945 events for the real remote events and the Random Times Catalog, respectively.

windows for the peak magnitude determination, such as 15 or 25 days, the real remote events have a significantly higher number of events that pass both metrics.

While the combined β-value and peak magnitude tests provide statistically significant results, we visually verify that the results are consistent with each remote event. In addition to the stacked histogram in Figure 3.2, we examine the seismograms for supporting evidence of triggering. This additional corroboration is useful because the signal of triggering in this area is subtle. Unlike the 2010 April 4 El Mayor Cucapah event, many of the histograms for the other triggering candidates do not have triggered sequences that look "obvious." We use data from broadband sensors in the ANZA (AZ) network and two borehole stations from the Plate Boundary Observatory (PBO) network (Figure 3.1). We filter the data between 0.01 and 1 Hz to view the remote events and

filter between 1 to 15 Hz, or 5 to 20 Hz to best view local events, depending on data quality. Based on the size of the study area, we consider earthquakes with S-P times ≤ 6.7 seconds to be local earthquakes. An M_w 6.7, 2007 August 2 earthquake along the Aleutian Trench is an example of a triggering candidate that passes the peak magnitude test in a 48-hour time window (Figure 3.4a) and although the histogram is not particularly impressive (Figure 3.4b), small local earthquakes coincide with the passing body and surface waves of the Aleutian Trench event (Figure 3.4c). Seismograms of a 2007 August 1 M_w 7.2 Vanuatu event reveal that there are several local events (S-P wave arrival time is ~2 seconds) during the passage of the Rayleigh waves from the remote event, detected at the hard rock site KNW station in the AZ network. Similarly, a smaller M_w 6.5, 2006 May 22 event in Russia coincides with local earthquakes that occur during the passage of the teleseismic body waves from the Russian event. In general, the seismic data determined whether we rejected triggering candidates, designated them as likely-triggering, or triggering events. We rejected the Papua New Guinea event on the basis that there was a clear local main shock and aftershock sequence fairly soon after the event.

For 11 of the events with a β-value ≥ 2 (and peak magnitude event following the remote earthquake), the seismic data shows that local earthquakes occur during or very soon after the passage of various phases from the remote events, regardless of what pattern is visible in the histograms. Some events are too tiny to be detected by the network, and therefore not recorded in the standard catalog. For 3 of the events, during the passage of teleseismic waves, we see several events that have S-P times or 1-2 s

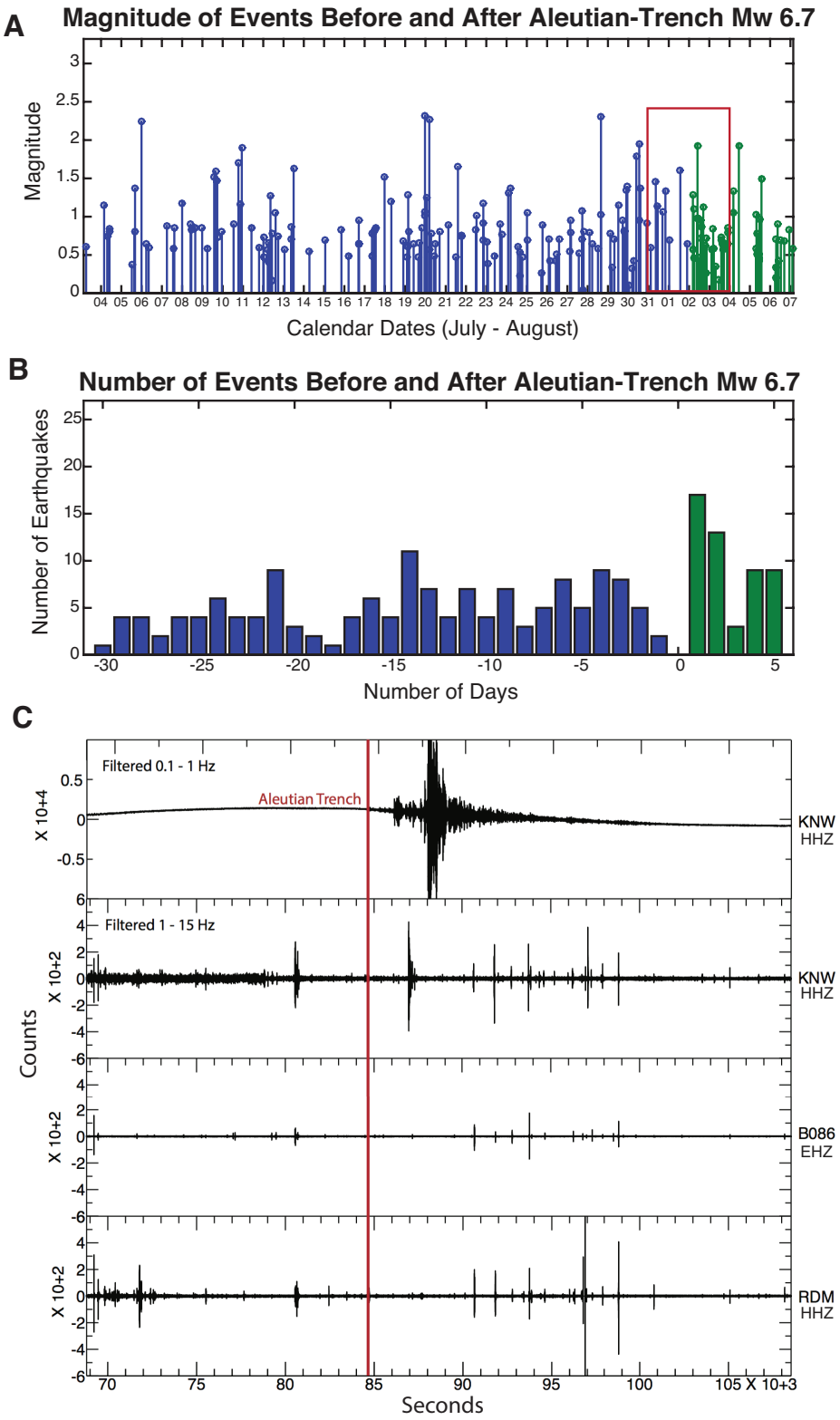
A
Magnitude of Events Before and After Aleutian-Trench Mw 6.7
Magnitude
Calendar Dates (July - August)
B
Number of Events Before and After Aleutian-Trench Mw 6.7
Number of Earthquakes
Number of Days
C
Filtered 0.1 - 1 Hz
Aleutian Trench
KNW HHZ
Filtered 1 - 15 Hz
KNW HHZ
B086 EHZ
RDM HHZ
Counts
X 10+4
X 10+2
Seconds

Figure 3.4. Summary of Aleutian Trench Event. (A) Stem plots of local earthquake magnitudes. Blue stems are for earthquakes preceding the remote event and green are for earthquakes following it. The red rectangle highlights 48 hours before and after the remote event. (B) Histogram showing the number of local earthquakes before and after the remote event. (C) Seismograms showing roughly 4 hours before and 7 hours after the remote event. The red line marks the arrival of the P wave at station KNW. Around the arrival of the S wave there are two very small local events; several larger local events occur after the surface waves start to pass through the area.

larger than our 6.7s cut-off for local events, implying local triggering even if they did not fit perfectly within our polygonal study area. The 3 events also have local peak magnitude events following the remote earthquake for larger time windows (i.e. 20 - 30 days before and after). We consider the 14 events discussed above to be triggering events, and the remaining 10 candidates are designated as likely-triggering events. In short, a good portion of the triggered episodes detected in this study using solely the catalog show compelling visual evidence of triggering.

We attempt to find a distinguishing similarity amongst the events that have β-values ≥ 2, greater peak magnitudes following a remote event, and local earthquakes that occur during the passage of waves from the remote events. We first look for a simple relationship between magnitude of the remote earthquake and β-values ≥ 2. There is no significant correlation between the two for the region we selected. We calculate the peak amplitude with the surface wave and amplitude relationship from *Lay and Wallace* (1995) as implemented by *Van der Elst et al.* (2010) with

$$\log_{10} A_{20} = M_s - 1.66 \log_{10} \Delta - 2. \quad (3.2)$$

We use the surface wave magnitude (M_s) from the GCMT catalog and the latitude and longitude of AZ station KNW as the reference point for the calculation of Δ, which is in distance degrees. El Mayor Cucapah is an outlier, far exceeding any of the other remote events with the highest peak amplitude (Figure 3.5). The 2012 Baja California and the 2012 October 28, M_w 7.8 Queen Charlotte, Canada event are the only other events with β-values ≥ 2 that have relatively high peak amplitudes. All three of these events did have

larger magnitude local earthquakes following their occurrence, but aside from these three events, there was no significant correlation of remote triggering and peak amplitude.

Although we calculate peak theoretical amplitudes for all 549 remote events, we calculate dynamic stresses from the seismograms for the 25 triggering candidates using the following approximation for the dynamic strain from *Love* (1927),

$$\varepsilon \approx \frac{A}{\Lambda} \approx \frac{V}{C_s}, \tag{3.3}$$

where A is displacement amplitude, which is roughly proportional to particle velocity (V) and Λ is wavelength proportional to seismic wave velocity (C_s). We assume average Rayleigh wave speeds of 3.2 km/s from *Lay and Wallace* (1995) for C_s. We use Hooke's Law for the dynamic stress relationship and assume 30 GPa for the shear modulus μ (*Stein and Wysession*, 2003). Our values range from 0.1 – 13 kPa, with El Mayor Cucapah as at outlier at 557 kPa. This large dynamic stress range is consistent with *Linville et al*. (2014), in which the authors found main shocks with peak dynamic stresses ranging from 0.001 – 34 kPa that triggered events in the southeastern United States. Similar to *Kane et al*. (2007), we find no single, obvious, distinguishing threshold for triggering along the SJFZ.

3.5. Discussion

Applying statistical tests involving combination of number of events and magnitudes using a standard earthquake catalog, we are able to tease out the small but statistically significant signal hidden in noisy data along the SJFZ. Each set of tests

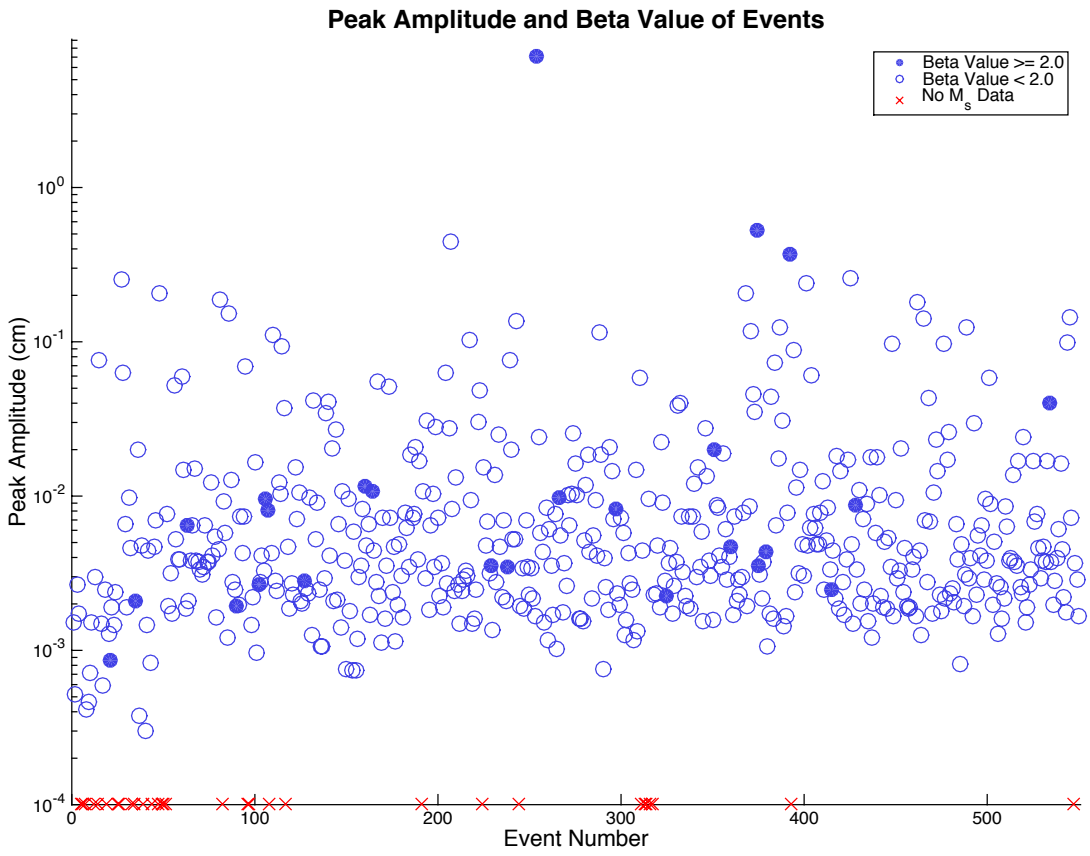

Figure 3.5. Peak Theoretical Amplitudes. M_s values are from the Global Centroid Moment Tensor catalog. The outlier is the El Mayor Cucapah event. The second highest value is another regional event in Baja California. Red x's mark events that do not have a surface wave magnitude in the Global CMT catalog and subsequently have no peak theoretical amplitude calculation.

reduces the number of likely candidates for remote triggering, leaving us, conservatively with 14 events that triggered local earthquakes along the SFJZ (Table 3.2). Due to the fact that all of the candidates for earthquake triggering are remote events at teleseismic distance, dynamic stresses are most likely responsible for the triggering (*Hill et al.*, 1993; *Kilb et al.*, 2000). Dynamic stresses are transient, oscillatory stresses transmitted via seismic waves and previous studies of triggering along the SJFZ cite dynamic triggering as the mechanism in this region (*Kane et al.*, 2007; *Meng and Peng*, 2014).

The occurrence of a peak magnitude in local earthquakes following triggering teleseismic events suggests that dynamic stresses may be able to produce not only more events, but also larger events. This implies that remote events perhaps can lead to the preferential failure of larger asperities along the SJFZ. Thus far, it is relatively rare to find large ($M_w \geq 5.5$) events triggered teleseismically anywhere on the globe (*Johnson et al*., 2015) and we do not see such large triggered events in our peak magnitude analysis either. We propose that considering magnitude of events before and after dynamic stress is a useful criterion for identifying dynamic triggering. It may be more useful to determine whether the relative magnitude is larger in a specific region following a teleseismic event, instead of selectively searching for magnitude thresholds or exceptionally large locally triggered events. Considering the wide range of dynamic stress values associated with various triggered episodes in the southeastern United States (*Linville et al*., 2014), each region may have a unique combination of contributing factors to facilitate triggering.

There is much debate about the physical causes of dynamic triggering. This is not an exhaustive list, but some of the physical processes that could affect triggering include pore fluid pressure, tectonic and micro-scale stress heterogeneities, fault orientation, directivity, and various forms of post-seismic relaxation (*Brodsky and van der Elst*, 2014; *Gomberg et al*., 2001; *Hill*, 2008; *Freed and Lin*, 2001). Pore fluid pressure could be a factor in the SJFZ through rare instances of fluid activation. Dynamic stress changes affect permeability and fluid transport subsequently causing a re-distribution of pore pressure that makes a rock volume more susceptible to failure (*Brodsky et al.* 2003; *Wang*

and Manga, 2009; *Elkhoury et al*., 2011). *Kane et al*. (2007) suggest that the distribution of fluids along the SJFZ does not easily facilitate remote triggering as an explanation for why it is difficult to observe remote triggering in this region.

Clock advance is an experimentally derived brittle failure model that explains how dynamic stresses temporally bring faults closer to failure (*Gomberg et al*., 1998) and may be a factor in triggering along the SJFZ. With clock advance, faults that are continually experiencing tectonic loading receive an extra push from transient stresses associated with teleseismic waves. The added stress can locally increase stress above the Coulomb failure criterion on optimally oriented faults and fractures, causing them to fail earlier in their earthquake cycle than if the dynamic stresses had not been present (*Gomberg et al*., 1998). Brittle failure models have been used to potentially explain remote dynamic triggering in areas ranging from Greece, to the Salton Sea geothermal field, to central Himalaya (*Brodsky et al*., 2000, *Meng and Peng*, 2014; *Mendoza et al*., 2016). Clock advance can explain events triggered in the presence of transient stresses from teleseismic waves, but it does not explain the extended 2-day period of increased seismicity seen in the stacked histogram (Figure 3.2). Even in the individual histograms for the triggered events, we consistently see increased local seismicity for roughly 48 hours. Local processes may be the driving factors for this sustained triggering. It is possible for teleseismic waves to trigger slow slip or accelerated creep, which in turn affects local stress heterogeneity to facilitate the occurrence of small earthquakes (*Delahaye et al.*, 2009; *Shelly et al*., 2011; *Vidale et al*., 2011). Based on previous studies, the SJFZ is capable of tremor, which is a signature of slow slip. *Wang et al*.

(2013) found that Love waves from the 2002 Mw 7.8 Denali earthquake dynamically triggered a tremor episode in the Anza region of the SJFZ. A more extensive study of non-volcanic tremor along the SJFZ found several deep tremor episodes north and south of the Anza Gap (*Hutchinson and Ghosh*, 2016). If tremor is common in this region, then slow slip may be a significant factor in the ability of transient stresses to trigger local earthquakes for an extended period of time. Any of the proposed models or additional physical models could individually or collectively explain the occurrence of earthquake triggering.

3.6. Conclusions

We present evidence for remote triggering of small local earthquakes in the SJFZ. In general, it appears as though remote events do not often trigger the SJFZ and multiple levels of tests are necessary to determine whether triggering occurred. We conservatively estimate that 14 remote events triggered, and 10 events likely triggered an increase in both the magnitude and number of earthquakes in the San Jacinto region for roughly 2 days. It is possible that the SJFZ infrequently reaches a critically stressed state that coincides with a remote event, resulting in infrequently triggered earthquakes. The infrequent nature of the triggering may be due to a complex interplay of dynamic stresses with local processes such as small-scale stress heterogeneities, pore fluid pressure, and slow slip activity.

3.7. References

Brodsky, E. E., E. Roeloffs, D. Woodcock, I. Gall, and M. Manga (2003), A mechanism for sustained groundwater pressure changes induced by distant earthquakes, *J. Geophys. Res*., *108*, doi:10.1029/2002JB002321.

Brodsky, E. E., V. Karakostas, and H. Kanamori (2000), A new observation of dynamically triggered regional seismicity: Earthquakes in Greece following the August, 1999 Izmit, Turkey earthquake, *Geophys. Res. Lett*., *27*, 2741-2744.

Brodsky, E. E., and N. J. van der Elst (2014), The uses of dynamic earthquake triggering, *Annu. Rev. Earth Planet. Sci.*, *42*, 317-339.

Brodsky, E. E. (2006), Long-range triggered earthquakes that continue after the wave train passes, *Geophys. Res. Lett*., *33*, L15313, doi:10.1029/ 2006GL026605.

Delahaye, E. J., J. Townend, M. E. Reyners, and G. Rogers (2009), Microseismicity but no tremor accompanying slow slip in the Hikurangi subduction zone, New Zealand, *Earth Planet. Sci. Lett*., *277*(1), 21-28.

Freed, A. M., and J. Lin (2001), Delayed triggering of the 1999 Hector Mine earthquake by viscoelastic stress transfer, *Nature*, *411*(6834), 180-183.

Gomberg, J., N. M. Beeler, and M. L. Blanpied (1998), Earthquake triggering by transient and static deformations. *J. Geophys*. *Res*., *103*, 24411-24425.

Gomberg, J., P. A., Reasenberg, P. Bodin, and R. A. Harris (2001), Earthquake triggering by seismic waves following the Landers and Hector Mine earthquakes, *Nature*, *411*(6836), 462-466.

Hill, D. P., and S. G. Prejean (2007), Dynamic triggering, in *Treatise on Geophysics*, *vol. 4*, edited by H. Kanamori, pp. 257–292, Elsevier, New York.

Hill, D. P., et al. (1993), Seismicity remotely triggered by the magnitude 7.3 Landers, California, earthquake, *Science*, *260*, 1617–1623.

Hill, D. P. (2008), Dynamic stresses, Coulomb failure, and remote triggering, *Bull. Of Seismol. Soc. of Am*., *98*(1), 66-92.

Hutchison, A. A., and A. Ghosh (2016), Tectonic tremor in the San Jacinto Fault, near the Anza Gap, detected by multiple mini seismic arrays (in prep).

Kane, D. L., D. Kilb, A. S. Berg, and V. G. Martynov (2007), Quantifying the remote triggering capabilities of large earthquakes using data from the ANZA Seismic Network catalog (southern California), *J. Geophys. Res.*, *112*, B11302, doi:10.1029/2006JB004714.

Kilb, D., J. Gomberg, and P. Bodin (2000), Triggering of earthquake after-shocks by dynamic stresses, *Nature*, *408*(6812), 570–574, doi:10.1038/35046046.

Kilb D., J. Gomberg, P. Bodin (2002), Aftershock triggering by complete Coulomb stress changes. *J. Geophys. Res.-Solid Earth*, *107*(B4), ESE 2-1–ESE 2-14, doi:10.1029/2001JB000202.

Lay, T., and T. C. Wallace (1995), *Modern Global Seismology*, Academic, San Diego, Calif.

Love, A. E. H. (1927), *Mathematical Theory of Elasticity*, Cambridge Univ., Cambridge, U. K.

Matthews M.V., and P. A. Reasenberg (1988), Statistical-methods for investigating quiescence and other temporal seismicity patterns. *Pure Appl. Geophys*. *126*(2–4), 357-372.

Mendoza, M. M., A. Ghosh, S. S. Rai (2016), Dynamic triggering of small local earthquakes in the central Himalaya, *Geophys. Res. Lett*., 43, 9581-9587, doi:10.1002/2016GL069969.

Meng, X., and Z. Peng (2014), Seismicity rate changes in the Salton Sea Geothermal Field and the San Jacinto Fault Zone after the 2010 M_w 7.2 El Mayor-Cucapah earthquake, *Geophys*. *J. Int.*, *197*, 1750-1762, doi:10.1093/gji/ggu085.

Prejean S. G., D. P. Hill, E. E., Brodsky, S. E. Hough, M. J. S. Johnson, et al. (2004), Remotely triggered seismicity on the United States west coast following the M 7.9 Denali fault earthquake, *Bull. Seismol. Soc. Am*., *94*(6B), S348-S359.

Sharp, R.V, 1967, San Jacinto fault zone in the Peninsular Ranges of Southern California. *Geol. Soc. Am. Bull*, *78*, p. 705-729.

Shelly, D. R., Z. G. Peng, D. P. Hill, and C. Aiken (2011), Triggered creep as a possible mechanicsm for delayed dynamic triggering of tremor and earthquakes.

Thatcher, W., J. A. Hileman, and T. C. Hanks (1975), Seismic slip distribution along the San Jacinto fault zone, southern California, and its implications, *Geol. Soc. Am. Bull*., *86*, 1140-1146.

van der Elst, N. J., and E. E. Brodsky (2010), Connecting near-field and far-field earthquake triggering to dynamic strain, *J. Geophys. Res*., *115*, B07311, doi:10.1029/2009JB006681.

Velasco, A. A., S. Hernandez, T. Parsons, K. Pankow (2008), Global ubiquity of dynamic earthquake triggering. *Nature Geoscience*, *1*, 375-379, doi:10.1038/ngeo204.

Vidale, J. E., A. J. Hotovec, A. Ghosh, K. C. Creager, and J. Gomberg, (2011), Tiny intraplate earthquakes triggered by nearby episodic tremor and slip in Cascadia, *Geochem. Geophys. Geosyst*., 12, Q06005, doi:10.1029/2011GC003559.

Wang C. Y., and M. Manga (2009), Hydrologic response to earthquakes and a general metric, *Geofluids*, *10*, 206-216.

Wang T. H., E. S. Cochran, D. Agnew, D. D. Oglesby (2013), Infrequent triggering of tremor along the San Jacinto Fault near Anza, California. *Bull Seimol. Soc. Am*., *103*, 2482-2497.

3.8. Tables

Table 3.1. Triggering Candidates. These are the 25 events with a beta value ≥ 2 when the background rate is averaged over 30 days.

Earthquake Location	Date	Time	Lat	Lon	Depth (km)	M_w
South Pacific Ocean	2005-05-12	11:15:35.34	-57.382	-139.231	10.0	6.5
Papua New Guinea	2005-09-29	15:50:24.03	-5.437	151.840	25.0	6.6
Russia	2006-05-22	11:12:00.80	60.772	165.743	19.0	6.6
Kermadec-Trench	2007-01-31	03:15:52.29	-29.776	-178.002	34.0	6.5
Solomon Islands	2007-06-28	02:52:10.99	-7.979	154.635	18.0	6.7
Vanuatu	2007-08-01	17:08:51.40	-15.595	167.680	120.0	7.2
Aleutian Trench	2007-08-02	03:21:42.82	51.307	-179.971	21.0	6.7
New Zealand	2007-10-15	12:29:34.86	-44.796	167.553	18.0	6.8
New Hebrides Trench	2008-04-09	12:46:12.72	-20.071	168.892	33.0	7.3
British Columbia	2008-05-02	01:33:37.24	51.864	-177.528	14.0	6.6
Ryukyu-Trench	2009-10-30	07:03:39.12	29.218	129.782	34.0	6.8
Solomon Islands	2010-01-05	12:15:32.21	-9.019	157.551	15.4	6.8
Baja California	2010-04-04	22:40:42.36	32.286	-115.295	10.0	7.2
Bay of Bengal	2010-06-12	19:26:50.46	7.881	91.936	35.0	7.5
Chile	2011-01-02	20:20:17.78	-38.355	-73.326	24.0	7.2
Kermadec Trench	2011-04-18	13:03:02.73	-34.336	179.874	86.0	6.6
Tonga-Trench	2011-10-21	17:57:16.10	-28.993	-176.238	33.0	7.4
West of North Sumatra	2012-01-10	18:36:59.08	2.433	93.210	19.0	7.2
Baja California	2012-04-12	07:15:48.50	28.696	-113.104	13.0	7.0
Chile	2012-04-17	03:50:15.61	-32.625	-71.365	29.0	6.7
Argentina	2012-05-28	05:07:23.45	-28.043	-63.094	586.9	6.8
Queen Charlotte	2012-10-28	03:04:08.82	52.788	-132.101	14.0	7.8
Queen Charlotte	2012-10-28	03:07:30.00	52.769	-131.927	5.0	7.7
Papua New Guinea	2013-03-10	22:51:51.60	-6.653	148.155	28.9	6.5
Offshore Nicaragua	2013-06-15	17:34:29.07	11.725	-86.975	35.8	6.5
South of Japan	2015-05-30	11:23:02.10	27.841	140.488	664.0	7.8

Table 3.2. Triggering Events. These events are selected based on the minimum criteria of having beta values ≥ 2 and a higher peak magnitude local earthquake occurring after the remote events. Additionally, 11 of these events also have an increase in local earthquakes (S-P times ≤ 6.7s) from a visual scan, and evidence of local earthquakes occurring during the passage of waves from the remote event.

Earthquake Location	Date	Time	Lat	Lon	Depth (km)	M_w
South Pacific Ocean	2005-05-12	11:15:35.34	-57.382	-139.231	10.0	6.5
Papua New Guinea	2005-09-29	15:50:24.03	-5.437	151.840	25.0	6.6
Russia	2006-05-22	11:12:00.80	60.772	165.743	19.0	6.6
Kermadec-Trench	2007-01-31	03:15:52.29	-29.776	-178.002	34.0	6.5
Vanuatu	2007-08-01	17:08:51.40	-15.595	167.680	120.0	7.2
Aleutian Trench	2007-08-02	03:21:42.82	51.307	-179.971	21.0	6.7
New Zealand	2007-10-15	12:29:34.86	-44.796	167.553	18.0	6.8
Solomon Islands	2010-01-05	12:15:32.21	-9.019	157.551	15.4	6.8
Baja California	2010-04-04	22:40:42.36	32.286	-115.295	10.0	7.2
Bay of Bengal	2010-06-12	19:26:50.46	7.881	91.936	35.0	7.5
Chile	2011-01-02	20:20:17.78	-38.355	-73.326	24.0	7.2
Kermadec Trench	2011-04-18	13:03:02.73	-34.336	179.874	86.0	6.6
Baja California	2012-04-12	07:15:48.50	28.696	-113.104	13.0	7.0
Chile	2012-04-17	03:50:15.61	-32.625	-71.365	29.0	6.7

General Conclusions

Dynamic stress plays a critical role in the generation, temporal evolution, and cessation of earthquakes. From localized shear stress changes that determine which path an earthquake will take along a complex fault system, to the remote triggering of local events by passing seismic waves, dynamic stress affects seismicity and subsequent seismic hazard in heavily-populated southern California. The present work investigates how dynamic stresses affect earthquake behavior on two of the largest fault systems in southern California: the San Andreas fault system (SAF) in the San Gorgonio Pass region (SGP) and the San Jacinto fault zone (SJFZ). Dynamic stress can either facilitate or hinder earthquake rupture propagation along the SAF, depending on fault geometry and initial stress assumptions, and it can trigger a temporary increase in local events along the SJFZ.

Dynamic rupture models of the SAF through the SGP demonstrate a complex interplay between fault geometry and initial stress assumptions. Our first set of models use a relatively simple fault geometry, which incorporates the San Bernardino strand of the SAF and two thrust faults from the San Gorgonio Pass Fault Zone. However, these simplified models are still more complex than some of the previous numerical models in the area (e.g. *Olsen et al*. 2006; 2008). The results from this set of models support previous work in both rupture dynamics and some studies on the SGP. Rupture propagation paths in our models are affected by the size of gaps between faults (*Harris and Day*, 1993), branching angles (*Kame et al.*, 2003), and relative orientation of thrust and strike-slip faults (*Oglesby*, 2005). The results are fairly robust across both the initial

stress conditions of constant tractions and regional stress fields, implying that fault geometry and dynamic shear stresses are the controlling factors in these models. In the simplified models, earthquakes that nucleate on the right-lateral strike-slip San Bernardino strand of the SAF do not propagate to the San Gorgonio Pass Fault Zone under any assumptions. Nucleation on a thrust fault in the San Gorgonio Pass Fault Zone east of the San Bernardino strand often leads to multi-fault rupture, including several through-going scenarios, due to dynamic increases in shear stress. Nucleation on a thrust in the San Gorgonio Pass Fault Zone west of the San Bernardino strand occasionally leads to multi-fault rupture, including some through-going scenarios. These results imply that earthquakes initiating northwest of the SGP do not lead to through-going rupture, while earthquakes initiating southeast of the San Bernardino strand can cause through-going scenarios that are similar to those of the TeraShake models (*Olsen et al.*, 2006; 2008). Earthquakes nucleating within the SGP on the San Gorgonio Pass Fault Zone may be capable of becoming a damaging event that affects large parts of metropolitan and suburban southern California.

Our second set of models in the SGP employ an even more realistic (and complex) fault geometry based on *Plesch et al.* (2007), with refinements made by *Herbert and Cooke* (2012), *Herbert et al*. (2014) and *Fattaruso et al*. (2014), and three different pre-stress assumptions: constant tractions, regional stress loading, and evolved stresses from long-term quasi-static crustal deformation modeling. We will henceforth refer to models from Chapter 1 of this dissertation as the "simplified models" and those from Chapter 2 as the "complex models." The results of the complex models vary

substantially from the results of the simplified models. The most consistent result of the complex models is that rupture does not propagate from the San Gorgonio Pass Fault Zone to any other faults, which appears to contradict the results of the simplified models. While none of the simplified models resulted in propagation jumping from the San Bernardino strand to either of the thrusts in the San Gorgonio Pass Fault Zone, this type of behavior was possible in the complex models that assumed regional stress loading and evolved stresses. These contradictory results are likely due to significant differences in the fault geometry. In the simplified models, only small portions of the San Gorgonio Pass Fault Zone are included, with the thrusts making perfect 90-degree angles along-strike with respect to the San Bernardino strand. However, in the complex models, the entirety of the mapped San Gorgonio Pass Fault Zone is included. With the larger fault, smaller-scale sharp angles are smoothed and overall the western portion of the San Gorgonio Pass Fault Zone has a much narrower along-strike angle (roughly 30 degrees) with the San Bernardino strand. The western portion also connects to the San Bernardino strand at depth, instead of remaining perfectly perpendicular. These changes in orientation are significant enough to cause different results between the two sets of models. *Kame et al*. (2003) show that narrower angles between fault branches can inhibit rupture on one of the branches due to the stress shadowing effect. We see this effect in particular on parts of the San Bernardino strand in complex models where earthquakes nucleate on the Garnet Hill strand. In comparison, wide angles between branches weaken the shear and normal stress interactions between branches, causing rupture to be more independent of slip on adjacent faults (*Kame et al*., 2003), which is similar to the

simplified models. With the complex models that assume regional stress loading, the difference in fault geometry controls the difference in the results. We use the end members of the regional stress fields tested in the simplified models in the complex models as well, and the results are vastly different, including through-going rupture with models that nucleate on the San Bernardino strand.

While the differences in fault geometry can account for some of the contradictory results between the simplified and complex models, the initial stress conditions also have an impact on the results. Compared to the simplified models, we use oblique stress on the San Bernardino and Garnet Hill strands in constant traction assumptions of the complex models, instead of pure strike-slip. This variation in the stress field in addition to the different fault geometry may account for abrupt rupture terminations in the complex models. The evolved stresses are only used with the complex models, so there is no comparison available with the simplified models. The evolved stresses are highly heterogeneous compared to typical initial stress conditions and our results validate previous studies that show heterogeneous stresses can complicate rupture propagation in models with complex fault branching (*Duan and Oglesby*, 2007). Compared with the simplified models, it appears as though the initial stress conditions have a stronger influence on the models than dynamic stress changes, which corroborates the conclusions of *Kame et al*. (2003) that pre-stress states have significant effects on the favored direction of rupture propagation.

Given the large variability in our results, we conclude that the SGP is a region that may act as barrier for rupture propagation in many circumstances, but it is also capable of

producing through-going ruptures. The results of the simplified models match those of *Olsen et al*. (2006), which indicate through-going rupture is possible for earthquakes initiating southeast of the SGP and inhibited for earthquakes initiating northwest of the SGP. Complex models assuming regional stress loading also match *Olsen et al*. (2006), but only for nucleation on the Garnet Hill strand. Complex models assuming regional stress loading and nucleation on the San Bernardino strand supports the conclusions of *Carena et al*. (2004), which indicate that earthquakes occurring on the SAF northwest of the SGP could possibly rupture through the SGP on rare occasions. Complex models, assuming constant tractions, resemble the results of *Shi et al*. (2012), which assumed homogenous volumetric stress; both sets of results concluded that rupture initiating from either side of the SGP could not propagate across the SGP. The large variability in the results also suggests that multiple fault geometries should be tested and initial stress conditions should be further studied before more robust results can be established.

Our final conclusions are with regards to the capability of dynamically triggered events along the SJFZ. It appears as though remote events do not often trigger the SJFZ and multiple tests, including statistical analysis of the number of events before and after a remote event, peak magnitude analysis, and visual scans of seismograms, are necessary to determine whether triggering occurred. Out of 25 triggering candidates identified with the statistical test, we conservatively estimate that 14 remote events triggered, and 10 events likely triggered an increase in both the magnitude and number of earthquakes in the San Jacinto region for roughly 2 days. It is possible that the SJFZ infrequently reaches a critically stressed state that coincides with a remote event, resulting in

infrequently triggered earthquakes. The infrequent nature of the triggering may be due to a complex interplay of dynamic stresses with local processes such as small-scale stress heterogeneities, pore fluid pressure, and slow slip activity.

References

Carena, S., J. Suppe, and H. Kao (2004), Lack of continuity of the San Andreas fault in Southern California: Three-dimensional fault models and earthquake scenarios, *Journal of Geophysical Research*, *109*, B04313, doi:04310.01029/02003JB002643.

Duan, B., and D.D. Oglesby, 2007, Nonuniform prestress from prior earthquakes and the effect on dynamics of branched fault systems, *J. of Geophys. Res.*, *112*, B05308, doi:10.1029/2006JB004443.

Fattaruso, L., M.L. Cooke, R.J. Dorsey (2014), Sensitivity of uplift patterns to dip of the San Andreas fault in the Coachella Valley, California, *Geosphere*, *10*(6), 235–1246; doi:10.1130/GES01050.1.

Harris, R. A., and S. M. Day (1993), Dynamics of Fault Interaction - Parallel Strike-Slip Faults, *Journal of Geophysical Research*, *98*(B3), 4461-4472.

Herbert, J.W., and M.L. Cooke (2012), Sensitivity of the southern San Andreas fault

system to tectonic bound- ary conditions and fault configurations, *Bull. of the Seis. Soc. of Am.*, *102*, 2046– 2062, doi: 10 .1785 /0120110316.

Herbert, J.W. et al. (2014), How much can off-fault deformation contribute to the slip rate discrepancy within the eastern California shear zone?, *Geology*, *42*, 71 – 74.

Kame, N., J. R. Rice, and R. Dmowska (2003), Effects of pre-stress state and rupture velocity on dynamic fault branching, *Journal of Geophysical Research*, *108*(B5), 2265, doi: 2210.1029/2002JB002189.

Oglesby, D. D. (2005), The dynamics of strike-slip step-overs with linking dip-slip faults, *Bulletin of the Seismological Society of America*, *95*(5), 1604-1622.

Olsen, K. B., S. M. Day, J. B. Minster, Y. Cui, A. Chourasia, D. Okaya, P. Maechling, and T. Jordan (2008), TeraShake2: Spontaneous rupture simulations of M-w 7.7 earthquakes on the southern San Andreas fault, *Bulletin of the Seismological Society of America*, *98*(3), 1162-1185.

Olsen, K. B., S. M. Day, J. B. Minster, Y. Cui, A. Chourasia, M. Faerman, R. Moore, P. Maechling, and T. Jordan (2006), Strong shaking in Los Angeles expected from southern San Andreas, *Geophysical Research Letters*, *33*, L07305, doi:07310.01029/02005GL025472.

Plesch, A., et al. (2007), Community Fault Model (CFM) for Southern California, *Bulletin of the Seismological Society of America*, *97*(6), 1793-1802.

Shi, Z., S. Ma, S. M. Day, and G. P. Ely (2012), Dynamic rupture along the San Gorgonio Pass section of the San Andreas Fault, *Seism. Res. Lett*., 83, 423.